



#### This is to certify that the

Nanoscale Metal and Alloy Particles by Homogeneous
Reduction with Alkalides or Electricles
and Reduction in Zeolite Pores
presented by

Kuo-Lih Tsai

has been accepted towards fulfillment of the requirements for

Ph. D. degree in Chemistry

Date / / / /

Major professor

MSU is an Affirmative Action/Equal Opportunity Institution

0-12771

# NANOSCALE METAL AND ALLOY PARTICLES BY HOMOGENEOUS REDUCTION WITH ALKALIDES OR ELECTRIDES AND REDUCTION IN ZEOLITE PORES

Ву

Kuo-Lih Tsai

## A DISSERTATION

Submitted to
Michigan State University
in partial fulfillment of the requirements
for the degree of

DOCTOR OF PHILOSOPHY

Department of Chemistry

1991

#### ABSTRACT

## NANOSCALE METAL AND ALLOY PARTICLES BY HOMOGENEOUS REDUCTION WITH ALKALIDES OR ELECTRIDES AND REDUCTION IN ZEOLITE PORES

Вy

#### Kuo-Lih Tsai

A new method for the preparation of small metal/oxidized metal or alloy particles and reduction in zeolite pores is described, that utilizes homogeneous reduction of metal salts by dissolved alkalides or electrides in an aprotic solvent such as dimethyl ether or tetrahydrofuran. Soluble compounds of transition metals and post-transition metals in dimethyl ether or tetrahydrofuran are rapidly reduced at -30 °C by dissolved alkalides or electrides to produce metal particles with crystallite sizes from < 3 to 15 nm. The average particle size was estimated from the line broadening of powder X-ray diffraction. Particle size distributions were determined by counting the particles on electron micrographs obtained by transmission electron microscopy. Salts of Au, Pt, Cu, Te, Fe, and Ta formed metallic particles with little or no oxidation even when washed with methanol or liquid ammonia. of salts of Ni, Fe, Zn, Ga, Si, Mo, W, In, Sn, and Sb yields surface oxidation over a metallic core. This method is also applicable to the formation of finely divided metals on oxide supports.

Alloys or intermetallic compounds formed when two different metal salts were used, as indicated by X-ray photoelectron spectroscopy. Confirmation by electron diffraction was made in the case of air-stable samples. Reduction of salts of Au-Cu, Au-Zn, Cu-Te, Zn-Te, Au-Ti, Fe-Ta formed particles that contained intermetallic compounds.

Stoichiometric amounts of the alkalide or electride were used; these were prepared separately or in situ. FT-IR spectroscopy was used to demonstrate that the presence of organic complexants and solvents often resulted in the inclusion of organic decomposition products due to the high reactivity of nanoscale metal particles. Elemental analysis showed that both carbon and hydrogen were less than one percent in atomic concentration on the surface of gold.

Electrides, the most powerful reducing agents, were used to reduce Cu<sup>2+</sup>, Pd<sup>2+</sup>, Ag<sup>+</sup> in zeolite-Y. X-ray photoelectron spectroscopy data show that these cations were completely reduced to the zero oxidation state at -30 °C. Cu and Pd remain trapped in the interior and an alkali metal cation balances the counter charge upon reduction. In contrast, Ag formed 40 Å diameter particles uniformly on the external surface. This method should also be applicable to the synthesis of organometallic compounds.

## To my parents and Ruwen

#### **ACKNOWLEDGEMENTS**

I would like to express my appreciation to Dr. James L. Dye for his continual guidance and support throughout this work. I would also like to thank Dr. Kim Dunbar, Dr. Mercoury Kanatzidis and Dr. James Harrison for their helpful discussions and advice.

Appreciation is also extended to all of the members of the Dye research group with whom I have worked, in particular Drs. Rui Huang, Evy Jackson, Jineun Kim, Kevin Moeggenborg, and Judith Eglin. I would like to thank the Master Glassblowers at Michigan State University, Keki Mistry, Manfred Langer, and Scott Bancroft, for the numerous pieces of glassware that they have designed, built, and repaired for me. I am grateful for the help from Dr. Karren L. Klomparens with the transmission electron microscopy, Dr. Kevin J. Hook with the X-ray photoelectron spectroscopy and Dr. Debbie Duxbury with the powder X-ray diffractometry.

I am grateful for finacial support from the National Science Foundation (Solid State Chemistry Grants Nos. 87-14751 and 90-17292) and the Center for Fundamental Materials Research at Michigan State University and the 1989 Graham summer fellowship, the 1990 Yates summer fellowship from the Chemistry Department, Michigan State University.

## TABLE OF CONTENTS

	LIST OF TABLES LIST OF FIGURES		
Chapter	1	Introduction	1
		A. Alkalides and Electrides	1
		B. Small Metal Particles	4
		C. Theory	4
		(I) X-ray Photoelectron Spectroscopy	4
		1. General background	4
		2. Nomenclature	7
		3. Chemical shifts	10
		(II) Powder X-ray Diffraction Line Broadening	
		(III) Electron Diffraction	15
		D. Objective	17
Chapter	2	EXPERIMENTAL METHODS	19
		A. Synthesis	19
		B. X-ray Photoelectron Spectroscopy	22
		C. Powder X-ray Diffraction	24
		D. Transmission Electron Microscopy	25
Chapter	3	SINGLE ELEMENT REDUCTION	26
•		A. Reduction with Alkalides or Electrides	26
		B. Reducing Agents	28
		C. Results	28
		(I) Gold	29
		(II) Copper	41
		(III) Tellurium	47
		(IV) Nickel	52
		(V) Antimony	52
		(VÍ) Gallium	52
		(VII) Zinc	56
		(VIII) Molybdenum	56
		(IX) Tin	56
		D. Summary	60

Chapter	4	BINARY ELEMENT REDUCTION	63
		A. Introduction	63
		B. Experimental	63
		C. Results	64
		(I) Au-Zn	65
		(II) Au-Cu	68
		(III) Tellurides	70
		(IV) Ti-Au	71
		(V) Ta-Fe	73
		D. Summary	76
Chapter :	5	REDUCTION in ZEOLITE PORES	77
•		A. Introduction	77
		B. Experimental	82
		C. Results	83
		D. Summary	92
Chapter	6	CONCLUSIONS and SUGGESTIONS for FUTURE WORK	93
APPEND	IX		99
REFEREN		S S	104

## LIST OF TABLES

Table 1-1.	X-ray and spectroscopic notation	9
Table 1-2.	Spin-orbit splitting parameters	9
Table 3-1.	Electron diffraction of Au from reduction of AuCl3	3 5
Table 3-2.	Electron diffraction of Cu from reduction of CuCl2	42
Table 3-3.	Electron diffraction of Te from reduction of TeBr4	5 1
Table 3-4.	Part of the periodic table showing the elements studied to date. Identification: 1, washable metals; 2, surface-oxidized; 3, nonwashable; 4, reoxidized. See the text for more detailed definition	62
Table 4-1.	Electron diffraction of AuZn from co-reduction of AuCl3+ZnI2	67
Table 4-2	Electron diffraction of AuCu from co-reduction of AuCl3+CuCl2	69

## LIST OF FIGURES

Figure	1-1.	Figure 1-1. Representative complexants: 15-Crown-5 (IUPAC name: 1,4,7,10,13- pentaoxacyclopentadecane) and Cryptand [222] (IUPAC name: 4,7,13,16,21,24-Hexaoxa-1,10-	
		diazabicyclo [8.8.8]hexacosane)	1
Figure	1-2.	Diagram of the X-ray photoelectron process	5
Figure	1-3.	Diagram of the fluorescent X-ray photoprocess and the Auger process	6
Figure	1-4	Two-dimensional zinc chemical state plot for XPS (from tabulation by C. D. Wagner, <i>Handbook of X-ray Photoelectron Spectroscopy</i> ; Perkin-Elmer; 1979; p84)	1 2
Figure	1-5.	Diagram of X-ray diffraction	1 4
Figure	1-6.	Diagram of electron diffraction	16
Figure	2-1.	Kontes double tube("H-cell") use to prepare metal and alloy particles	20
Figure	3-1.	XPS spectrum of Au from the product of reduction of AuCl <sub>3</sub>	3 1
Figure	3-2.	XRD lines(111) used to determine average particle sizes for Au.	3 2
Figure	3-3.	Particle size distributions for Au	3 3
Figure	3-4.	Electron micrograph of Au (mag=100,000X, 1,000 Å/cm)	3 4
Figure	3-5.	Selected area electron diffraction of Au.	3 4

Figure	3-6.	Electron micrograph of Au particles on Al2O3(mag=190,000X, 550 Å/cm)	3 6
Figure	3-7.	Optical absorption spectra of an Au colloidal solution	3 7
Figure	3-8.	XRD spectrum of the products from the reduction of AuCl <sub>3</sub> . (A=6.5x10 <sup>-4</sup> M, B=1.6x10 <sup>-4</sup> M)	3 8
Figure	3-9.	FT-IR spectra of washed Au particles	40
Figure	3-10.	XRD lines(111) used to determine average particle sizes for Cu	4 1
Figure	3-11.	Selected area electron diffraction of Cu (camera length=140 cm)	4 2
Figure	3-12.	Electron micrograph of Cu (mag=320,000X, 310 Å/cm)	44
Figure	3-13.	Particle size distribution of Cu	44
Figure	3-14.	Energy dispersive spectra of Cu particles on Ni grid	4 5
Figure	3-15.	XPS spectrum of Cu (A before washing, B exposed to air for 24 hours, and C after washing)	46
Figure:	3-16.	XPS spectrum of Te (A before washing, B exposed to air for 3 min, and C after washing)	4 8
Figure	3-17.	XRD lines(100) used to determine average particle sizes for Te	49
Figure	3-18.	Electron micrograph of Te (mag=140,000X, 700 Å/cm)	5 0
Figure	3-19.	Selected area electron diffraction of Te (camera length=140 cm)	50
Figure	3-20.	XPS spectrum of Ni.(A) before washing (B) oxidised in the air for 24 h (C) washed by MeOH	i 53

Figure 3-21.	XPS spectrum of Sb. (A) before washing (B) washe by MeOH (C) sputtered by Ar ions	d 54
Figure 3-22.	XPS spectrum of L3M45M45 Auger peaks of Ga.  (A) reaction products (B) sputtered by Ar ions for 2 min (C) sputtered by Ar ions for 5 min	5 5
Figure 3-23.	XPS specrum of $L3M45M45$ Auger peaks of Zn. (A) reaction products (B) sputtered by Ar ions for 2 min (C) sputtered by Ar ions for 4 min	57
Figure 3-24.	XPS specrum of 3d peaks of Mo. (A) reaction products (B) sputtered by Ar ions for 10 min (C) sputtered by Ar ions for 30 min	5 8
Figure 3-25.	XPS specrum of 3d peaks of Sn. (A) reaction produ (B)exposed to the air for 30 seconds	ucts 59
Figure 4-1.	XPS spectrum for the 4f5/2 and 4f7/2 levels of Au:(A) Au particles from AuCl3 reduction; (B)AuZn particles formed from reduction of a mixture of AuCl3 and excess ZnI2; (C) AuZn + Au particles formed from reduction of a mixture of AuCl3 and ZnI2 with the former in excess	66
Figure 4-2.	XPS of the reduction product of a mixture of TiCl4 and AuCl3 in Me <sub>2</sub> O (top) and after washing with air-free methanol (bottom)	72
Figure 4-3.	XPS results for the Ta-Fe system; product washed with anhydrous NH3: (A) Fe XPS from 2:1 FeCl3 to TaCl5; (B) Fe XPS from FeCl3 alone; (C) Ta XPS from 2:1 FeCl3 to TaCl5; (D) Ta XPS from TaCl5 alone	75
Figure 5-1.	Structure of sodalite cage	79
•	Structure of zeolite Y	8.0

- Figure 5-3. XPS spectra of Pd in zeolite Y before reduction 3d5/2=337.5 eV, 3d3/2=343.0 eV (top) and after reduction 3d5/2=335.2 eV, 3d3/2=340.4 eV (bottom).
- Figure 5-4. The XPS survey scans of (A) plain zeolite Y (B) after Na<sub>2</sub>PdCl<sub>4</sub> ion exchange (new peaks of Pd 3d<sub>5/2</sub> at 337 eV and 3d<sub>3/2</sub> at 343 eV appear and Na 1s peak at 1071 eV decreases) (C) after reduction by, K+(15C<sub>5</sub>)<sub>2</sub>e<sup>-</sup>, (new peaks of K 2p appear showing potassium cations balance the counter charge) 86
- Figure 5-5. XPS spectra of Cu in zeolite Y before reduction  $(2p_3/2=934.35 \text{ eV}, 2p_1/2=954.15 \text{ eV top})$ , after reduction  $(2p_3/2=933.7 \text{ eV}, 2p_1/2=953.8 \text{ eV middle})$ , and oxidized in air  $(2p_3/2=935.8 \text{ eV}, 2p_1/2=955.9 \text{ eV})$  bottom) 88
- Figure 5-6. XPS spectra of Ag in zeolite Y before reduction 3d5/2=369.5 eV, 3d3/2=375.6 eV (top) and after reduction 3d5/2=368.7 eV, 3d3/2=374.7 eV (bottom) 90
- Figure 5-7 The XPS survey scans of (A) plain zeolite Y (B) after AgNO<sub>3</sub> ion exchange ( new peaks of Ag 3d5/2 at 369 eV and 3d3/2 at 375 eV appear and Na 1s peak at 1071 eV disappear) (C) after reduction by, K+(15C5)<sub>2</sub>e<sup>-</sup>,(the peak intensities of Ag show surface enrichment and new peaks of K 2p appear showing potassium cations balance the counter charge) 91

## Chapter 1 INTRODUCTION

#### A. Alkalides and Electrides

Alkali metals were found to dissolve in liquid ammonia by Weyl in 1864.(1) Since then, the study of metal ammonia solutions has become an active research area. Two major species present in the blue ammonia solutions are the metal cations  $(M^+)$  and the solvated electron  $(e^-_{SOlV})$ . Crown ethers and cryptands were synthesized by Pedersen and Lehn respectively in the 1960's.(2, 3, 4) Crown ethers are cyclic polyethers and cryptands are bicyclic polyethers that readily complex metal cations: examples are shown in Figure 1-1.

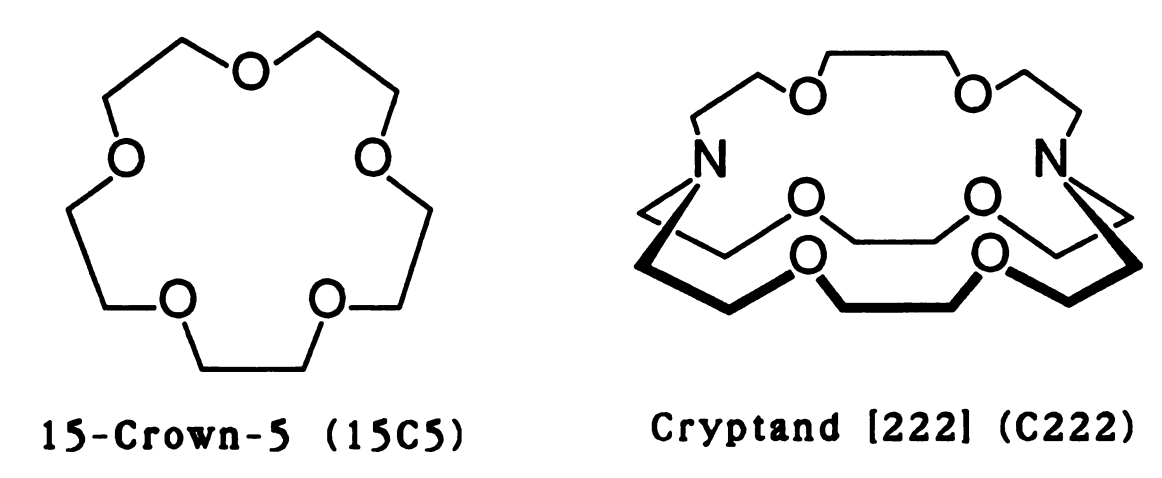


Figure 1-1. Representative complexants: 15-Crown-5 (IUPAC name: 1.4.7.10.13-pentaoxacyclopentadecane) and Cryptand [222] (IUPAC name: 4.7.13.16.21.24-Hexaoxa-1.10-diazabicyclo [8.8.8]hexacosane).

In the early 1970's. Dye and co-workers combined alkali metals with crown ethers and cryptands in amine or ether solvents to produce a new class of compounds, which they called alkalides. Alkalides are salts in which the cation is a complexed alkali metal cation, and the anion is that of either the same or a different alkali metal. The first alkalide, Na<sup>+</sup>(C222)Na<sup>-</sup>, was reported in 1974.(5)

By changing the ratio of metal and complexant. Dye and coworkers synthesized another new class of compounds called electrides. Electrides have the same complexed cation as alkalides but the anion is replaced by a trapped electron. The first crystalline electride, Cs<sup>+</sup>(18C6)2e<sup>-</sup>, was reported in 1983.(6) So far, more than 40 alkalides and 10 electrides have been synthesized by using various alkali metals and complexants.

These compounds crystallize from solution to yield shiny bronze-colored crystals (alkalides) or black crystals (electrides) which are all reactive towards air and moisture and thermally unstable at room temperature. Because of their unusual nature and properties, they have been studied by a variety of experimental methods. These include optical studies. (7) nuclear magnetic resonance spectroscopy. (8) electron paramagnetic resonance spectroscopy. (9) magnetic susceptibility. (10) single crystal X-ray crystallography. (11) powder X-ray diffraction. (12) photo emission spectroscopy. (13) and pressed powder electrical conductivity. (14, 15)

Because alkalides and electrides are air sensitive and thermally unstable, their synthesis must be done at low temperatures in the absence of air, moisture and other reducible substances. The synthesis of alkalides and electrides via vacuum line techniques has

been described in detail elsewhere so only a brief description will be given here. (16, 17)

The apparatus usually used to synthesize these compounds is called a "K celi".(16) To synthesize either an alkalide or an electride, the reactants are placed in a reaction vessel in a helium filled inert atmosphere dry box. The complexant is added to one chamber of the cell through one side-arm and the metal is added to another side-arm in an opened glass ampoule. The side-arms are then closed with an Ultra-Torr connector and a sealed glass tube. After removal from the dry box the metal in the ampoule is distilled into one chamber of the cell and the side-arms are sealed off. This is accomplished by heating the ampoule with a torch which produces a thin film of metal in the chamber (Note that this cannot be done with lithium).

A solvent such as methylamine or dimethyl ether is distilled into the complexant side of the cell. The solvent is used to dissolve both the complexant and the metal by repeatedly washing from one chamber of the cell to the other. Next, most of the first solvent is removed and a second less polar solvent is added to precipitate the product. The solution is then allowed to stand for several hours, after which the precipitate in the chamber is washed several times with the second solvent. After final removal of the second solvent, the polycrystalline precipitate is poured into the "fingers" at the top of the cell and vacuum-sealed to prevent decomposition. The compounds are stored in a liquid nitrogen dewar or a -80 °C freezer until needed.

#### B. Small Metal Particles

The preparation of nanoscale particles (1-20 nm diameter) as colloids or aggregates is a well-developed field that involves a variety of chemical and physical techniques. (18, 19) Small noblemetal particles are commonly made by mild reduction. (20, 21, 22) Rieke and co-workers and others have reduced salts of more active metals in ethereal or hydrocarbon solvents, either heterogeneously with alkali metals (slow) or homogeneously with aromatic radical anions such as naphthalene (fast).(23, 24, 25, 26, 27) The products of such reactions are highly active metal powders. Other methods such as pyrolysis of precursors, (28) evaporation of metals, (29) matrix isolation (solvated metal atom dispersion).(30) and sol-gel processes (31) have also been used to prepare small metal particles. A more recent development is reduction with alkali metal organoborohydride solutions, such as NaB(Et)<sub>3</sub>H, that has been shown to yield both single metals and alloys of the iron-group elements and the noble metals.(32)

### C. Theory

## (1). X-ray Photoelectron Spectroscopy

## 1. General background

X-ray Photoelectron Spectroscopy (XPS), which is also commonly termed electron spectroscopy for chemical analysis (ESCA) is one of a number of surface analysis techniques. In addition to its

surface sensitivity. XPS is capable of providing chemical information such as the oxidation state and the nature of the chemical bonding, as well as elemental composition. Therefore, it is a very good method for the characterization of nanoscale particles.

XPS involves the energy analysis of electrons ejected from a surface under bombardment by soft X-rays. Mg Kα X-rays (1253.6 eV) or Al Kα X-rays (1486.6 eV) are ordinarily used. These photons have limited penetrating power in a solid, of the order of 1-10 micrometers. The photoelectron ejection process occurs when a core level electron absorbs a photon of energy greater than its binding energy. When this occurs, the electron is ejected from the atom with an energy characteristic of the exciting photon and the initial core level binding energy as illustrated in Figure 1-2.

$$\frac{1}{\frac{1}{1}} \frac{1}{\frac{1}{1}} \frac{3p}{3s} M$$

$$\frac{1}{\frac{1}{1}} \frac{1}{\frac{1}{1}} \frac{1}{\frac{1}{1}} \frac{2p}{e^{-2s}} L$$

$$\frac{1}{1} \frac{1}{1} \frac{1}{$$

Figure 1-2. Diagram of the X-ray photoelectron process.

The emitted electrons have kinetic energies given by

$$KE = hv - BE - \phi_S$$

in which KE is the kinetic energy of the photoelectron.

hv is the X-ray photon energy.

BE is the photoelectron binding energy.

 $\phi_S$  is the spectrometer work function.

When a sample is illuminated by an intense source of photons of a single well defined energy the resultant photoelectrons can be resolved into energy peaks that are characteristic of the emitting atoms. In addition to the photoelectrons emitted in the photoelectric process. Auger electrons are emitted due to relaxation of the energetic ions that remain after photoemission. Auger electron emission occurs roughly  $10^{-14}$  seconds after the photoelectric event. More than 99% of the energy of relaxation shown in Figure 1-3 is released through Auger processes. Fluorescent X-ray photon emission is another process in this energy range, but occurs less than one percent of the time.

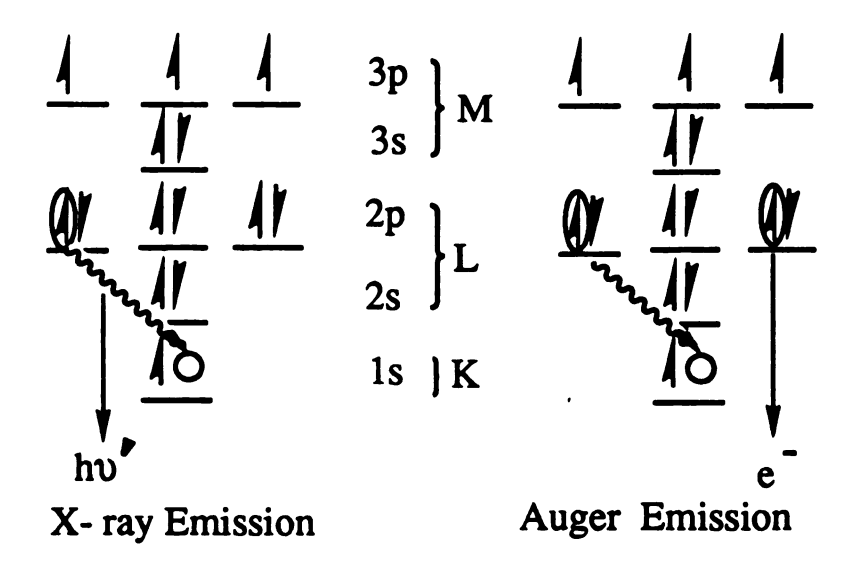


Figure 1-3. Diagram of the fluorescent X-ray photoprocess and the Auger process.

In the Auger process, an outer electron falls into the inner orbital vacancy, and a second electron is emitted, carrying off the excess energy. The Auger electron kinetic energy is equal to the difference between the energy of the initial ion and the doubly-charged final ion. This process is independent of the mode of the initial ionization. Thus photoionization often leads to two emitted electrons, a photoelectron and an Auger electron.

The path length of the photons in the material is of the order of micrometers, but that of the electrons is of the order of tens of Angstroms. Thus, while ionization occurs to a depth of a few micrometers, only those electrons that originate within tens of Angstroms of the solid surface can leave the surface without energy loss. It is these electrons that produce the peaks in the spectra and are most useful. Those that undergo loss processes before emerging contribute to the background.

#### 2. Nomenclature

Since an electron is a charged particle, its orbital motion around a nucleus induces a magnetic field whose intensity and direction depend on the electron velocity and on the radius of the orbit. Quantum mechanically, this is characterized by the orbital angular momentum operator. The appropriate quantum number  $\ell$  can take the values 0.1, 2, 3, ..... n-1 in which n is the principal quantum number. Another property of an orbiting electron is its intrinsic spin. Its spin quantum number s can take either of the values  $\pm 1/2$ .

The total electronic angular momentum is a combination of the orbital and spin angular momenta.

The total angular momentum of a single isolated atom is obtained by summing vectorially the individual electronic spin and angular momenta. For a particular electron, the total angular momentum is characterized by the quantum number j, where  $j=\ell+s$ . The value of j can be 1/2, 3/2, 5/2,....etc. The total angular momentum for the whole atom is the summation for all electrons.  $J = \Sigma j_{\ell}$ . This process is known as j-j coupling and occurs for inner core electrons in atoms.

Under j-j coupling the nomenclature is based on the principal quantum number n and the electronic quantum numbers  $\ell$  and j. In the X-ray notation, states with n=1, 2, 3, 4,... are designated K. L. M. N.... respectively, while states with various combinations of  $\ell=0, 1, 2, 3,...$  and j=1/2, 3/2, 5/2, 7/2,... are given conventional suffixes. 1, 2, 3, 4,....

A spectroscopic nomenclature has been developed that is equivalent to that used with X-rays. The principal quantum number appears first, then the states with  $\ell=0, 1, 2, 3, \ldots$  are designated  $s, p, d, f, \ldots$ , respectively and the j values are appended as suffixes. Thus the state written  $L_2$  in the X-ray notation, in which n=2,  $\ell=1$  and j=1/2, would be written  $2p_{1/2}$  in spectroscopic notation. The relation between X-ray and spectroscopic notation is summarized in Table 1-1.

Table 1-1. X-ray and spectroscopic notation

n	l	j	X-ray suffix	X-ray level	spectroscopic level
1	0	1/2	1	K	1 s <sub>1/2</sub>
2	0	1/2	1	Lı	$2s_{1/2}$
2	1	1/2	2	L2	$2p_{1/2}$
2	1	3/2	3	Lз	2p <sub>3/2</sub>
3	0	1/2	1	М1	3s <sub>1/2</sub>
3	1	1/2	2	M2	$3p_{1/2}$
3	1	3/2	3	М3	3p <sub>3/2</sub>
3	2	3/2	4	M4	3 d <sub>3/2</sub>
3	2	5/2	5	M5	3 d <sub>5/2</sub>
etc.	etc.	etc.	etc.	etc.	etc.

Spin-orbit coupling results in splitting of the atomic p, d, f energy levels into  $p_{1/2}$  and  $p_{3/2}$ ,  $d_{3/2}$  and  $d_{5/2}$ , and  $f_{5/2}$  and  $f_{7/2}$  components. The relative intensities of the doublet peaks are given by the ratio of their respective degeneracies (2j+1). The area ratio and designations  $(n\ell_j)$  of spin-orbit doublets are given in Table 1-2.

Table 1-2. Spin-orbit splitting parameters

Subshell	<i>j</i> value		Area ratio
s	1/2		
р	1/2	3/2	1:2
d	3/2	5/2	2:3
f	5/2	7/2	3:4

The X-ray notation is almost always used for Auger transitions, so that, for example, in j-j coupling there would be six predicted KLL transitions, i.e.  $KL_1L_1$ ,  $KL_1L_2$ ,  $KL_1L_3$ ,  $KL_2L_2$ ,  $KL_2L_3$  and  $KL_3L_3$ .

#### 3. Chemical Shifts

Binding energy is the most important quantity that can be measured by XPS because of the highly useful information it provides. In a large number of cases the binding energies for an element show "chemical shifts" that are characteristic of the element's chemical state.

In some cases the chemical shifts change regularly as the oxidation state changes. For example, aluminum shows chemical shifts which proceed from low to high binding energies as the chemical state changes from Al<sup>0</sup> to Al<sup>3+</sup>. The reason that binding energies shift in this manner is because the ejected electrons from the Al<sup>3+</sup> are subject to less electron shielding from the valence electrons and a greater net positive charge from the atom than the ejected electrons from Al<sup>0</sup>. Unfortunately, binding energy chemical shifts depend on other factors such as electron relaxation and extraand intra-atomic forces, so that one cannot use them to obtain an unambiguous measure of the oxidation state.

The best way to handle chemical state determination is the Auger parameter method. This method distinguishes chemical states by observing the energy separation between the photoelectron lines

and the Auger lines of an element. The Auger parameter,  $\alpha$ , is defined by Wagner(33) as.

$$\alpha = KE(A) - KE(P)$$

in which KE(A) is the kinetic energy of the Auger electron.

KE(P) is the kinetic energy of the photoelectron.

For insulators,  $\alpha$  is independent of static charging and is characteristic of a particular chemical state. The disadvantage of this definition is that it can result in negative values. A modified Auger parameter,  $\alpha$ , is then defined as

$$\alpha' = \alpha + h\nu = KE(A) + BE(P)$$

in which BE(P) is the binding energy of the photoelectron.

The modified Auger parameter is not only independent of charging, but also is independent of the energy of the X-ray source. This eliminates the need for an outside binding energy reference because the chemical states are determined by the peak separation. rather than by the absolute binding energies.

The reason that a reference such as the C1s line is not needed when Auger parameters are used is because the chemical states are not determined by referencing to a standard binding energy. Instead, a two dimensional array can be constructed as shown in Figure 1-4 by plotting the binding energy of the most intense photoelectron line on the x-axis and the kinetic energy of the most intense Auger line on the y-axis for a series of known compounds.

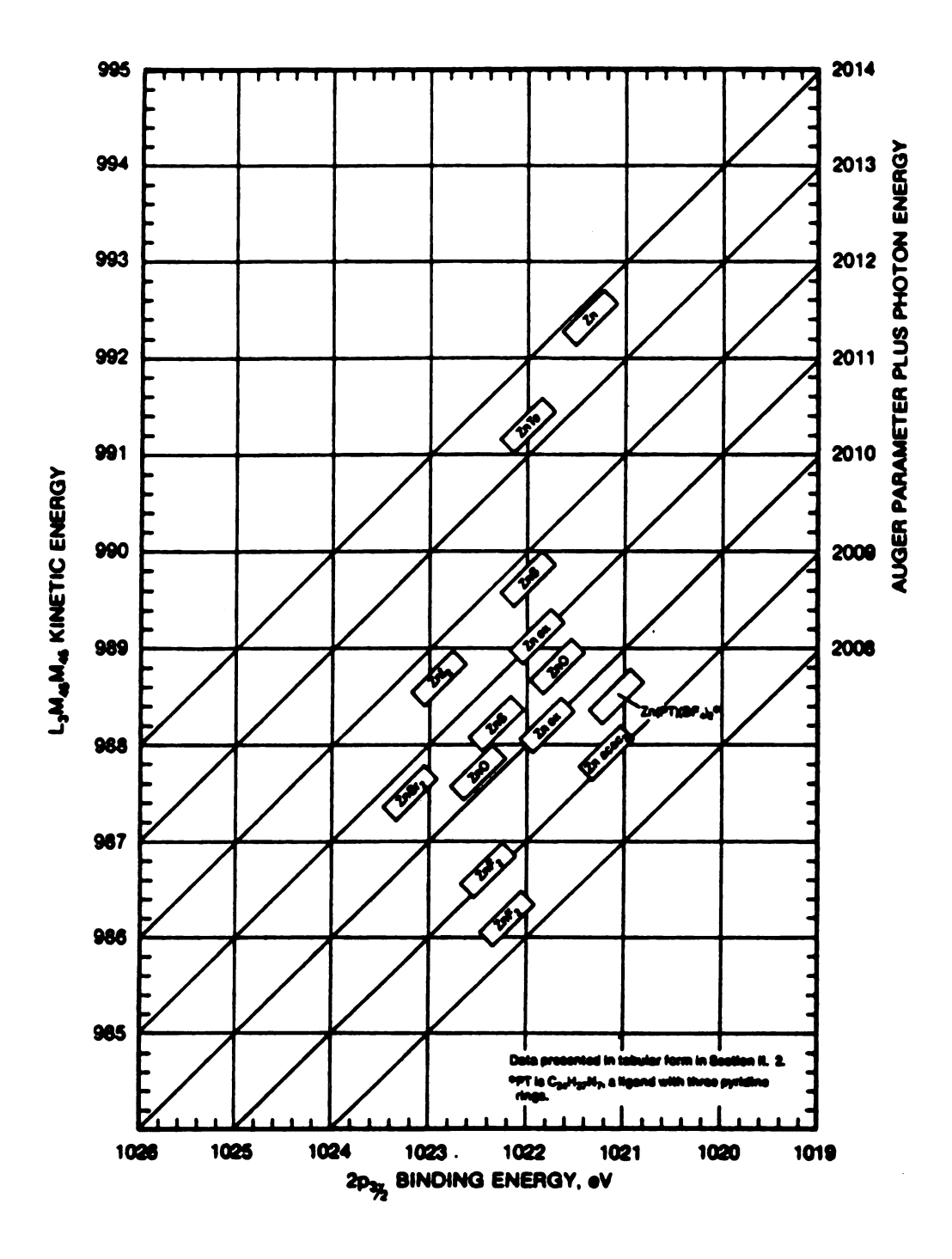


Figure 1-4 Two-dimensional zinc chemical state plot for XPS (from tabulation by C. D. Wagner, Handbook of X-ray Photoelectron Spectroscopy: Perkin-Elmer: 1979: p84)

Characterization is performed by location of a point on the two-dimensional array instead of determining the absolute binding energies from the photoelectron lines and Auger lines. Errors in charge referencing introduce uncertainty in data points parallel to the Auger parameter grid. For this reason, labels of compounds are shown as rectangles with the long dimension parallel to the grid lines. Since the function plotted is  $(\alpha + h\nu)$ , rather than  $(\alpha)$  itself, no notation of the photon energy is required and the information can be utilized with ESCA data obtained by using any X-ray source.

For example, the binding energies of the strongest photoelectron and Auger electron peaks of Zn and ZnO are 1021.4 eV (Zn  $2p_{3/2}$ ), 261.3 eV (Zn  $L_3M_{45}M_{45}$ ), 1021.6 eV (ZnO  $2p_{3/2}$ ), and 264.8 eV (ZnO  $L_3M_{45}M_{45}$ ) using Mg K $\alpha$  X-rays. There is only a 0.2 eV shift between the Zn  $2p_{3/2}$  photoelectron lines of Zn and ZnO, but the Auger parameter of zinc metal is 760.1 eV (Zn  $2p_{3/2}$  - Zn  $L_3M_{45}M_{45}$ ) while that of ZnO is 756.8 eV (ZnO  $2p_{3/2}$  - ZnO  $L_3M_{45}M_{45}$ ). Therefore, the difference between the Auger parameters of Zn and ZnO is 3.3 eV. This is much better than the 0.2 eV shift between the photoelectron peaks of Zn and ZnO.

However, the Auger parameter method is not applicable to all elements. In some cases, natural peak widths of Auger lines are larger than photoelectron lines, resulting in less accurate measurements in line shifts. At present, sufficient data for the two dimensional chemical state plots are available only for nine elements. (F. Na. Cu. Zn. As. Ag. Cd. In. and Te)

### (II). Powder X-ray Diffraction Line Broadening

Interatomic spacings in crystals are on the order of 1 Å. The wavelength of X-rays is of the same order. Hence, crystals can act as diffraction gratings for X-rays. This was first realized by von Laue in 1912 and forms the basis for the determination of crystal structures. The Bragg equation is a fundamental equation of powder X-ray diffraction, and is given by

$$2d\sin\theta = n\lambda, n=1, 2, 3,...$$

Constructive interference between waves scattered by the lattice points produces a diffracted beam of X-rays only for the angles of incidence that satisfy this equation. With the known wavelength  $\lambda$  of X-rays, the interatomic spacing d can be determined by measuring  $\theta$ . This is illustrated in Figure 1-5.

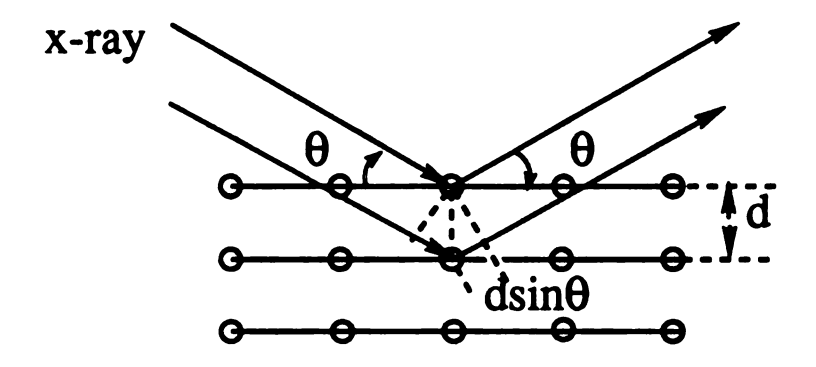


Figure 1-5. Diagram of X-ray diffraction.

If the particle sizes in the sample are less than 1000 Å, the peak width tends to be broadened and the smaller the size, the broader the peak. The average crystallite size of a powder sample can be estimated from the broadening of the powder X-ray line by using the well-known Scherrer equation

$$L_{hkl} = \frac{K \lambda}{\beta \cos \theta}$$

in which L is the average particle size along the direction of the Miller indices(hkI).

 $\lambda$  is the wavelength of the X-rays used.(eg. Cu K $\alpha$  is 1.540 Å)

K is Scherrer's constant and has a value of about 0.9.  $\theta$  is the Bragg angle.

β is the peak width at half height in radians.

Bragg has given a simplified derivation of the Scherrer equation that employs only the ordinary principles of optical diffraction. (34)

#### (III). Electron Diffraction

When a beam of electrons passes through a sample in the electron microscope, some of the electrons are deflected or scattered from the main beam in the same way as X-rays. However, the Bragg angle is much smaller, because the wavelength of the electrons is ordinarily much smaller than that of X-rays. For example, under normal operating conditions the wavelength of the electrons is 0.00370 nm when the accelerating voltage of a transmission electron microscope is 100 kV.

The diffraction pattern from a crystalline specimen is a record of the periodic structure or repeating array of that specimen. If the specimen is a single crystal (that is a single repeating array of atoms) then the diffraction pattern will consist of an array of bright spots. If the specimen consists of a large number of small discrete areas. each with exactly the same atomic array, but at different orientations to each other, the specimen is termed polycrystalline, and its diffraction pattern will consist of a series of concentric rings.

We now consider the electron microscope as a simple electron diffraction camera, with the electron beam striking a specimen and being diffracted to form a diffraction spot on the photographic plate at distance R from the center of the diffraction pattern, as shown in Figure 1-6.

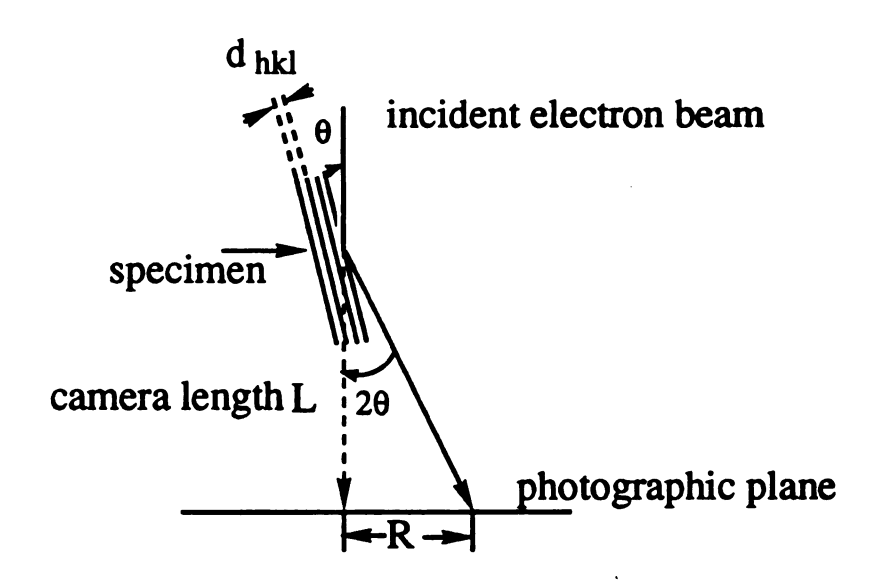


Figure 1-6. Diagram of electron diffraction.

The distance between the specimen and the plate, called the camera length, is designated by L, and by simple geometry

$$tan2\theta = R/L$$

The Bragg Law states that

 $2d\sin\theta = \lambda$ 

and since the angles  $\theta$ , through which the electrons are diffracted are very small, (only 1'-2') the approximation

$$tan2\theta \cong sin2\theta \cong 2sin\theta$$

can be made with very little error. This gives

$$R/L = \lambda/d$$

or

$$Rd = \lambda L$$
.

Thus, if values of R, L and  $\lambda$  for a particular diffraction spot or ring can be measured, the d-spacing of the lattice planes that give rise to that spot or ring can be determined.

#### D. Objective

The objective of this study was to test the generality of homogeneous reductions of soluble metal salts by solvated electrons and/or alkali-metal anions in aprotic solvents. Although many of the metals studied can be prepared as small particles by other methods, this method has the advantage of being rapid and quantitative and of requiring only low temperatures for all steps. The method has potential applicability to metal and alloy formation in the form of powders, on inert supports, and in the pores of zeolites.

Rapid reduction to the zero oxidation state produces metal particles that form colloids and aggregates with crystallite sizes that range from less than 3 nm to about 15 nm. When compounds of two different metals are used, intermetallic compounds or alloys form rather than simple mixtures of the separate metals. The initial reduction products must consist of very small, reactive particles, as

binary alloy formation is observed rather than simple mixtures of metals when two metal salts are simultaneously reduced. In this thesis. I report the formation and identification of such compounds and alloys, and the reductive preparation of some metals in zeolite pores.

#### Chapter 2 EXPERIMENTAL METHODS

#### A: Synthesis

The reduction took place in an H-cell with a medium frit as shown in Figure 2-1. The cell was attached to a vacuum line until the inner pressure was less than  $2x10^{-5}$  torr. The H-cell was then loaded into a helium-filled dry box. A small sample (1-10 mg) of the desired compound was added to the H-cell in the dry box. After removal from the dry box, the H-cell and an ampoule of presynthesized alkalide or electride (about 0.5 millimole) which had been kept cold in liquid nitrogen, were transferred to a glove bag contained a nitrogen atmosphere. The ampoule of alkalide or electride was cut off and the contents were poured into the other side of the H-cell. A liquid nitrogen bath was used to cool the cell to prevent decomposition of the alkalide or electride.

The H-cell was once again placed on the vacuum line. It was kept cold by immersion in a bath of liquid nitrogen until the cell had been pumped down to about  $10^{-4}$  torr, and then a bath of isopropanol to which dry ice had been added to keep the temperature at about -50 °C was used to keep the cell cool. About 20 mL of prepurified dimethyl ether or tetrahydrofuran was then distilled into each side.

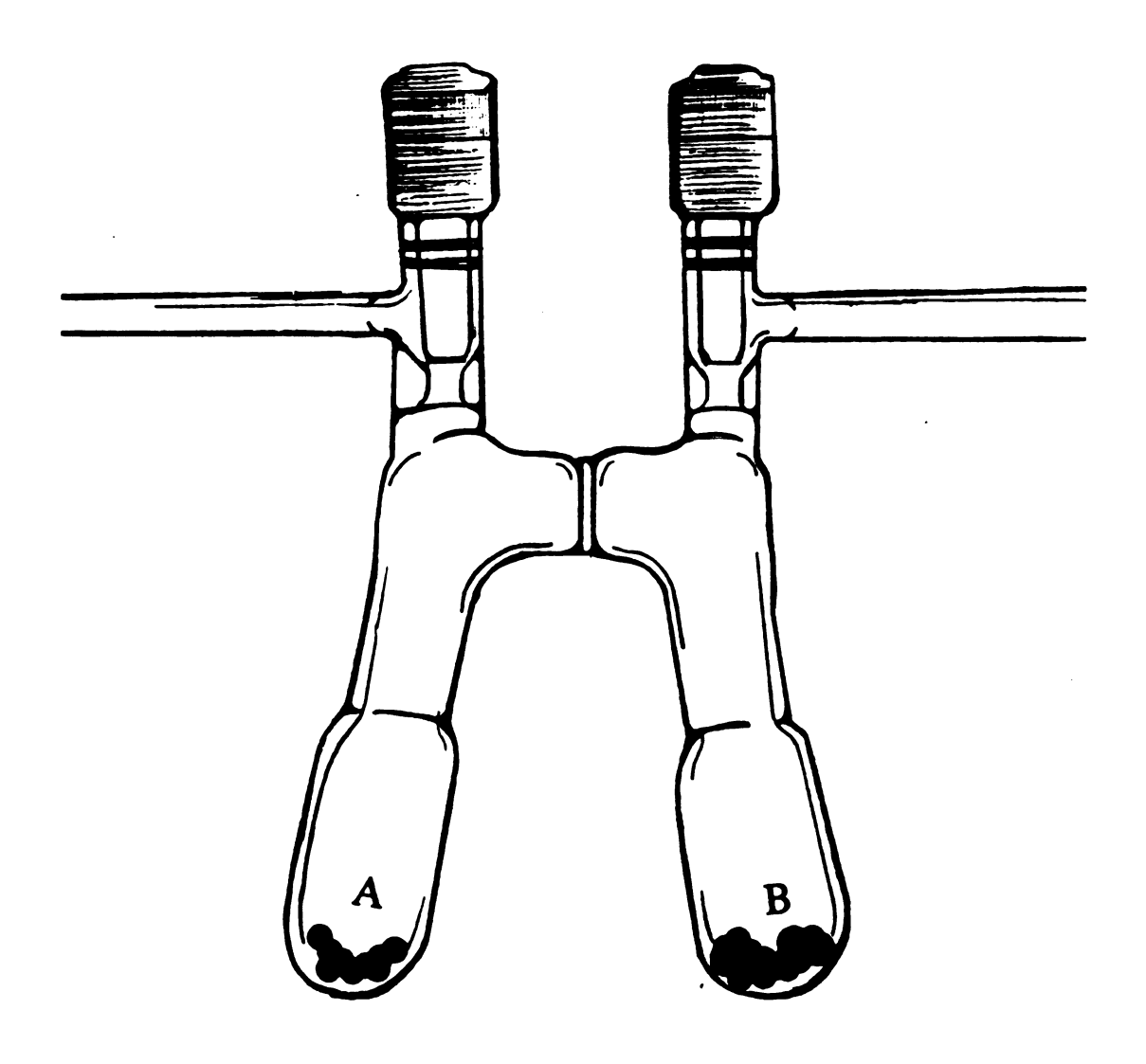


Figure 2-1.Kontes double tube("H-cell") use to prepare metal and alloy particles

The solvent had been stored under its vapor pressure after pumping out the nitrogen gas to about  $10^{-5}$  torr. (freeze-pump-thaw) Enough blue solution of the alkalide or electride was poured through the frit to react with the solution of the metal salt to be reduced after both solids had been completely dissolved in the solvent.

The reaction was complete immediately after the addition of alkalide or electride as indicated by fading of the blue color. A slight excess of alkalide or electride was added until the blue color no longer disappeared to make sure that the reaction was complete. Different colors of various colloids were formed at the same time. The solvent was then distilled off under vacuum. The products were removed from the walls of the H-cell and mounted on indium or lead foil in the He-filled dry box. A vacuum transfer vessel, which was designed to transfer chemically reactive specimens from a controlled atmosphere to an analytical system, was used to carry the sample from the dry box to the XPS transfer chamber. The pressure of the main chamber of the XPS instrument was kept below  $3x10^{-8}$  torr during measurement.

In some cases deionized and degassed distilled water or prepurified methanol was used to wash away the by-products in a glove bag. The products were removed from the cell and were placed into a test tube. About 10 mL of washing solvents was then added into the test tube inside the nitrogen-filled glove bag. Washing was performed by centrifugation to separate the undissolved metallic particles from the water- or methanol- soluble by-products. XRD patterns were recorded by placing the the precipitate on a glass slide either with or without washing. A drop of

washed suspension was put on the TEM carbon-coated grid and allowed to dry in the air. after which TEM micrograghs. EDS and electron diffraction patterns were made.

The aprotic solvents Me<sub>2</sub>O or THF were distilled from solutions of excess Na-K and benzophenone into stainless-steel (Me<sub>2</sub>O) or glass (THF) storage vessels. Liquid 15C5 crown ether was purified by distillation. All the alkali metals and metal salts were purchased from Aldrich or AESAR in the highest available purity without any further purification. Liquid samples were  $TiCl_4(99.995+\%)$ .  $GeCl_4(99.999\%)$ .  $SiCl_4(99.999\%)$ .  $SbCl_5(99\%)$  and  $SnCl_4(99.999\%)$ . Solid samples were  $CuCl_2(99.9999\%)$ .  $GaCl_3(99.99+\%)$ .  $Znl_2(99.99\%)$ .  $MoCl_5(99.99\%)$ .  $FeCl_3(98\%)$ .  $H_2PtCl_6(99.9\%)$ .  $InCl_3(99.999\%)$ .  $TeBr_4(99\%)$ .  $WCl_6(99.9+\%)$ .  $AlCl_3(99.99\%)$ .  $VCl_3$  and  $AuCl_3$ . The oxide support was neutral activated  $Al_2O_3$  with a specific surface area of 155 m<sup>2</sup>/g and 150 mesh size. Either a 0.25 mm thick 99.99+% indium foil or a 0.5 mm thick 99.99% lead foil was used to mount the samples for XPS studies.

## B. X-ray Photoelectron Spectroscopy

X-ray Photoelectron Spectroscopy (XPS) or Electron Spectroscopy for Chemical Analysis (ESCA) was performed with a Perkin-Elmer PHI 5400 ESCA/XPS spectrometer system. Its analyzer is a Spherical Capacitor Electron Energy Analyzer (SCA) with an Omni-Focus II lens and a small area lens (200 µm dia to 3 mm x 10 mm with 4 selectable apertures). This permits efficient small area analysis without sacrificing overall system analytical flexibility for

Auger parameter and photon dependent depth profiling studies. Unlike a focused X-ray source, the small spot ESCA design gives an energy resolution that is independent of the analysis area.

The most commonly used anode material for ESCA/XPS is magnesium which has a K $\alpha$  X-ray energy of 1253.6 eV. It has a narrow natural X-ray line width which facilitates chemical species interpretation and is a highly efficient source of X-rays at moderate power. Photoelectron lines generated by Mg K $\alpha$  X-rays are narrower and more intense than the same lines generated by any of the other commonly used non-monochromated X-ray sources.

The system is also equipped with a monochromator to deliver the highest available energy resolution, in which case, Al Kα (1486.6 eV) X-rays are used. The monochromator provides maximum X-ray collection efficiency for unsurpassed counting rates. This monochromator X-ray source works with the SCA and Omni-Focus II lens to also provide high signal-to-background ratios for superior trace element detection, sharp, narrow line widths for enhanced chemical speciation, and the elimination of unwanted satellite lines for unambiguous data interpretation. All data were recorded by scans at 15 KV. The power of the X-ray sources was 600 W for Al Kα and 400 W for Mg Kα.

A vacuum transfer vessel was used to transfer chemically reactive specimens from a controlled atmosphere to the analytical system. or from one system to another without atmospheric exposure. The specimens were transported under an inert gas atmosphere or under vacuum. This vacuum transfer vessel allows one to transport a sample of all products of the reduction from the

helium filled dry box to the introduction system of the XPS without oxidation.

There is also a differential ion gun on the XPS system to generate an energetic ion beam for sputter etching of solid surfaces. During operation, an inert gas such as argon is bled into the gun ionization chamber. A heated tungsten filament emits electrons which are attracted to a positively biased grid and accelerated through the gas in the chamber.

lons are created by electron impact within the ionization chamber, extracted from the chamber toward the focusing and deflection lenses, and directed onto the specimen. When the surface is oxidized, this argon ion sputtering technique is used to probe the sub-surface composition.

# C. Powder X-ray Diffraction

Powder X-ray diffraction (XRD) provides direct evidence for metal particle formation when the crystallite size is greater than 3 nm. The width of the strongest XRD line can be used with Scherrer's equation to determine the average size for crystallites between 3 and 20 nm.

For X-ray amorphous metals, common in this work, XRD only provides an upper size limit of about 3 nm, but cannot be used to verify metal formation. The by-product salts were always crystalline, so that XRD provides a convenient measure of the efficiency of removal of these salts. By contrast, organic decomposition products are not usually detectable by XRD.

A Rigaku D/max-RBX rotating-anode diffractometer equipped with a scintillation counter detector and a graphite monochromator to yield Cu K $\alpha$  (wavelength 1.54184 Å) radiation was used under the control of a DEC Microvax computer. All data were recorded by scans at 45 KV and 80 m A.

# D. Transmission Electron Microscopy

Transmission Electron Microscopy (TEM) was used to obtain particle sizes and the morphology of aggregation. A JEOL 100 CX II transmission electron microscope operating at 100 KV was used for imaging, energy dispersive spectra (EDS) and selective area electron diffraction (SAD).

It was not possible to prevent air oxidation with the instrument used, so that reactive metals could not be directly observed in the TEM. But the particle size distribution of the products of oxidation could be studied. It was also possible with this instrument to obtain elemental analyses of microscopic crystallites by EDS. This allowed us to verify the presence of both components of an alloy and to identify regions that contain only one metallic element. For products that could be briefly exposed to air, SAD provided identification of the structure.

# Chapter 3 SINGLE ELEMENT REDUCTION

#### A. Reduction with Alkalides or Electrides

Alkalides and electrides owe their parentage to alkali metal solutions in ammonia, amines and polyethers.(35) The species e-solv and M- have been extensively studied in solution.(36.37.38) Indeed, reductions that involve such species ("dissolving metal reductions") have been used in the laboratory and industrially for many years. The unique feature of alkalides and electrides is the ability to produce stoichiometric crystalline salts in which trapped electrons or alkali metal anions serve as the anions. This is achieved by using powerful cation complexants such as crown ethers or cryptands to protect the alkali cation from reduction by e-solv or M-. To first order, most solid alkalides and electrides may be viewed as close-packed large (8-10 Å diameter) cations with e-solv or M- in the holes that are produced by such packing.

The organic complexant not only permits isolation of solventfree crystalline alkalides and electrides, but also serves to greatly enhance the solubility of alkali metals in such aprotic solvents as Me<sub>2</sub>O and THF. The relevant equilibria are:

$$M(s) = \frac{27}{M \text{ solv}} + e \text{ solv} \qquad (1)$$

$$2 M(s) \longrightarrow M_{solv} + M_{solv}$$
 (2)

$$M \stackrel{+}{solv} + nL \longrightarrow M \stackrel{+}{}(L)n$$
 (3)

in which L is the complexant and n is 1 or 2. Reaction 3 lies far to the right, which tends to drive reactions 1 and 2 to the right also. The effect on metal solubility is dramatic. For example, potassium is not perceptibly soluble in Me<sub>2</sub>O ( $10^{-5}$  M solutions would be easily discernable by eye because of the intense colors of  $e^-$ solv or  $M^-$ ). In the presence of stoichiometric amounts of 15C5, at least 0.5 M solutions of  $K^+(15C5)_2K^-$  are formed at -25 °C. The solubility is presumably even higher than this since no precipitate forms upon cooling this solution to -78 °C. This dissolution process is slow, however, and potassium powder or films require about one hour at -25 °C to form concentrated solutions. By contrast, pre-synthesized alkalides and electrides dissolve rapidly.

The solvated electron (e-solv) is thermodynamically the most powerful reducing agent possible in a given solvent. It also usually reacts rapidly with metal ions and with simple compounds that contain a metal in a positive oxidation state. Alkali metal anions.

M-, are nearly as effective and can provide two electrons in a single encounter. Side reactions with the solvent arise, however, when protic solvents such as ammonia or a primary or secondary amine is used.(39)

A solution that contains  $e^-solv$  or  $M^-$  in an aprotic solvent is an attractive reducing medium. The alkali metals are solubilized in

a suitable cation complexant such as a crown ether or a cryptand. (40.41.42.43) The resulting homogeneous solutions contain either e-solv or M- depending on the metal/complexant ratio. (44) Identical solutions are prepared by dissolving pre-synthesized electrides or alkalides in the solvent. When a metal salt or complex are dissolved in the same solvent, rapid reduction to the metal can occur upon mixing the two solutions.

## B. Reducing agents

Six alkalides and two electride were used as reducing agents. These include:  $K^+(18C6)Na^-$ .  $Cs^+(18C6)_2Na^-$ .  $Cs^+(15C5)_2Na^-$ .  $Rb^+(15C5)_2Na^-$ .  $K^+(15C5)_2K^-$ .  $Rb^+(15C5)_2Rb^-$ .  $K^+(15C5)_2e^-$ . and  $Cs^+(15C5)_2e^-$ . It is not important which alkalide or electride is used since it simply acts as an electron donor. There is no perceptible difference in the reducing ability among them as the blue colors of the alkalide or electride solution disappear immediately when the reaction occurs. The compounds  $K^+(15C5)_2K^-$  and  $K^+(15C5)_2e^-$  were most often used as reductants because of their high solubilities and ease of preparation.

#### C. Results

This work presents a new method for preparation of small metal/oxidized metal particles that utilizes homogeneous reduction by dissolved alkalides or electrides in an aprotic solvent such as

dimethyl ether or tetrahydrofuran. (45) Salts of Au. Pt. Cu. and Te form metallic particles with little or no oxidation even when washed with methanol. Reduction of salts of Ni. Fe. Zn. Ga. Si. Mo. W. In. Sn. Cd. and Sb yields surface oxidation over a a metallic core. while only oxidized Ti was observed.

The procedure for the preparation of small metal particles was described in Chapter 2. While nearly any soluble metallic compound is reduced by alkalides or electrides in Me<sub>2</sub>O or THF, the less reactive noble metals. Au. Pt. etc., are easiest to isolate and characterize. Gold was used to test the method and to develop the methodology because AuCl<sub>3</sub> is highly soluble in Me<sub>2</sub>O and can be easily obtained as the anhydrous compound, and because the product. Au metal, does not oxidize easily when exposed to the air while almost all other metals do when they are in the nanophase state.

## (I) Gold

AuCl<sub>3</sub> was reduced by  $K^+(15C5)_2K^-$  or  $K^+(15C5)_2e^-$  in Me<sub>2</sub>O or THF. The reaction stoichiometries such as

2 AuCl<sub>3</sub> + 3 K<sup>+</sup>(15C5)<sub>2</sub>K<sup>-</sup> 
$$\frac{\text{Me}_2\text{O}}{2}$$
 2 Au + 3 K<sup>+</sup>(15C5)<sub>2</sub>Cl<sup>-</sup> + 3 KCl and AuCl<sub>3</sub> + 3 K<sup>+</sup>(15C5)<sub>2</sub>e<sup>-</sup>  $\frac{\text{Me}_2\text{O}}{2}$  Au + 3 K<sup>+</sup>(15C5)<sub>2</sub>Cl<sup>-</sup>

were verified by XRD studies of reaction products after solvent removal by distillation. The by-products, K<sup>+</sup>(15C5)<sub>2</sub>Cl<sup>-</sup> and/or KCl. were washed away by methanol or water. The remaining black **Products** are pure small metallic gold particles confirmed by XPS.

XRD. SAD. and EDS. AuCl3 was reduced 11 times and the results were reproducible.

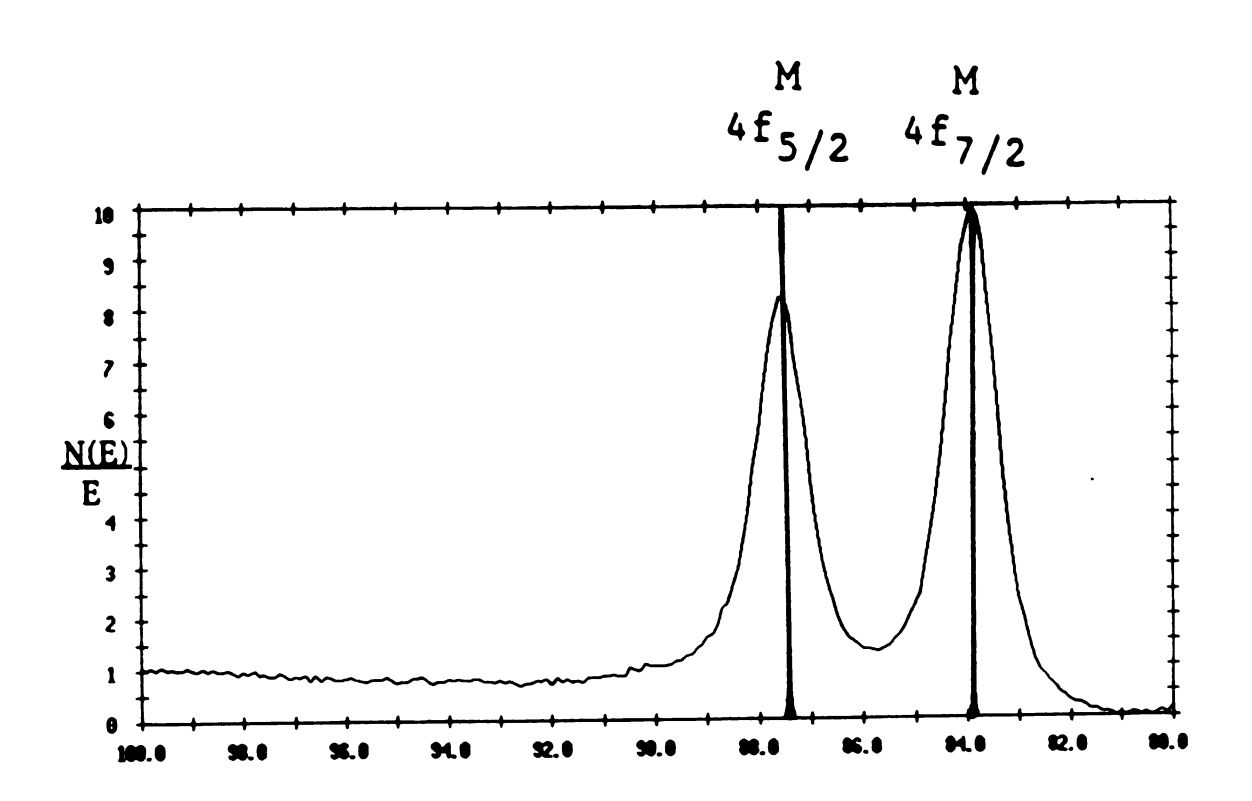
For crystalline particles of average diameter larger than 3 nm. the mean diameter was determined by applying Scherrer's equation to the XRD line widths. TEM micrographs were also used to determine particle size and size distribution. EDS permitted analysis, and SAD was used to identify the bulk structure of the particles. XPS (photoelectron and Auger peaks) identified the surface composition (metallic or oxidized), and when necessary, argon ion sputtering removed the surface layer to verify the presence of subsurface metal.

Crystallite sizes (and particle sizes) were of the order of 10 nm. so that XRD identification was possible. When dilute solutions ( $10^{-2}$  to  $10^{-3}$  M) of AuCl<sub>3</sub> were reduced, colloidal gold that only slowly precipitated was formed in Me<sub>2</sub>O. The particle size was smaller when more dilute solutions were used. After removal of Me<sub>2</sub>O by distillation, the residue again formed a colloidal solution when taken up in water.

Figure 3-1 shows the XPS spectrum of Au  $(4f_{7/2} \text{ and } 4f_{5/2})$  from the product of reduction of AuCl<sub>3</sub>. The binding energies of both the Au  $4f_{7/2}$  state at 83.70 eV and the  $4f_{5/2}$  state at 87.30 eV show that the product is pure metallic gold.(46)

Figure 3-2 shows typical XRD lines that were used to determine average particle sizes for Au. The average particle size estimated from the line width and Sherrer's equation is 10 nm. Figure 3-3 shows the size distributions for Au from an electron micrograph (Figure 3-4). There is very good agreement between the average

The SAD patterns shown in Figure 3-5 were also taken on the same area. All the rings in Figure 3-5 were converted to d-spacings and were compared to a standard XRD Au file as shown in Table 3-1.



Binding Energy, eV

Figure 3-1. XPS spectrum of Au from the product of reduction of AuCl<sub>3</sub>.

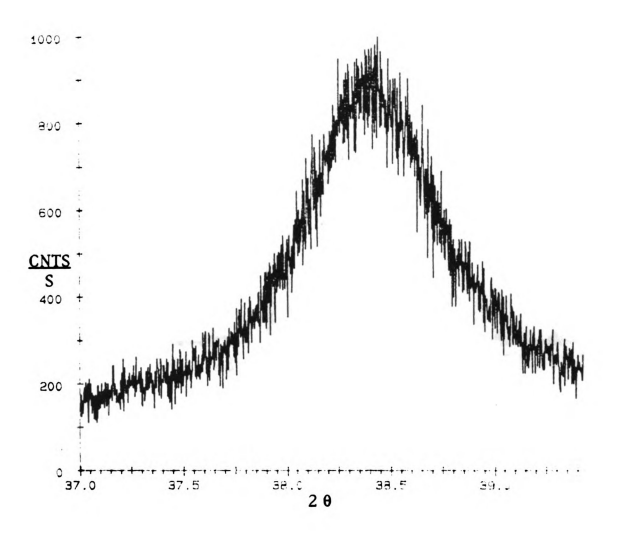


Figure 3-2. XRD lines(111) used to determine average particle sizes for Au.

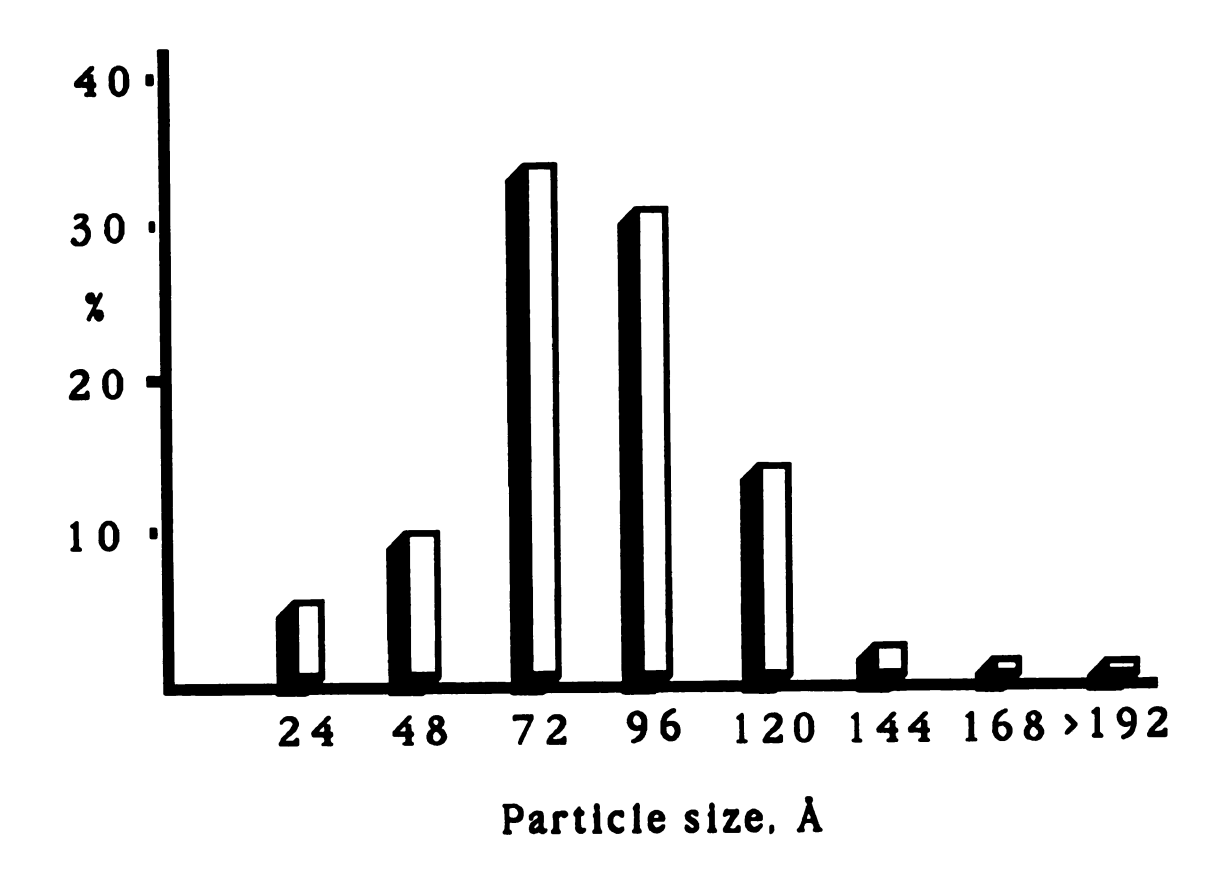


Figure 3-3. Particle size distributions for Au.



Figure 3-4. Electron micrograph of Au.(mag=100,000X, 1,000 Å/cm)

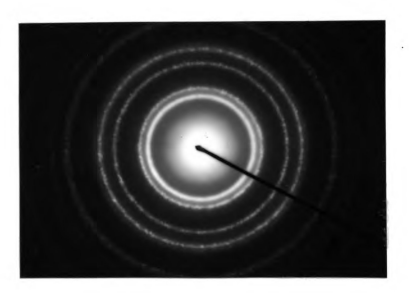


Figure 3-5. Selected area electron diffraction of Au. (camera length=83 cm)

. . . . . . . . . . . . . . . .

91.275

The state of the s

Table 3-1. Electron diffraction of Au from reduction of AuCl3.

	D(cm) <sup>a</sup>	d(Å)b	d/d'C	d'(Å)d	hkle
1	2.74	2.24	0.952	2.355	111
2	3.14	1.96	0.959	2.039	200
3	4.51	1.36	0.944	1.442	220
4	5.28	1.16	0.943	1.230	311
5	5.57	1.10	0.934	1.1774	222
6	6.44	0.954	0.935	1.0196	400
7	6.98	0.880	0.940	0.9358	331
8	7.18	0.855	0.938	0.9120	420
9	7.84	0.783	0.941	0.8325	422

- a. Ring diameter of electron diffraction. (camera length = 83 cm)
- b. d-spacing converted from ring diameter.
- c. d-ratio from electron and powder X-ray diffraction.
- d. d-spacing from powder X-ray diffraction files.(4-0784)
- e. Miller index.

This method was also used to prepare highly dispersed metals on oxide surfaces as previously done by other methods. (47) To verify this. AuCl<sub>3</sub> in Me<sub>2</sub>O was adsorbed on neutral activated Al<sub>2</sub>O<sub>3</sub> (155 m<sup>2</sup>/g) and reduced with  $K^*(15C5)_2K^-$  in Me<sub>2</sub>O. Au particles (about 6 nm average diameter) were randomly dispersed on the surface as shown in Figure 3-6. One may be able to prepare a large surface area metal oxide catalyst by co-reduction of a noble metal and an active metal. followed by oxidation of the latter. It should be also possible to prepare organometallic compounds by reaction of suitable precursors with freshly prepared active metals.

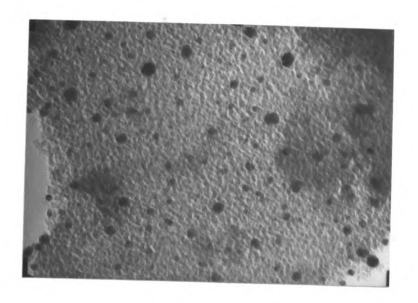


Figure 3-6. Electron micrograph of Au particles on Al2O3.  $(mag\text{=}190.000X,\,550\,\text{Å/cm})$ 

A gold colloidal solution was formed by adding water to the reaction products after distilling out the Me<sub>2</sub>O. The average diameter of Au produced in this way was about 10 nm as determined from XRD. The optical absorption spectra of a gold colloid solution (ruby red) is shown in Figure 3-7. The 520 nm peak was assigned to surface plasmon absorption by Abe et al.(48) This colloid is very stable over a period of several months. This optical peak was also found in deposited particles (12 nm diameter) in glass.(49)

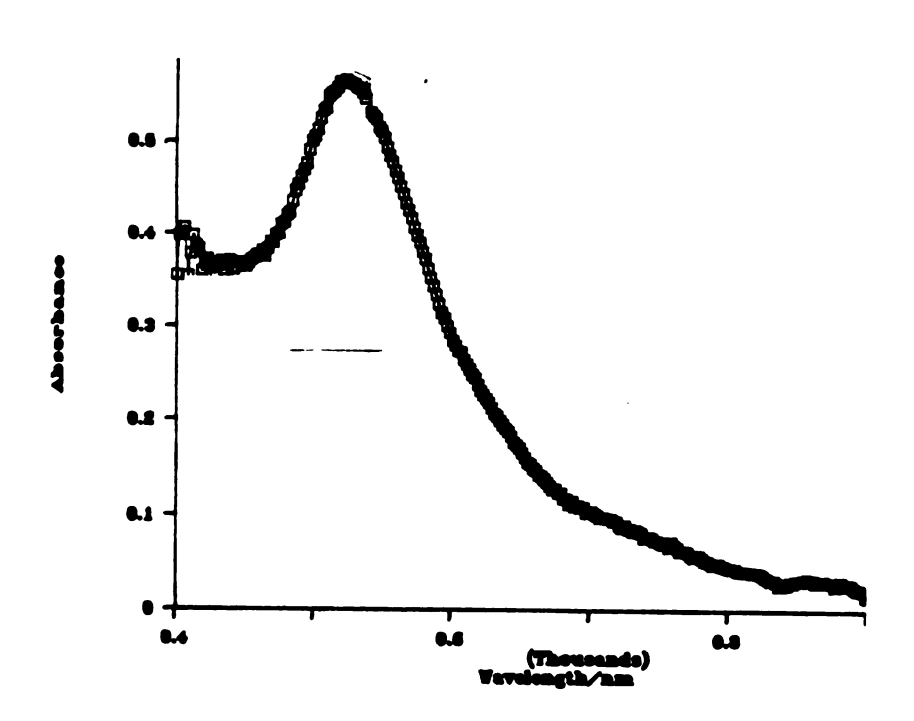


Figure 3-7. Optical absorption spectra of an Au colloidal solution.

In an attempt to control the particle size, two AuCl<sub>3</sub> solutions with different concentrations were reduced with  $K^+(15C5)_2K^-$  in Me<sub>2</sub>O and the products were collected by distilling out solvent. The XRD data showed that the higher concentration formed larger particles of Au. A  $1.6 \times 10^{-4}$  M AuCl<sub>3</sub> solution formed 5.8 nm Au particles while the higher concentration  $(6.5 \times 10^{-4} \text{ M})$  formed larger Au particles (10.5 nm) as shown in Figure 3-8. However, the byproduct crystallite sizes remained almost the same even when different Au particle sizes formed. This was verified by the same peak height and width from KCl (111) at  $20 = 40.5^+$ .

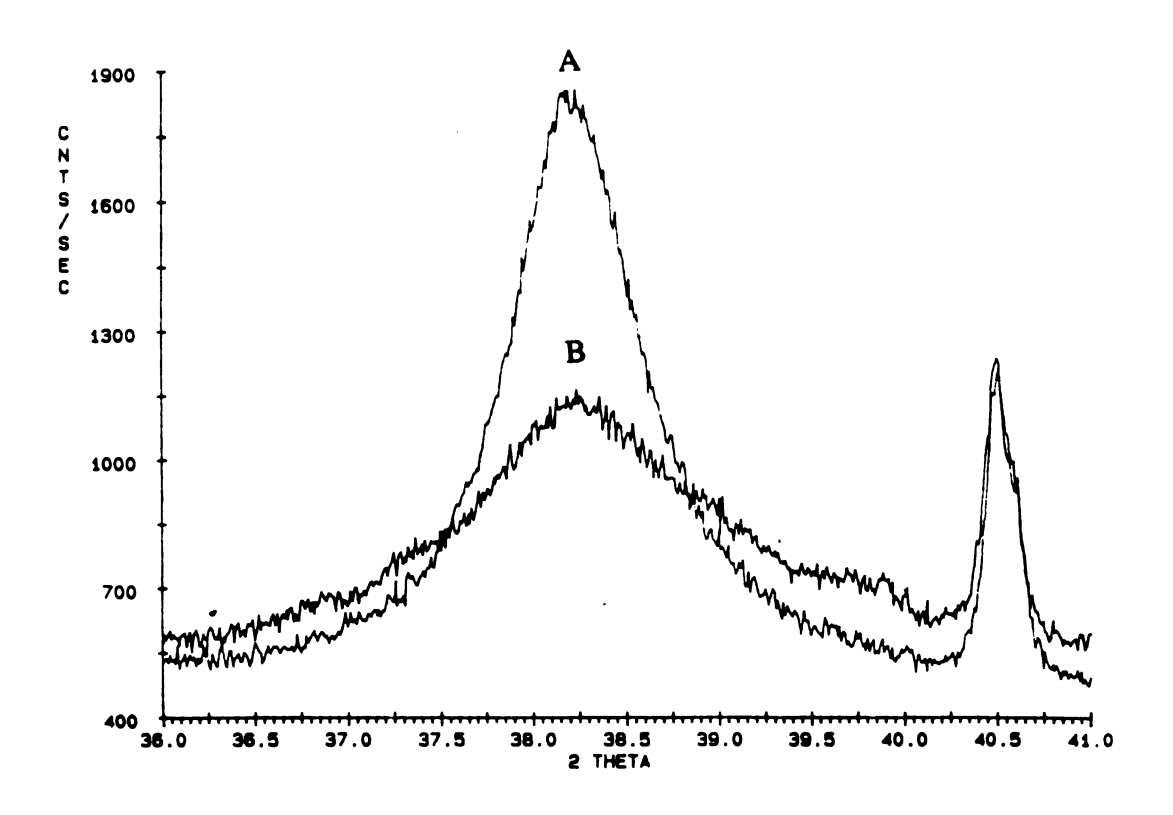


Figure 3-8. XRD spectrum of the products from the reduction of AuC13. (A=6.5x $10^{-4}$  M. B=1.6x $10^{-4}$  M)

By using all of the characterization techniques described above. it was often possible to identify the major phase or phases resulting from reduction and to obtain particle size information. But the high reactivity of nanoscale metal particles and the presence of organic complexants and solvents often resulted in the inclusion of organic decomposition products.

FT-IR spectroscopy was used to demonstrate their presence and to identify major IR-active groups on the surface of the metal particles as shown in Figure 3-9. The following peak positions were identified: 611(C-H or O-H), 1089 and 1117(C-O), 1385(major impurity from KBr), 1634(O-H), 2852 and 2925(C-H), and 3448(O-H). A sample of washed Au particles was also sent to Galbraith Laboratories, Inc. for chemical analysis and it was found that carbon was 0.70 % and hydrogen was < 0.5 % in atomic percent concentration.

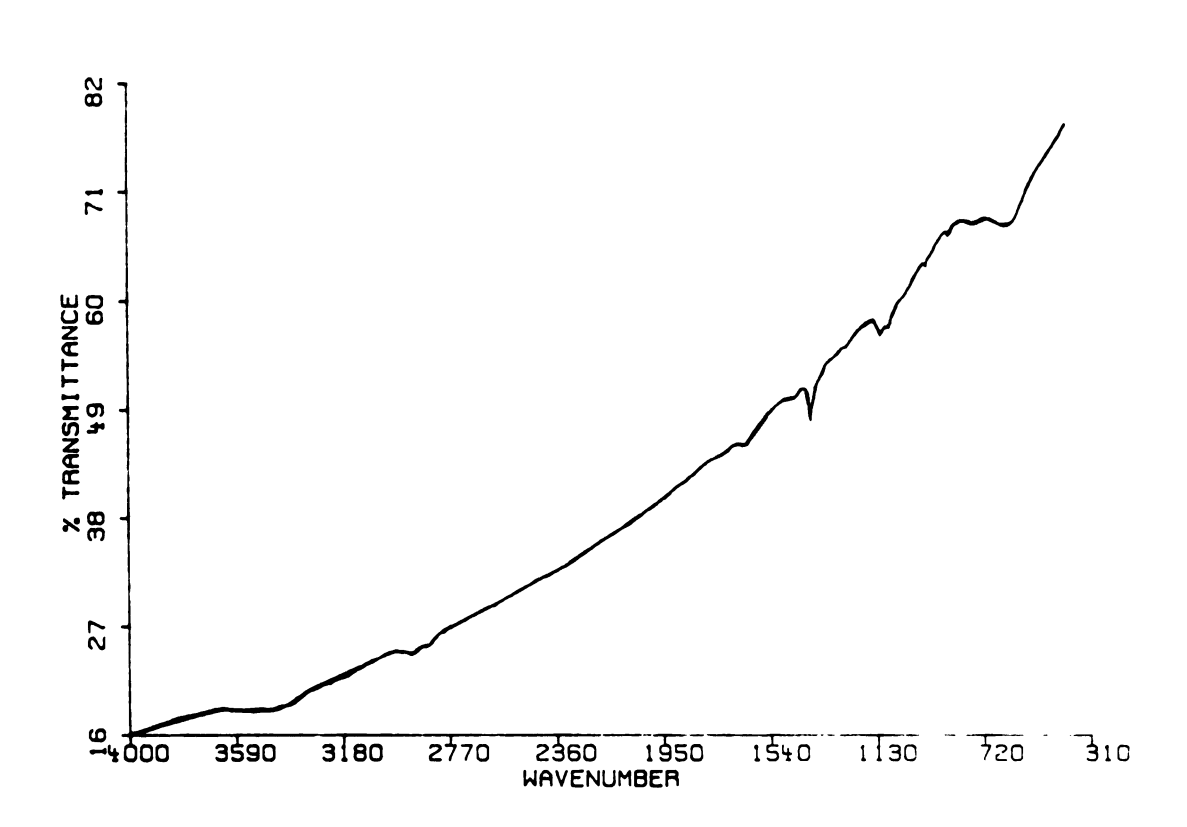


Figure 3-9. FT-IR spectra of washed Au particles.

# (II) Copper

Although bulk copper is very stable in the air, it is easily oxidized at room temperature when the particles are of nanometer size. CuCl<sub>2</sub> was reduced in Me<sub>2</sub>O by the present method to produce small metallic copper particles. These were fully characterized by x-ray powder diffraction, electron diffraction, and x-ray photoelectron spectroscopy. Only metallic copper peaks were detected by XRD from the precipitates after washing away the by-products. The mean particle size of the strongest peak of Cu(111) from the XRD line broadening, as shown in Figure 3-10, was about 57 Å after washing with methanol.

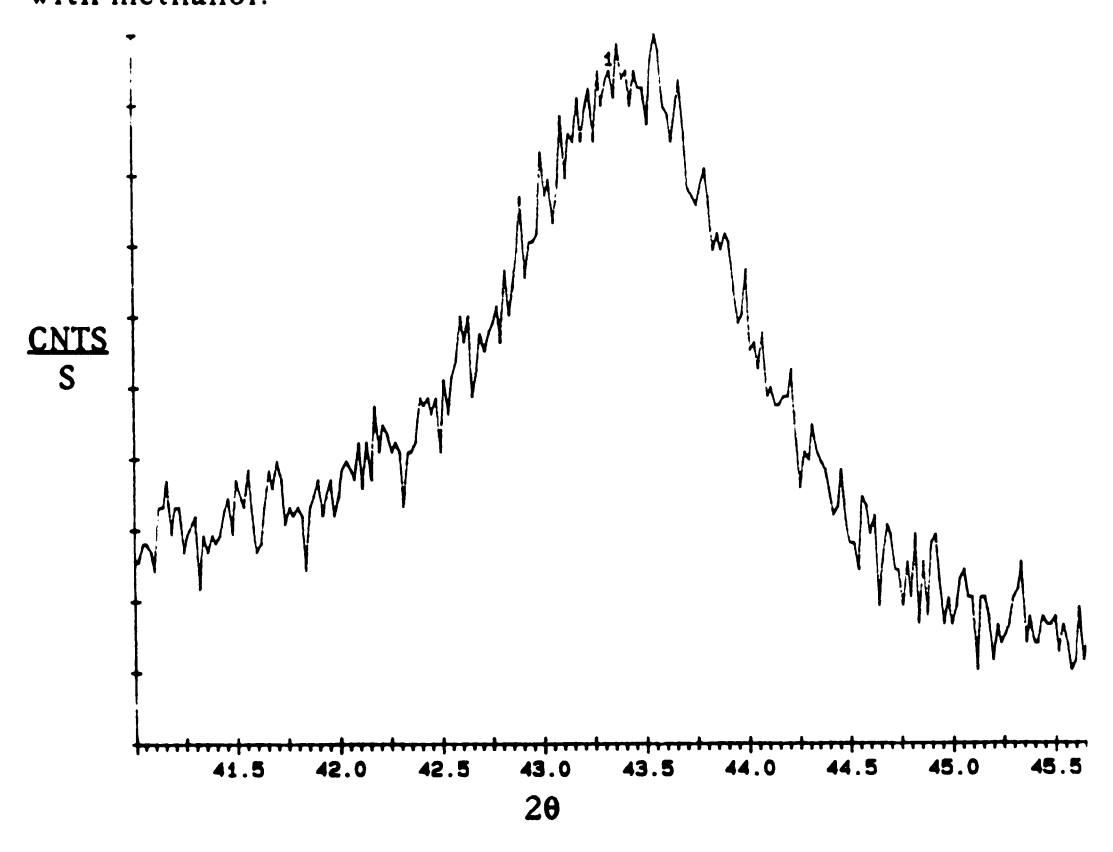


Figure 3-10. XRD lines(111) used to determine average particle sizes for Cu.

Figure 3-11 shows the characteristic electron diffraction pattern of metallic copper, with lines (111), (200), (220), (311) giving rise to rings from inner to outside rings. All the rings in Figure 3-11 were also converted to d-spacings and were compared to a standard XRD Cu file as shown in Table 3-2.

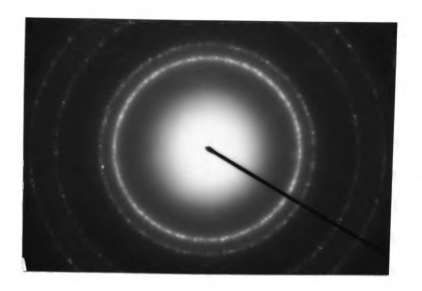


Figure 3-11. Selected area electron diffraction of Cu. (camera length = 140cm)

Table 3-2. Electron diffraction of Cu from reduction of CuCl2

	D(cm)a	d(Å)b	d/d'c	d'(Å)d	hkle
1	4.93	2.10	1.0057	2.088	111
2	5.66	1.83	1.0120	1.808	200
3	8.02	1.29	1.0094	1.278	220
4	9.38	1.10	1.0092	1.090	311
5	9.81	1.06	1.0153	1.044	222

- a. Ring diameter of electron diffraction. (camera length = 140cm)
- b. d-spacing converted from ring diameter.
- c. d-ratio from electron and powder X-ray diffraction.
- d. d-spacing from powder X-ray diffraction files.(4-0836)
- e. Miller index.

The electron micrograph of Figure 3-12 agrees well with the average particle size of 57 Å obtained from the XRD line broadening of the metallic Cu product from the same run. Figure 3-13 shows the particle size distribution of these metallic copper particles. These particles were also characterized by energy dispersive spectroscopy as shown in Figure 3-14. Only Cu peaks appear on the Ni grid.

The small Cu particles were also characterized by XPS and only the  $2p_{3/2}$  peak at 932.6 eV and the  $2p_{1/2}$  peak at 952.4 eV appear in Figure 3-15-A (before washing) and Figure 3-15-C (after washing away by-products with methanol). Figure 3-15-B shows that a small amount of CuO is present on the Cu surface after exposing the sample to air for 24 hours.

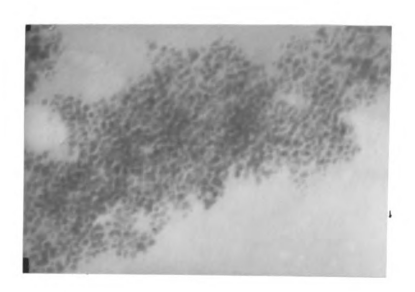


Figure 3-12. Electron micrograph of Cu. (mag=320.000X, 310Å/cm)

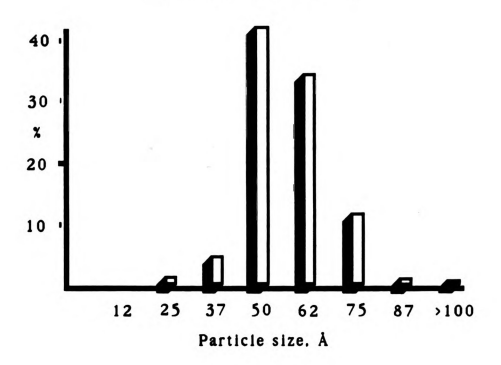


Figure 3-13. Particle size distribution of Cu.

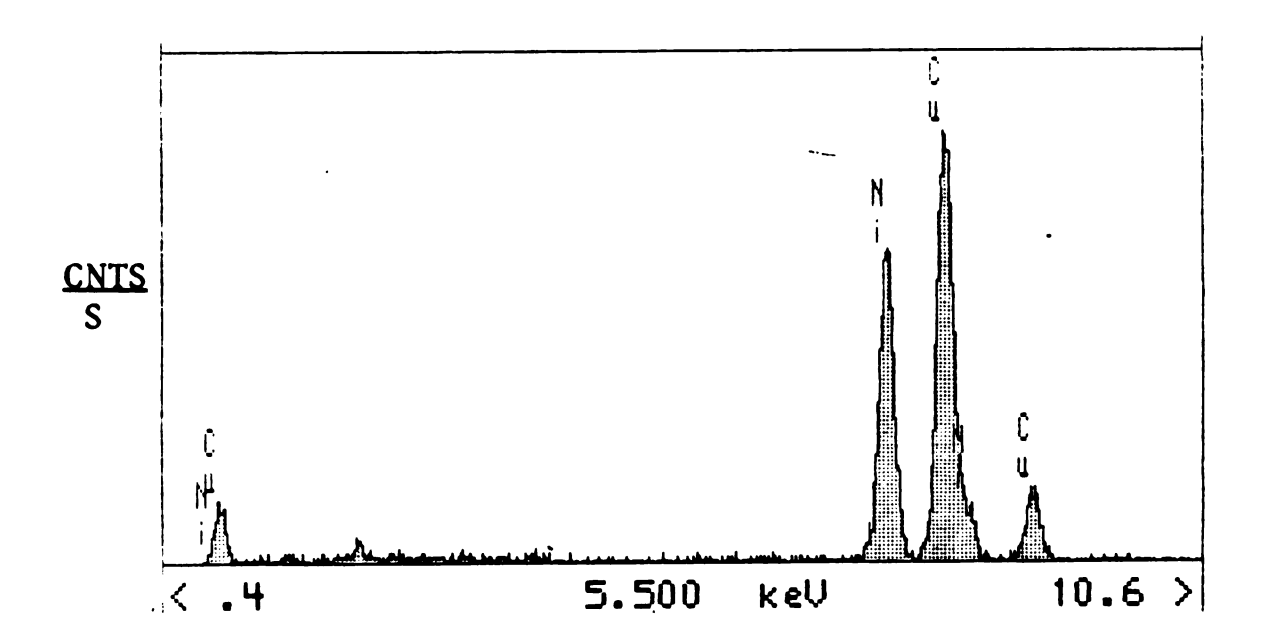


Figure 3-14. Energy dispersive spectra of Cu particles on Ni grid.

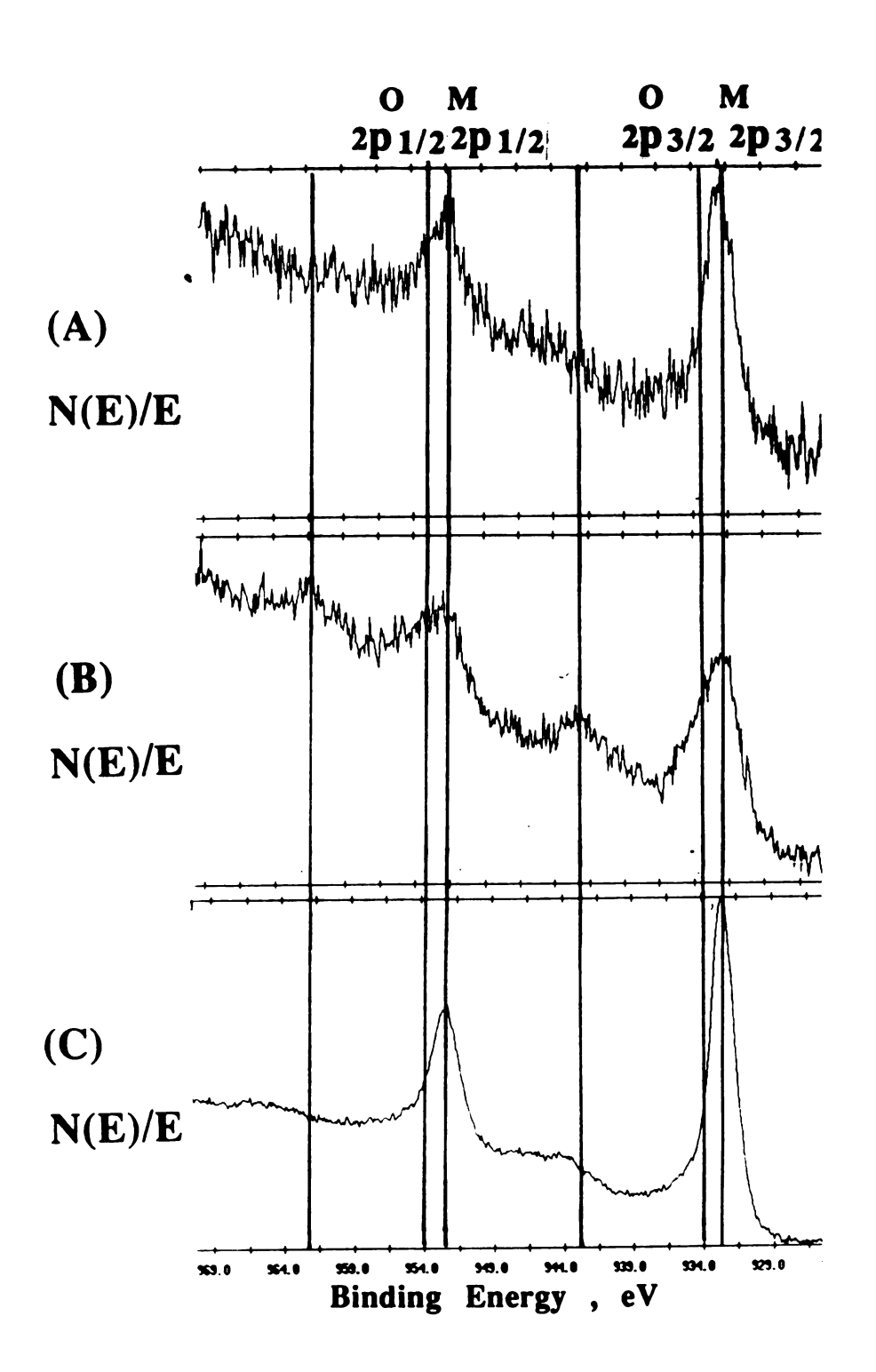


Figure 3-15. XPS spectrum of Cu (A before washing, B exposed to air for 24 hours, and C after washing)

### (III) Tellurium

TeBr<sub>4</sub> was reduced by  $K^+(15C5)_2e^-$  in dimethyl ether. Figure 3-16-A shows the XPS results of the  $3d_{5/2}$  and  $3d_{3/2}$  peaks of metallic Te before washing. After oxidizing these products in air for 3 min. the oxide peaks were larger than the metal peaks as shown in Figure 3-16-B. These particles were partially oxidized after washing with methanol as shown in Figure 3-16-C. Clean metallic Te peaks were observed in another methanol-washed product.

Only metallic Te peaks were observed by powder X-ray diffraction. Although the average particle size estimated from line broadening in Figure 3-17 for Te (101) is 117 Å (line width at half height  $\beta$  = 0.7), the micrograph (Figure 3-18) shows interesting rod-like shapes. The electron diffraction pattern (Figure 3-19) shows the hexagonal structure of metallic Te with a=4.46 Å and c=5.93 Å. All the rings in Figure 3-19 were converted to d-spacings and were compared to a standard XRD Te file as shown in Table 3-3.

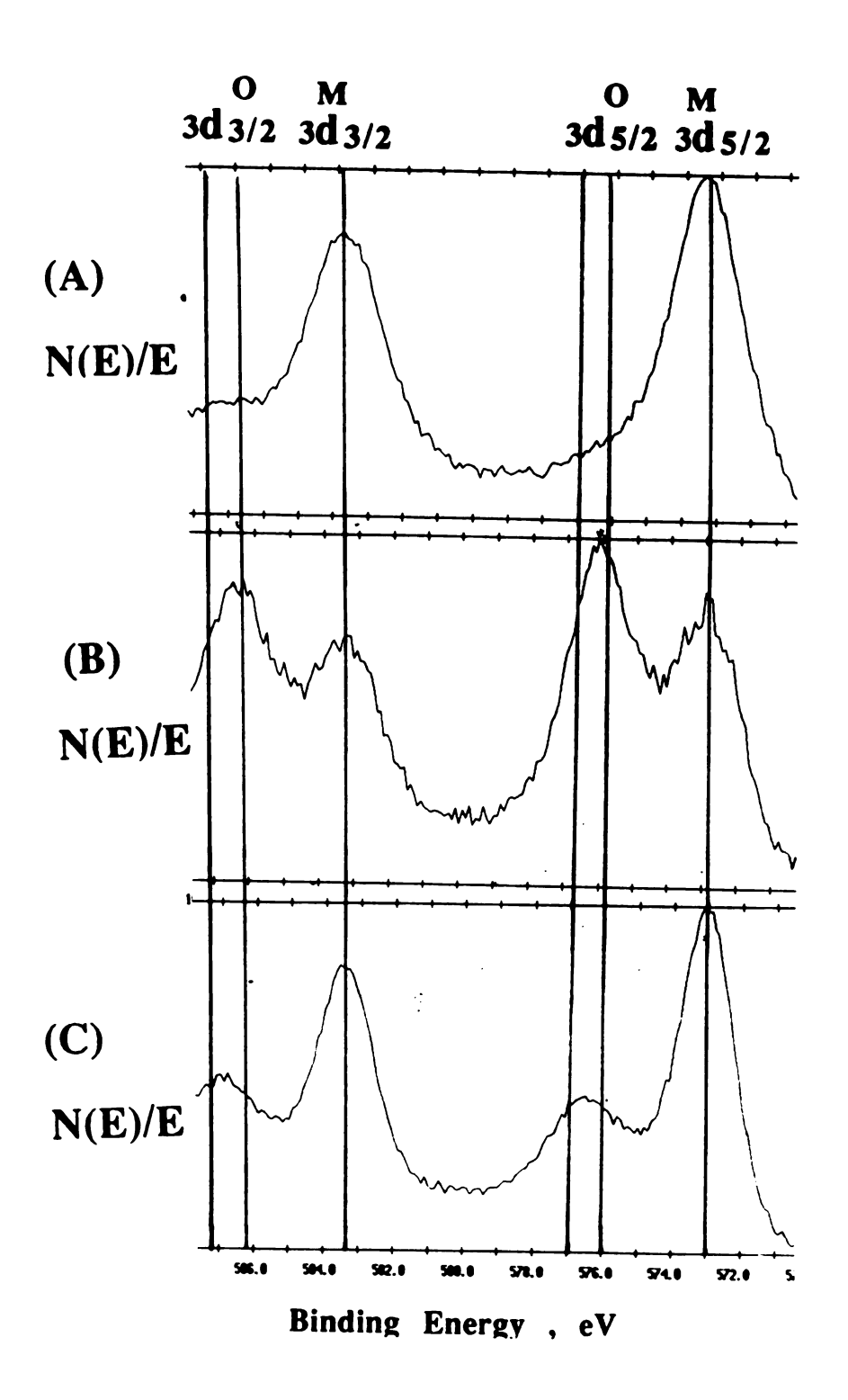


Figure 3-16. XPS spectrum of Te (A before washing, B exposed to air for 3 min. and C after washing)

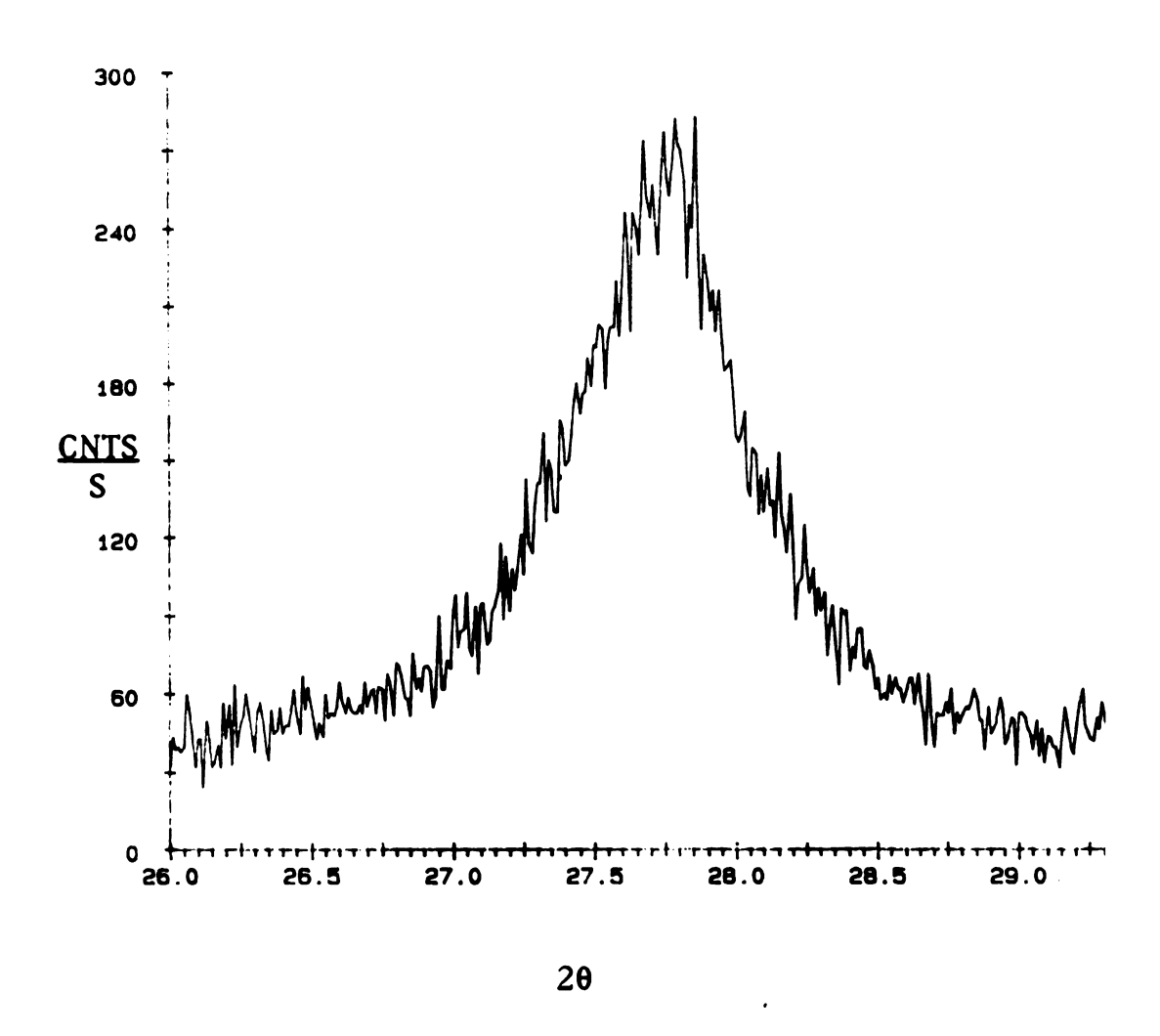


Figure 3-17. XRD lines(100) used to determine average particle sizes for Te.

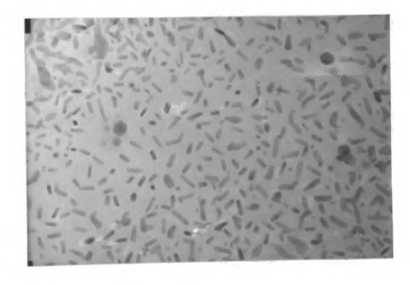


Figure 3-18. Electron micrograph of Te. (mag=140.000X. 700 Å/cm)

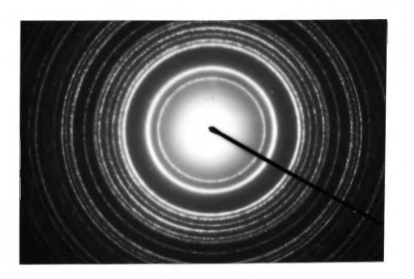


Figure 3-19. Selected area electron diffraction of Te.
(camera length = 140cm)

Table 3-3. Electron diffraction of Te from reduction of TeBr4.

	D(cm)a	d(Å)b	d/d'c	d'(Å)d	hkle
1	2.74	3.781	0.979	3.86	100
2	3.29	3.149	0.975	3.23	101
3	4.53	2.287	0.973	2.35	102
4	4.76	2.176	0.976	2.23	110
5	5.12	2.023	0.968	2.09	111
6	5.41	1.915	0.967	1.98	003
7	5.79	1.789	0.975	1.83	201
8	6.06	1.710	0.973	1.76	103
9	6.59	1.572	0.973	1.616	202
10	7.24	1.431	0.967	1.479	113

- a. Ring diameter of electron diffraction.(camera length= 140cm)
- b. d-spacing converted from ring diameter.
- c. d-ratio from electron and powder X-ray diffraction.
- d. d-spacing from powder X-ray diffraction files.(4-0554)
- e. Miller index.

#### (IV). Nickel

By adding triethylphosphine to increase the solubility. NiBr<sub>2</sub> was reduced by  $K^+(15C5)_2K^-$  in dimethyl ether. The products were kept in the H-cell under vacuum for four days and analyzed by XPS. Figure 3-20-A shows only metallic Ni peaks. Small NiO peaks appear when these particles were oxidized in air for 24 h. but all Ni particles were oxidized after washing by methanol as shown in Figure 3-20-B and 3-20-C.

## (V). Antimony

SbCl<sub>5</sub> was reduced by  $K^+(15C5)_2K^-$  in dimethyl ether. Both metallic and oxide  $3d_{5/2}$  and  $3d_{3/2}$  XPS peaks appear in Figure 3-21-A and 3-21-B before and after washing by methanol. The washed products were sputtered by Ar ions for 20 min. The result shown in Figure 3-21-C indicates that only a small amount of oxide was left after sputtering.

#### (VI) Gallium

GaC13 was reduced by  $K^+(15C5)_2K^-$  in dimethyl ether. Both metallic and oxide L3M45M45 Auger peaks appear in Figure 3-22-A. The sample was bombarded by argon ions for 2 min and 5 min as shown in Figure 3-22-B and 3-22-C respectedly. It is clear that the longer the argon ion sputtering the higher the intensity of the metallic peak and the lower the intensity of the oxide peaks.

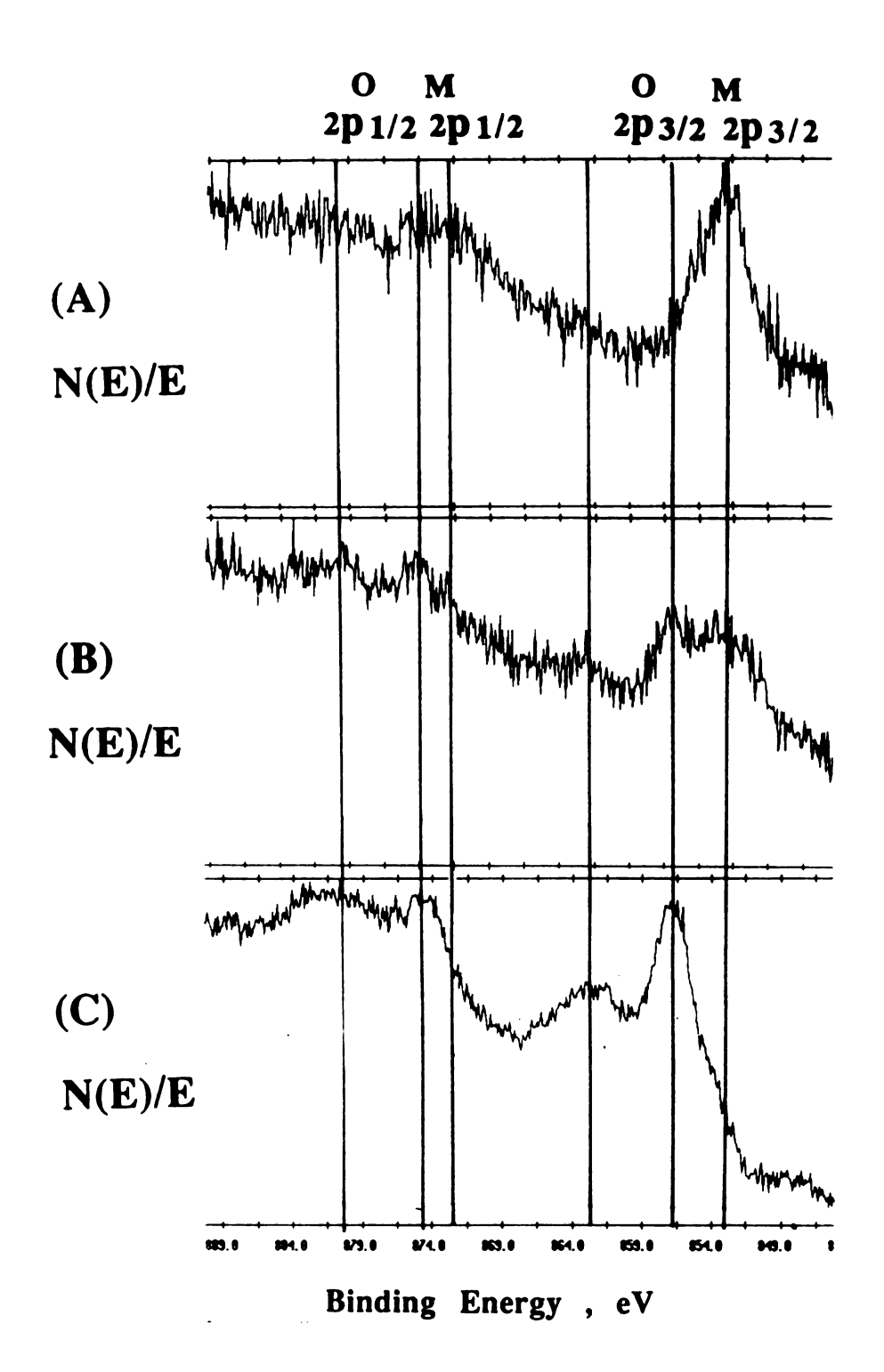


Figure 3-20. XPS spectrum of Ni.(A) before washing (B) oxidised in the air for 24 h (C) washed by MeOH

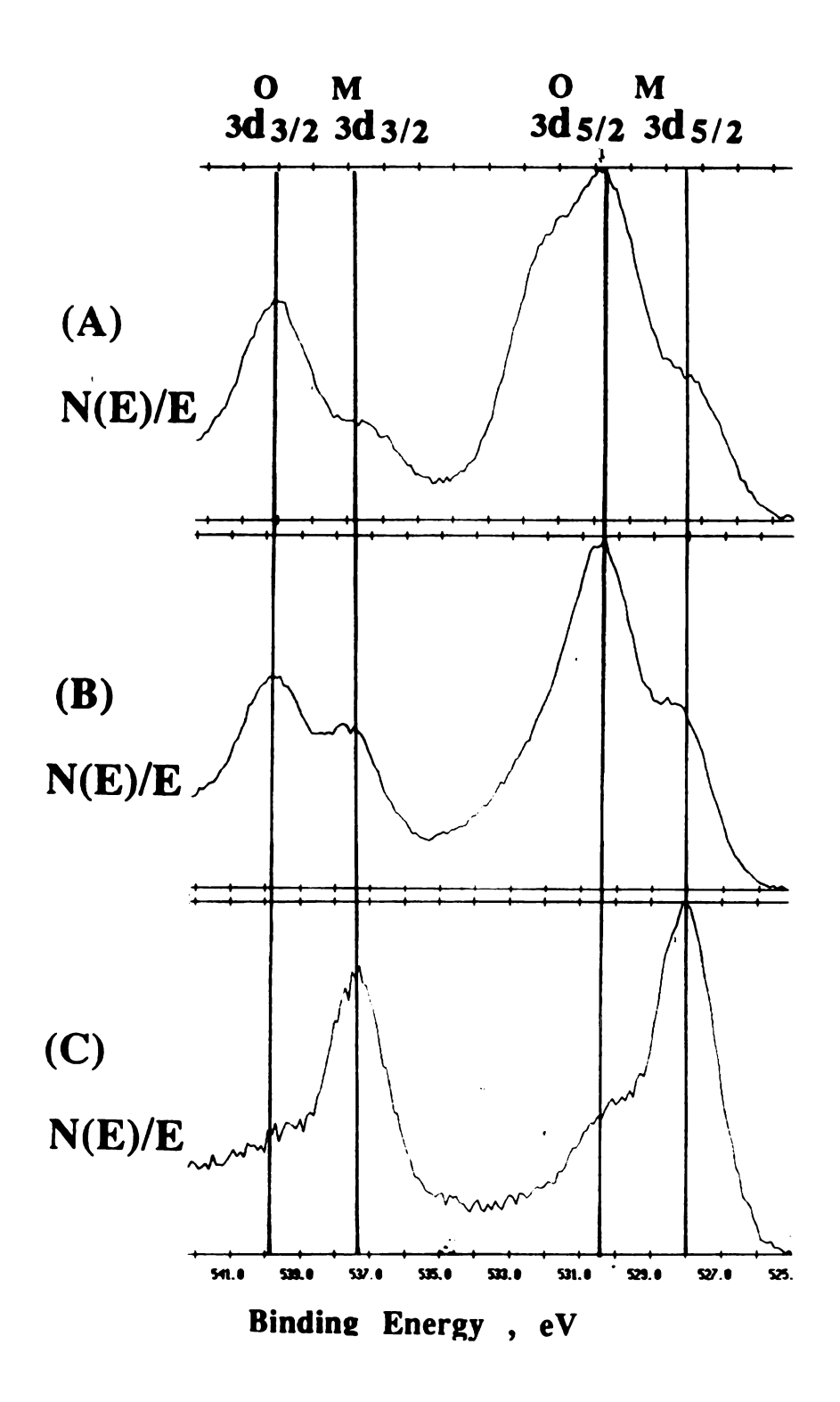


Figure 3-21. XPS specrum of Sb. (A) before washing (B) washed by MeOH (C) sputtered by Ar ions

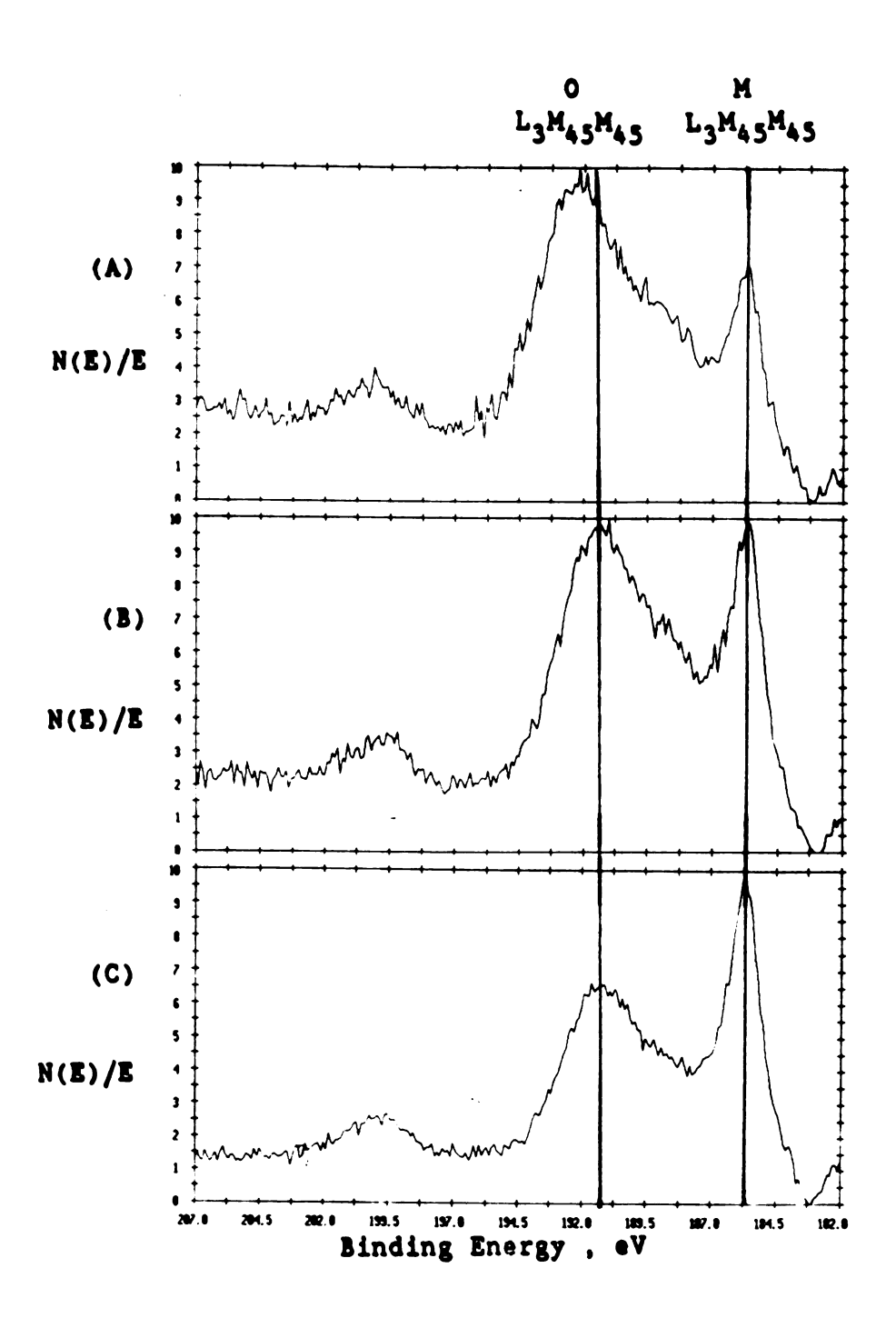


Figure 3-22. XPS specrum of L3M45M45 Auger peaks of Ga. (A) reaction products (B) sputtered by Ar ions for 2 min (C) sputtered by Ar ions for 5 min

#### (VII) Zinc

Znl2 was reduced by  $K^+(15C5)_2K^-$  in dimethyl ether. Both metallic and oxide L3M45M45 Auger peaks appear in Figure 3-23-A. The sample was bombarded by argon ions for 2 min and 4 min as shown in Figure 3-23-B and 3-23-C respectedly.

## (VIII) Molybdenum

MoC15 was reduced by  $K^+(15C5)_2K^-$  in dimethyl ether. Both metallic and oxide  $3d_{5/2}$  and  $3d_{3/2}$  XPS peaks appear in Figure 3-24-A. The sample was bombarded by argon ions for 10 min and 30 min as shown in Figure 3-24-B and 3-24-C respectedly. The oxide on molybdenum is harder to remove than that on zinc or gallium so that it took a longer time to sputter off the oxide.

### (IX) Tin

SnCl<sub>4</sub> was reduced by  $K^+(15C5)_2K^-$  in dimethyl ether. Both metallic and oxide  $3d_{5/2}$  and  $3d_{3/2}$  XPS peaks appear in Figure 3-25-A. The sample was exposed to the air for 30 seconds and the intensity of metallic peaks was decreased to only about half as shown in Figure 3-25-B.

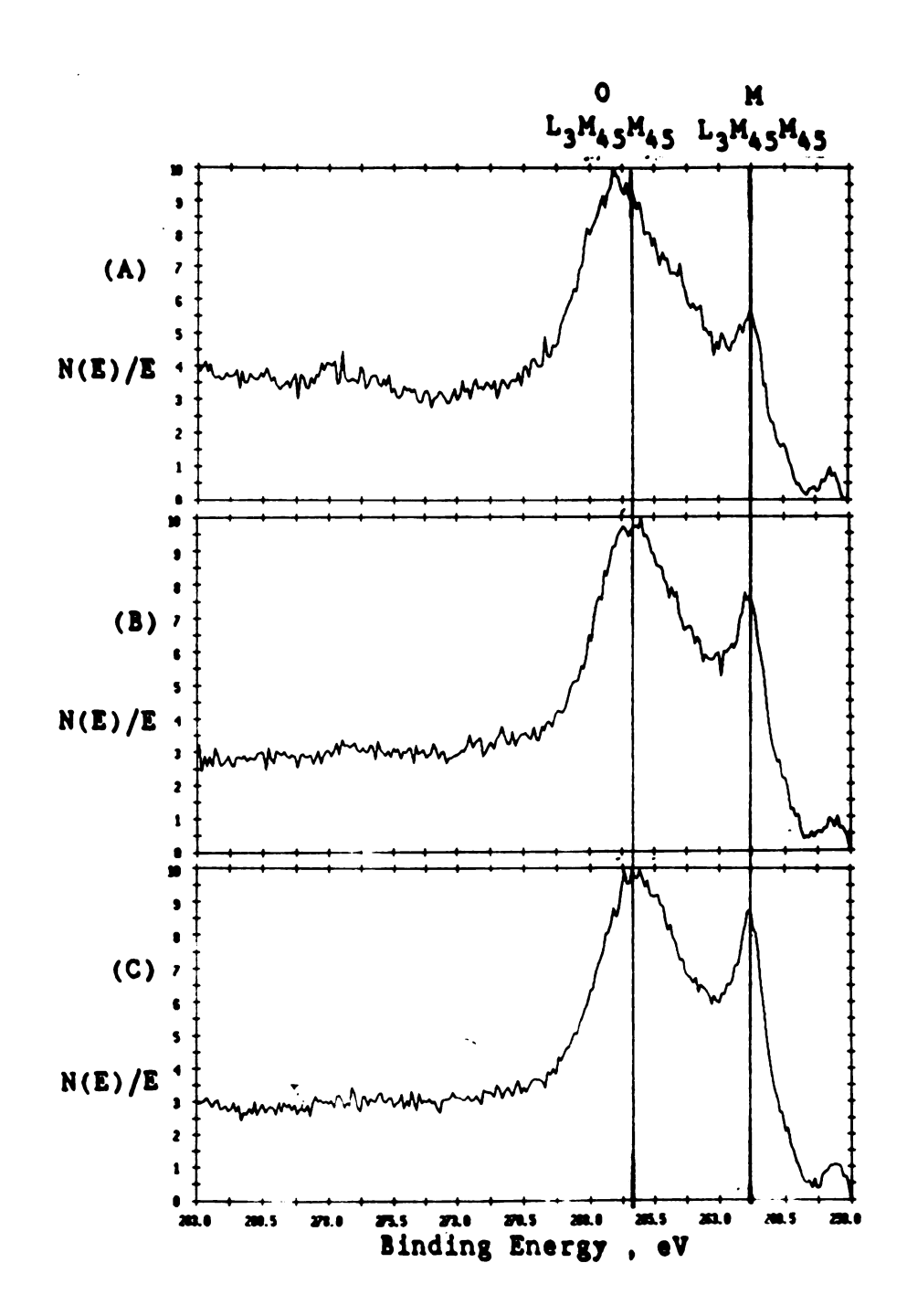


Figure 3-23. XPS specrum of L3M45M45 Auger peaks of Zn. (A) reaction products (B) sputtered by Ar ions for 2 min (C) sputtered by Ar ions for 4 min

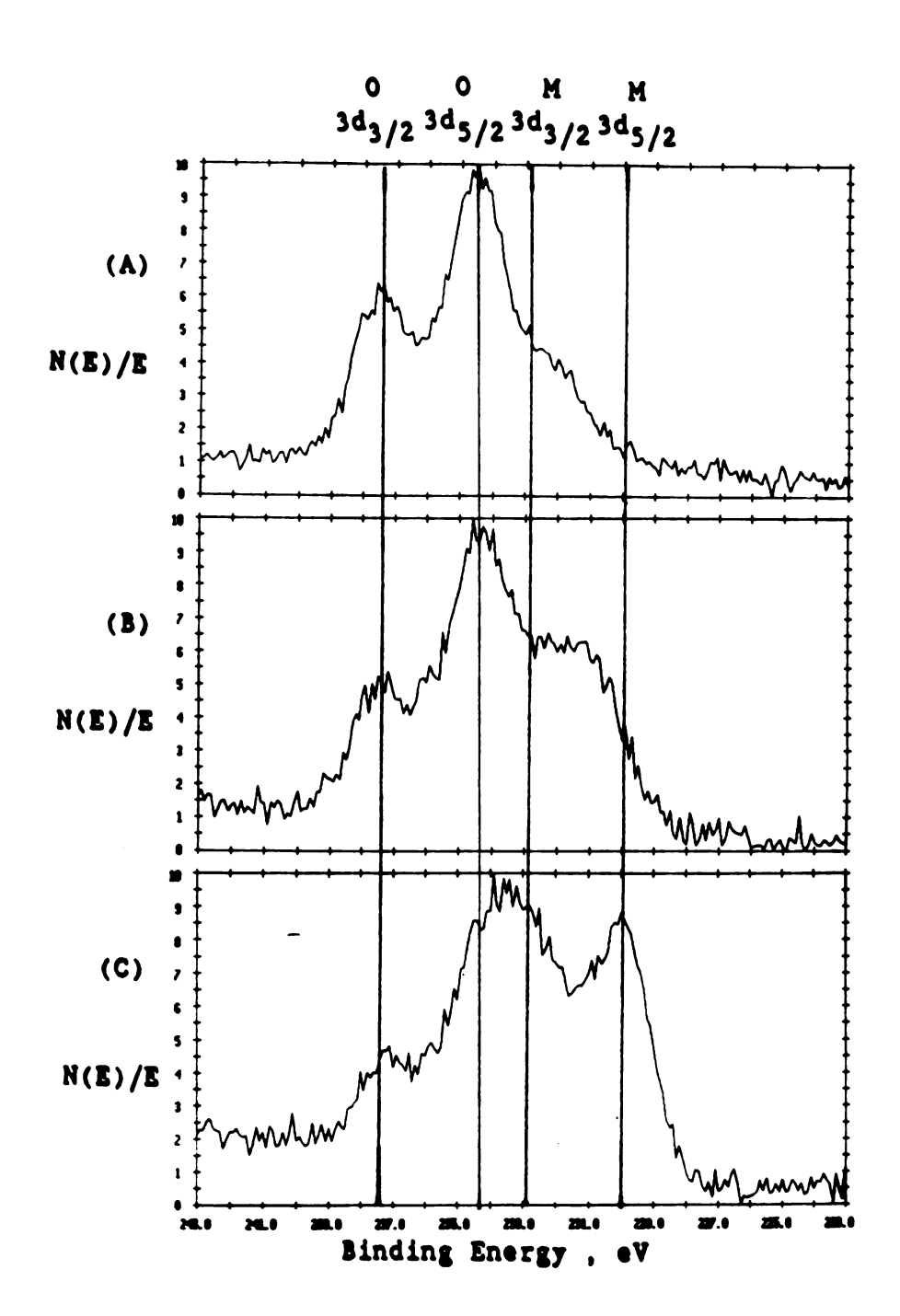


Figure 3-24. XPS specrum of 3d peaks of Mo. (A) reaction products

(B) sputtered by Ar ions for 10 min (C) sputtered by Ar ions for 30 min

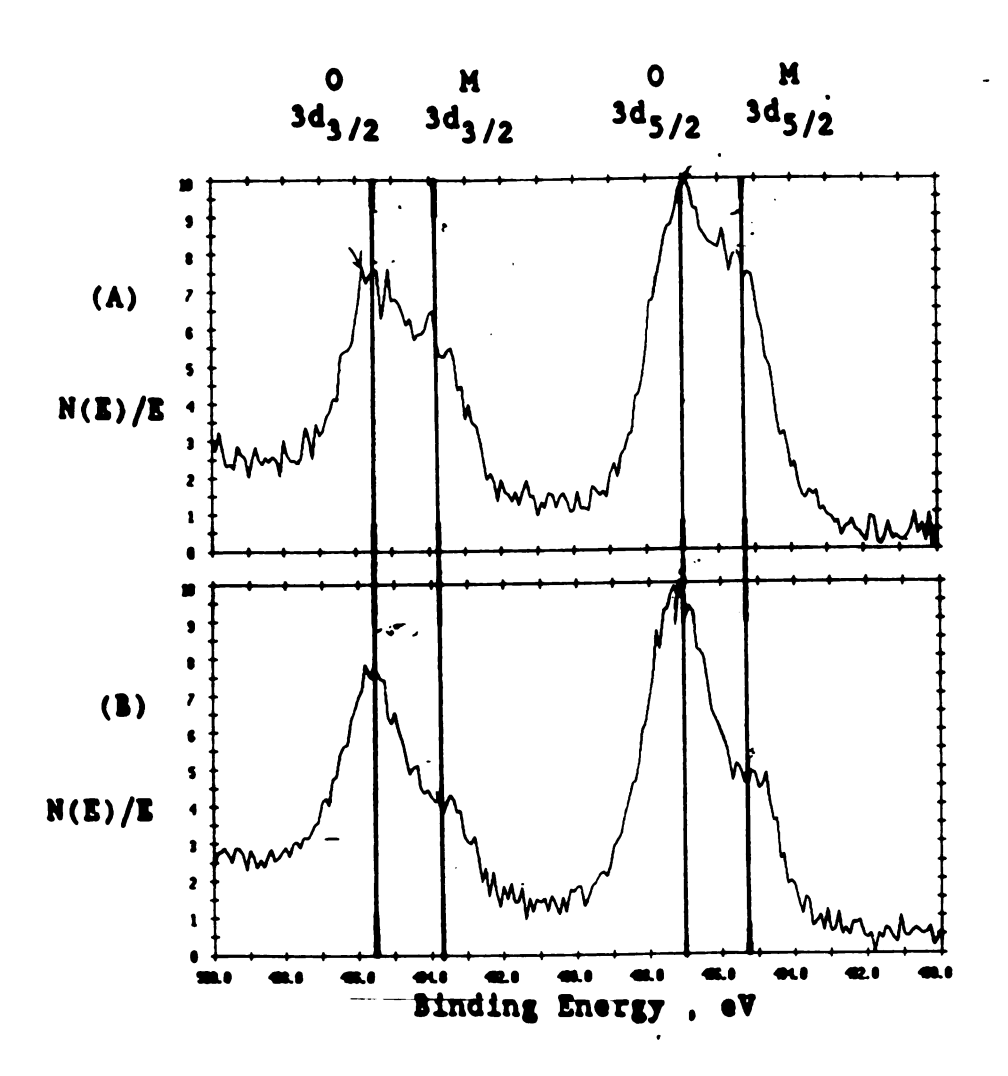


Figure 3-25. XPS specrum of 3d peaks of Sn. (A) reaction products (B) exposed to the air for 30 seconds

#### D. Summary

The reduction products are indicated in Table 3-4 and may be classified as follows.

- (1) Washable metals: Metal particles could be washed with little or no surface oxidation. Compounds reduced include  $AuCl_3$ .  $H_2PtCl_6$  (hydrated).  $TeBr_4$ . and  $CuCl_2$ .
- (2) Surface-oxidized: Partial or complete surface oxidation occurs with or without washing, but the subsurface material is metallic. Compounds include SbCl<sub>5</sub>, Znl<sub>2</sub>, GaCl<sub>3</sub>, SnCl<sub>4</sub>, InCl<sub>3</sub>, and SiCl<sub>4</sub>.
- (3) Nonwashable: Metal was observed with the unwashed product only. Oxidation occurs upon washing with methanol. Included are NiBr<sub>2</sub> + triethylphosphine. MoCl<sub>5</sub>. FeCl<sub>3</sub>, and WCl<sub>6</sub>.
- (4) Reoxidized: No metal was observed (with or without washing), although initial reduction occurs as indicated by fading of the blue color of the alkalide solution. This includes only  $TiCl_4$  so far. although  $TaCl_5$  is also readily oxidized by the reaction medium.

Homogeneous reduction of various metal salts with alkalides or electrides in Me<sub>2</sub>O or THF at -50 °C or below produces 2-15 nm diameter particles of metals or oxidized products. Reactions are rapid. complete, and applicable to a wide range of elements from Ti to Te. Metallic particles dispersed on high surface area oxides were also prepared in this way.

The XRD patterns of the unwashed products and the absence of significant carbon signals in the XPS data of washed samples show

that most of the crown ether complexant is not destroyed in the process and could be recovered if desired. This would be important in the utilization of the method because of the relatively high cost of the complexants.

VI VI	0	S	8	$\left  \begin{array}{c} \mathrm{Te} \\ 1 \end{array} \right $	8
<b>&gt;</b> <	Z	Ь	As	Sb 2	Bi
¥	C	Si 2	3	Sn 2	Pb
H	В	VI	Ga 2	In 2	П
		II B	Zn 2	Cd 2	Нg
		ВП	Cu 1	Ag	Au 1
			Ni 3	Pd	Pt 1
		N N	ပ	Rh	Ir
			Fe 1	Ru	Š
		VII B	Mn	Тс	Re
		MI B	Cr	Mo 3	W 3
		<b>P</b>	Λ	NP	Ta 1
		B≤	Ti 4	Zr	H
		IIII B	ઝ	Y	La

Identification: 1, washable metals; 2, surface-oxidized; 3, nonwashable; Part of the periodic table showing the elements studied to date. 4, reoxidized. See the text for more detailed definition. Table 3-4.

## Chapter 4 BINARY ELEMENT REDUCTION

#### A. Introduction

Single element reduction was described in Chapter 3. Soluble compounds of transition metals and post-transition metals in dimethyl ether or tetrahydrofuran are rapidly reduced at - 50 °C by dissolved alkalides or electrides to produce metal particles with crystallite sizes from < 3 to 15 nm. It is clear that a wide variety of elements can be prepared as small metallic particles by reducing dissolved compounds in Me<sub>2</sub>O or THF with M<sup>-</sup> or e<sup>-</sup>solv.

Because of the small particle size (and probably even smaller initial particles) it was of interest to examine the products of reduction of homogeneous mixtures of two or more metal salts. If intermetallic compounds could be formed rather than mixtures of metals, this would open up an opportunity to synthesize new materials, since many intermetallic compounds that are stable at low temperatures decompose at high temperatures. A major advantage of the present method is the ability to control overall stoichiometry simply by adjusting initial compositions.

## B. Experimental

The purified aprotic solvents Me<sub>2</sub>O or THF were distilled from stainless (Me<sub>2</sub>O) or glass (THF) storage vessels, from which 30-40 mL

were withdrawn by distillation as needed. The commercially available H-cell (Figure 2-1) was used to carry out the reduction. The solid or liquid samples of the compounds to be reduced were added to one arm and either a pre-synthesized sample of the alkalide or electride or the alkali metal and a stoichiometric amount of complexant was added to the other arm in the He-filled dry box.

Small amounts (5-10 mg) of reactants were used to produce  $10^{-2}$  to  $10^{-4}$  M. solutions. Larger amounts up to a millimole were used when the precursor solubility permitted. The potasside,  $K^+(15C5)_2K^-$ , and electride,  $K^+(15C5)_2e^-$ , were used as the reductants because of their high solubilities and ease of preparation. To carry out homogeneous reactions, the desired compound and the alkalide or electride were separately dissolved in Me<sub>2</sub>O or THF and the solutions were rapidly mixed. Reduction was immediate to give colloidal solutions when dilute and precipitates when concentrated.

#### C. Results

When two different metal salts were used, alloys or intermetallic compounds formed as indicated by XPS. Confirmation by electron diffraction was made in the case of air-stable samples. All binary systems studied so far yielded some evidence for alloy or compound formation. But all have been X-ray amorphous, thus preventing identification of the compounds by XRD.

The photoelectron and Auger peaks were used to distinguish intermetallic compounds from a mixture of the pure metals, but cannot provide positive identification. When the sample can be

briefly exposed to air without oxidation. it is possible to use electron microscopy. EDS and, especially SAD to identify compounds.

## (I) Au-Zn

The identification of the known compound AuZn was carried out by XPS and SAD. Figure 4-1 (A) is the XPS spectrum of Au  $4f_{7/2}$  and  $4f_{5/2}$  from the product of reduction of AuCl<sub>3</sub>. The binding energy of Au  $4f_{7/2}$  at 83.70 eV and  $4f_{5/2}$  at 87.30 eV shows that the product is pure metallic gold.(50) Figure 4-1(B) is the Au  $4f_{7/2}$  and  $4f_{5/2}$  XPS spectrum from the product of reduction of a mixture of AuCl<sub>3</sub> and Znl<sub>2</sub> that contains excess Znl<sub>2</sub>. These peaks shift to 84.45 eV and 88.00 eV respectively.

The 4f binding energy splitting (3.55 eV) from (B) is narrower than that (3.60 eV) from (A). and shifted to higher binding energy with respect to the Fermi level. This indicates that an alloy is formed from the reduction of the mixtures. This result is in good agreement with the XPS work on Al-Au alloys by Fuggle and coworkers.(51) Figure 4-1(C) is the spectrum from the mixtures of AuCl<sub>3</sub> and Znl<sub>2</sub> with excess AuCl<sub>3</sub>. This spectrum shows clearly that both pure metallic gold and alloy exist. The new compound was identified as AuZn by SAD. Table 4-1 is the comparison of d-spacings between XRD and SAD.

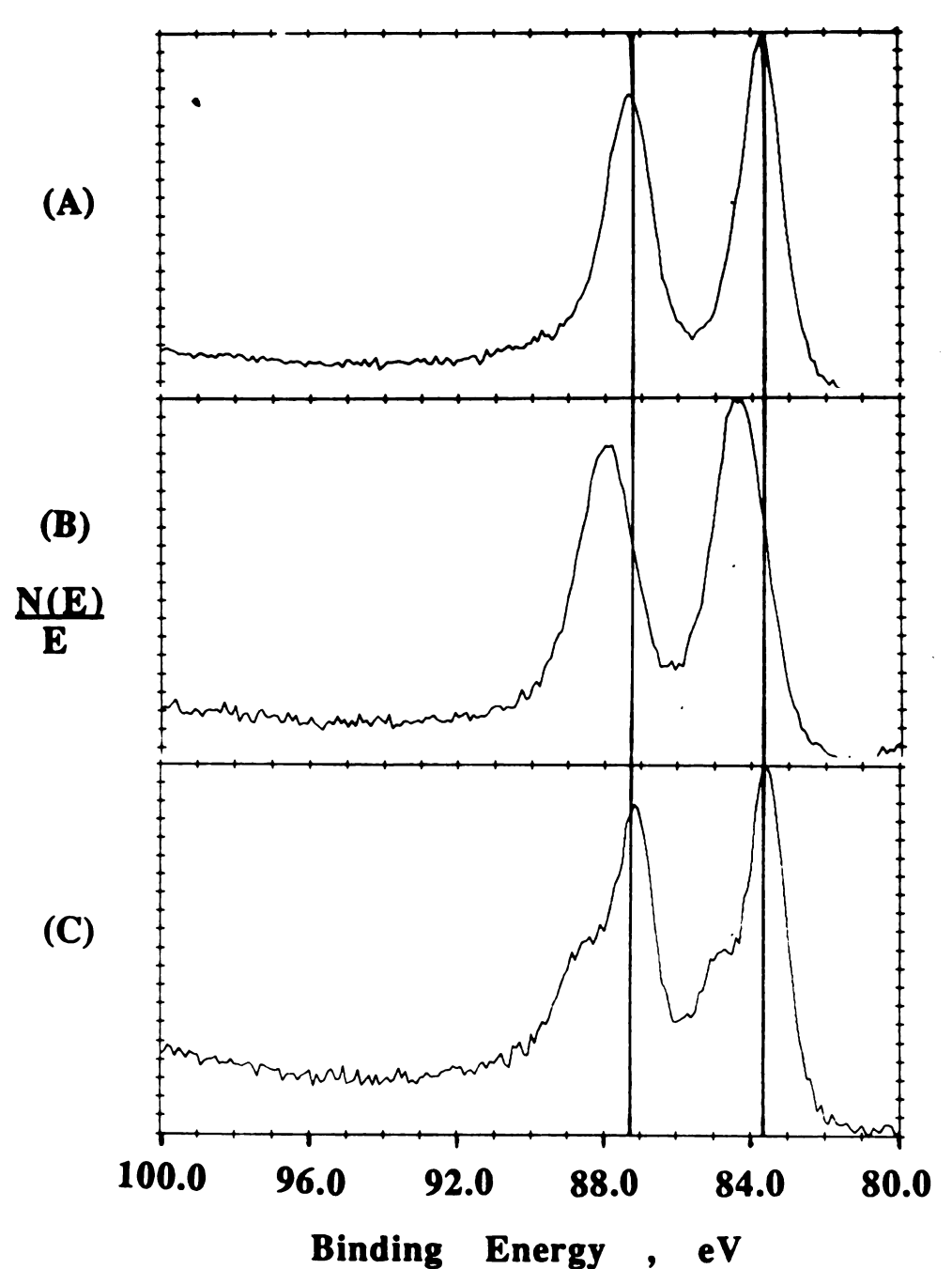


Figure 4-1. XPS spectrum for the 4f5/2 and 4f7/2 levels of Au:(A)

Au particles from AuCl3 reduction: (B) AuZn particles
formed from reduction of a mixture of AuCl3 and
excess Znl2: (C) AuZn + Au particles formed from
reduction of a mixture of AuCl3 and Znl2 with the former
in excess.

Table 4-1. Electron diffraction of AuZn from co-reduction of AuCl<sub>3</sub>+Znl<sub>2</sub>.

	D(cm)a	d(Å)b	d'(Å)¢	AuZn(Å)d	hkle
1	3.31	3.13	3.19	3.1960	100
2	4.63	2.24	2.28	2.2599	110
3	5.73	1.81	1.85	1.8452	111
4	6.58	1.57	1.60	1.5980	200
5	7.40	1.40	1.43	1.4293	210
6	8.14	1.27	1.30	1.3048	211

- a. Ring diameter of electron diffraction. (camera length = 140cm)
- b. d-spacing converted from ring diameter.
- c. d-spacing corrected by camera constant.
- d. d-spacing from powder X-ray diffraction files.(30-608)
- e. Miller index.

#### (II) Au-Cu

The Au-Cu alloy is the most studied of all alloys except Fe-C. It has been found that the structure at its ideal composition. AuCu, consists of alternate layers of Au and Cu atoms parallel to a cube face. The symmetry is slightly distorted to tetragonal with c/a=0.93. The structure transforms to orthorhombic with b/a=10.03 at about 380 °C.(52) We prepared a new phase of this compound with a cubic structure as identified by the SAD pattern by reduction of stoichiometric mixtures of AuCl<sub>3</sub> and CuCl<sub>2</sub> at -50 °C.

Formation of a compound in the Au-Cu system was suggested but not proven by the XPS data. The Au  $4f_{7/2}$  and  $4f_{5/2}$  XPS lines are near those of pure Au. and the Cu  $2p_{3/2}$  XPS line at 932.3 eV is close to that of Cu (932.4 eV) and Cu<sub>2</sub>O (932.2 eV). However, the modified Auger parameter,  $\alpha$ , which is free of charging errors, is 1849.9 eV, about 1.6 eV below those of copper metal and CuO but close to the value for Cu<sub>2</sub>O (1849.5 eV). Thus, the photoelectron and Auger data are not definitive in this case. The SAD results are. however, clear and unambiguous. The diffraction pattern is of the same type as that of AuZn and corresponds to a simple cubic structure with each Au atom at the center of a cube of Cu atoms and vice versa. The patterns of the two known higher temperature phases of AuCu (tetragonal and orthorhombic) would be very different from that observed. The cubic unit cell has a=2.95 Å compared with 3.196 Å for AuZn. The d-spacings are listed in Table 4-2.

Table 4-2. Electron diffraction of AuCu from co-reduction of AuCl<sub>3</sub>+CuCl<sub>2</sub>.

	D(cm)a	d(Å)b	d'(Å)¢	hkid
1	3.60	2.88	2.94	100
2	5.12	2.02	2.06	110
3	6.26	1.66	1.69	111
4	7.27	1.43	1.46	200
5	8.12	1.28	1.31	210
6	8.95	1.16	1.18	211

- a. Ring diameter of electron diffraction. (camera length = 140cm)
- b. d-spacing converted from ring diameter.
- c. d-spacing corrected by camera constant.
- d. Miller index.

#### (III) Tellurides

When particles of Au, Cu or Te were separately prepared by reduction of AuCl<sub>3</sub>. CuCl<sub>2</sub> and TeBr<sub>4</sub> respectively, the XRD pattern always showed peaks of the metal. Reduction of a mixture, however, gave X-ray amorphous products except when an excess of one component was used. This suggests the formation of alloys or compounds with either random occupancies or crystallite sizes smaller than 3 nm.

The reduction of a mixture of  $CuCl_2$  and  $TeBr_4$  in  $Me_2O$  yielded a powder that was washed with air-free methanol without significant oxidation. The  $Cu\ 2p_{3/2}$  and  $2p_{1/2}$  binding energies from the XPS of the product. 932.5 and 952.3 eV respectively, are indistinguishable from those of metallic copper, and the  $L_3VV$  Auger peak is at nearly the same energy as for pure Cu. The modified Auger parameter,  $\alpha$ '. 1850.5 eV. is slightly lower than the average literature value of 1851.5 eV. Thus, the XPS data for the binary system Cu-Te do not distinguish between compound formation and mixture of the pure metals. They do show, however, that the original compounds were reduced.

The case for compound formation in the Au-Te system is somewhat stronger. The Au  $4f_{7/2}$  and  $4f_{5/2}$  XPS peaks in the binary system are nearly twice as wide as for pure Au, although the peaks positions are essentially the same as those of the pure metal. Also the value of  $\alpha$ ' for Te in the mixture (1064.5 eV) is at least 0.4 eV lower than that of elemental tellurium.

On the basis of the XRD results and the XPS data, it is concluded that alloy or compound formation occurs in the Au-Te system and probably also in the Cu-Te system.

#### (IV) Ti-Au

The reduction of a mixture of TiCl4 and AuCl3 yielded the XPS results shown in Figure 4-2. The unwashed product (top curve) gave broadened Au  $4f_{7/2}$  and  $4f_{5/2}$  XPS peaks at the positions observed with pure gold. (83.7 and 87.4 eV) and shoulders at 84.8 and 88.4 eV. Upon washing with methanol, the XPS pattern (bottom curve) reverted to that of pure Au. The possible formation of a Ti-Au compound is suggested by these results, but further work needs to be done to verify this conclusion. The results could be significant for catalysis if it were possible to produce small noble metal particles on a finely divided TiO<sub>2</sub> or Ti(OR)<sub>2</sub> support.

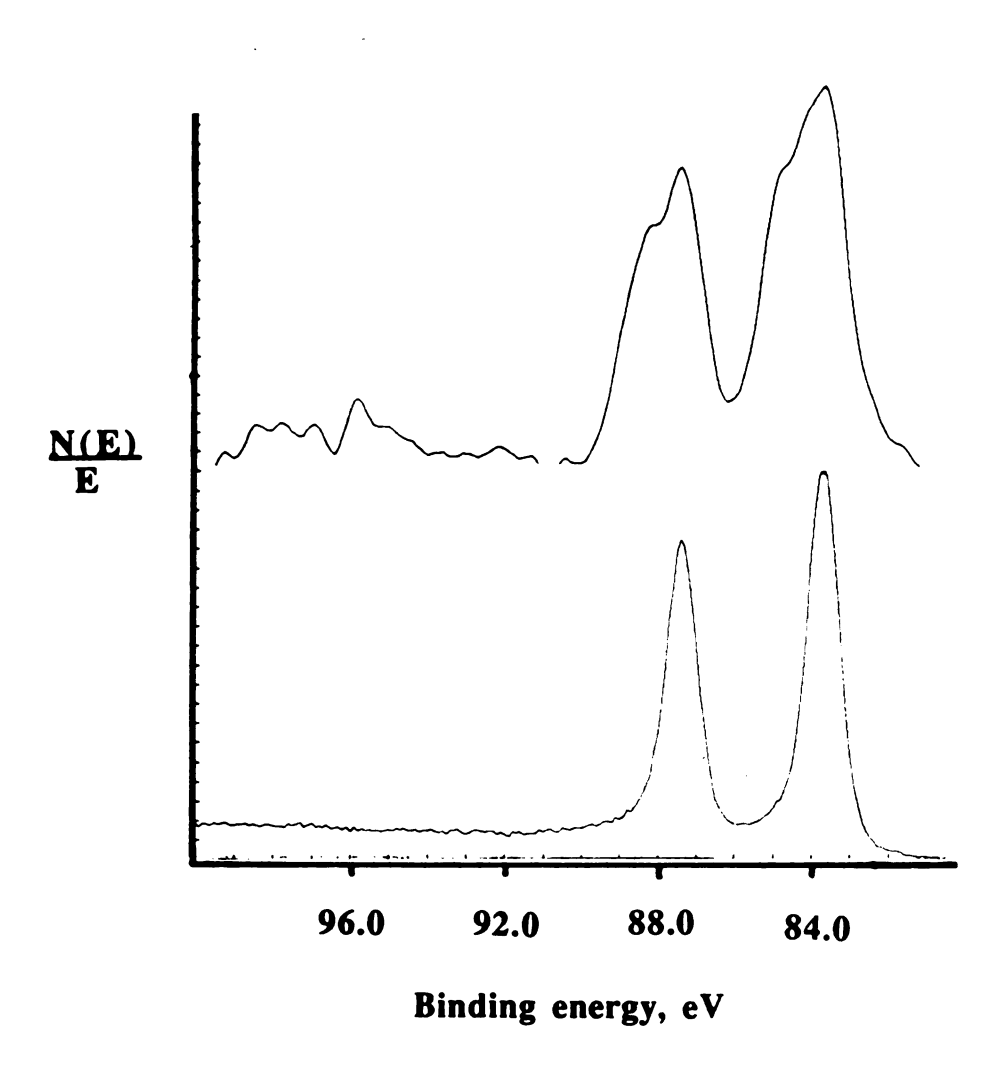


Figure 4-2. XPS of the reduction product of a mixture of TiCl4 and AuCl3 in Me<sub>2</sub>O (top) and after washing with air-free methanol (bottom).

(V) Ta-Fe

Refractory and oxophilic metals, such as Ta. W and Mo present severe challenges to preparation by this method. They require strong reductants, have multiple oxidation states and have such a high affinity for oxygen that small particles are expected to be very reactive. The "intertness" of the bulk metals is due to a compact oxide layer rather than to an inherent lack of reactivity. In spite of these difficulties, our initial results showed that Mo and W metals could be produced by reduction of MoCl<sub>5</sub> and WCl<sub>6</sub> respectively, but, as expected, washing with methanol resulted in complete oxidation.

Considerable effort has been expended in an attempt to prepare millimole quantities of small tantalum particles for use as precursors in ternary nitride synthesis. Purified TaCl<sub>5</sub> is very soluble in Me<sub>2</sub>O and reacts immediately in an H-cell with K<sup>+</sup>(15C<sub>5</sub>)<sub>2</sub>K<sup>-</sup> prepare in situ. Since five moles each of K and 15C<sub>5</sub> are required per mole of TaCl<sub>5</sub>, copious amounts of KCl and K<sup>+</sup>(15C<sub>5</sub>)<sub>2</sub>Cl<sup>-</sup> are produced and are only slightly soluble in Me<sub>2</sub>O. Most, but not all, of the byproducts can be removed by washing with anhydrous liquid ammonia. The product is Ta metal together with some unidentified organic material. The fine black powder is pyrophoric and reacts immediately with water and methanol. It can, however, be handled and stored in an inert atmosphere box without apparent change. The XRD pattern shows the product to be amorphous, but the XPS peaks (Figure 4-3-D) provide identification as Ta metal.

Pyrophoric iron can be readily prepared by reduction of FeCl<sub>3</sub> in Me<sub>2</sub>O. When solid FeCl<sub>3</sub> was present in contact with the saturated solution during reduction with an excess of  $K^+(15C5)_2K^-$ , crystalline

Fe was produced as indicated by the XRD pattern. The by-products could be removed by washing with liquid ammonia. More dilute solutions yielded X-ray amorphous iron. The XPS peaks (Figure 4-3-B) show the presence of both metallic iron and oxidized iron on the surface of the particles.

In an attempt to prepare the known compound Fe<sub>2</sub>Ta, mixtures of FeCl<sub>3</sub> and TaCl<sub>5</sub> in a 2:1 mole ratio were reduced with K<sup>+</sup>(15C5)<sub>2</sub>K<sup>-</sup> in Me<sub>2</sub>O and the product was washed with NH<sub>3</sub>. The product has not yet been identified, but the XPS data show the presence of Ta, Fe and K in approximately a 1:2:3 mole ratio. The Fe and Ta XPS patterns are shown in Figures 4-3-A and 4-3-C respectively. The latter shows a shift of the Ta  $4f_{7/2}$  peak from 21.6 eV in Ta metal to 23.8 eV. Oxidation of the mixture in air shifts the peak to 24.8 eV. The Fe  $2p_{3/2}$  peak at 706.3 eV (Fe metal = 706.8 eV) shifts to 709.7 eV upon oxidation (Fe<sub>2</sub>O<sub>3</sub> = 711 eV). The K  $2p_{3/2}$  peak at 292.6 eV does not shift upon oxidation. A substantial carbon 1s peak at 285.0 eV decreases dramatically upon argon ion sputtering. The results show that some type of complex alloy or compound formation occurs in the K-Ta-Fe system, but the product or products have not been identified.

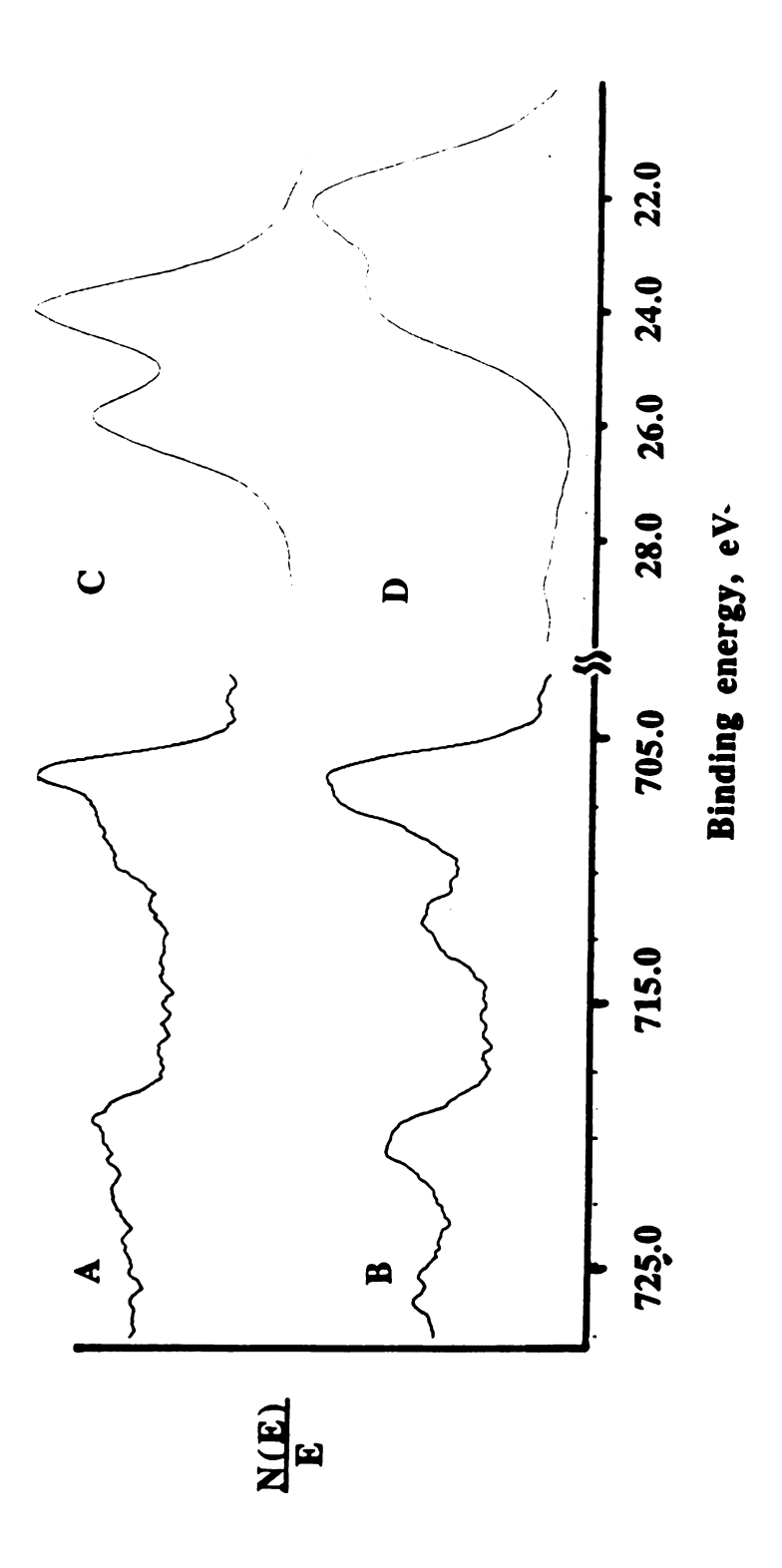


Figure 4-3 XPS results for the Ta-Fe system; product washed with anhydrous NH3: (A) Fe XPS from 2:1 FeCl3 to TaCl5; (B) Fe XPS from FeCl3 alone; (C) Ta XPS from 2:1 FeCl3 to TaCl5; (D) Ta XPS from TaCl5 alone.

## C. Summary

In spite of the preliminary nature of these experiments, it is clear that reduction of pure compounds in Me<sub>2</sub>O or THF solutions with dissolved alkalides and electrides leads to nanoscale metal particles. The strong reducing ability of alkalides and electrides makes the method very general and permits metal production across the transition metal and post-transition metal series, from Ta to Te. It is difficult to positively identify alloys and compounds with particle sizes too small to yield an X-ray diffraction pattern and with reactivities too high to load into available TEM without oxidation. While the less reactive compounds AuCu and AuZn could be characterized, a number of other binary systems yielded powdered samples whose XPS pattern suggested alloy or compound formation, but did not provide identification. This method is also applicable to the formation of finely divided metals on oxide supports and to the synthesis of organometallic compounds.

# Chapter 5 REDUCTION in ZEOLITE PORES

#### A. Introduction

In recent years there have been considerable academic and industrial research efforts carried out in the field of zeolite catalysis. There are 34 known natural zeolites and about 100 zeolites which do not have natural counterparts have been synthesized. Of this large number of zeolites, only a few have found commercial application: they are mostly synthetic zeolites and synthetic-analog natural zeolites. A zeolite has been defined as a "crystalline aluminosilicate with a tetrahedral framework structure enclosing cavities occupied by cations and water molecules, both of which have enough freedom of movement to permit cation exchange and reversible dehydration".

The major part of zeolite catalysis work has been related to reactions where the zeolite is used as solid acid. e.g., isomerization, cracking, hydrocracking etc. The catalyst of choice for catalytic cracking, the heaviest use of zeolites, is usually a rare earth, magnesium, hydrogen, or ultrastable form of zeolite X and Y, or a combination of these.

In general, zeolites have four properties that make them especially interesting for heterogeneous catalysis:(53)

- 1. They have exchangeable cations allowing the introduction of cations with various catalytic properties.
- 2. If these cationic sites are exchanged with H<sup>+</sup>, they can have a very high number of very strong acid sites.

- 3. Their pore diameters are less than 10 Å.
- 4. They have pores with one or more discrete sizes.

The properties of a zeolite are dependent on the topology of its framework, the size, shape, and accessibility of its free channels, the location, charge and size of the cations within the framework, and the presence of faults and/or occluded material. Therefore, structural information is extremely important in understanding the adsorptive and catalytic properties of zeolite catalysts.

The fundamental building block of all zeolites is a tetrahedron of four oxygen anions surrounding a small silicon or aluminum ion. These tetrahedra are arranged so that each of the four oxygen anions is shared in turn with another silica or alumina tetrahedron. The crystal lattice extends in three-dimension and the -2 oxidation state of each oxygen is accounted for. Each silicon ion has its +4 charge balanced by the four tetrahedral oxygens and the silica tetrahedra are electrically neutral. Each alumina tetrahedron has a residual charge of -1 since the trivalent aluminum is bonded to four oxygen anions. Thus each alumina tetrahedron requires a +1 charge from a cation in the structure to maintain electrical neutrality.

The silica and alumina tetrahedra are combined into more complicated secondary units, which form the building blocks of the framework zeolite crystal structures. The silica and alumina tetrahedra are geometrically arranged, with Al-O-Al bonds excluded. The unit cell formula is usually written as

 $M^{n+}_{X/n}[(A102^{-})_{X}(SiO_{2})_{Y}] zH_{2}O$ 

where M<sup>n+</sup> is the cation which balances the negative charge associated with the framework aluminum ions. These metal cations, which neutralize the excess anionic charge on the aluminosilicate framework, are usually alkali metal and alkaline earth metal cations and at least some of them must be able to undergo reversible ion exchange. Water molecules fill the remaining volume in the interstices of the zeolite.

The tetrahedra are arranged so that the zeolites have an open framework structure, which defines a pore structure with a high surface area. The three-dimensional framework consists of channels and interconnected voids or cages. The cations and water molecules occupy the void spaces in the structure. The intracrystalline zeolite water can be removed by thermal treatment, usually reversibly.

Zeolite Y consists of tetrahedra linked to form so-called sodalite cage units as shown in Figure 5-1.

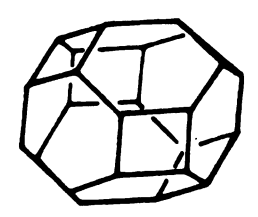


Figure 5-1 Structure of sodalite cage

A sodalite unit is the secondary building block of zeolite Y. Molecules can penetrate into this unit through the six-membered oxygen rings. which have a free diameter of 2.6 Å; the unit contains a spherical void volume with a 6.6 Å free diameter. Since the pore diameter is so small, only very small molecules, e.g. water, helium, or hydrogen cations can enter the sodalite cage.

When the truncated octahedra are connected by bridge oxygen atoms between the six-membered rings, zeolite Y is formed. Figure 5-2 shows the three-dimensional structure of zeolite Y. The unit cell of zeolite Y is cubic with a unit cell dimension of 25 Å, and it contains 192 silica and alumina tetrahedra. The unit cell dimension varies with Si/Al ratio. Each sodalite unit in the structure is connected to four other sodalite units by six bridge oxygen ions connecting the hexagonal faces of two units. The truncated octahedra are stacked like carbon atoms in diamond. This structure results in a supercage surrounded by ten sodalite units which is sufficiently large for an inscribed sphere with a diameter of 12 Å. The opening into this large cavity is bounded by sodalite units, resulting in a 12membered oxygen ring with a 7.4 Å free diameter. Each cavity is connected to four other cavities, which in turn are themselves connected to three-dimensional cavities to form a highly porous framework structure.

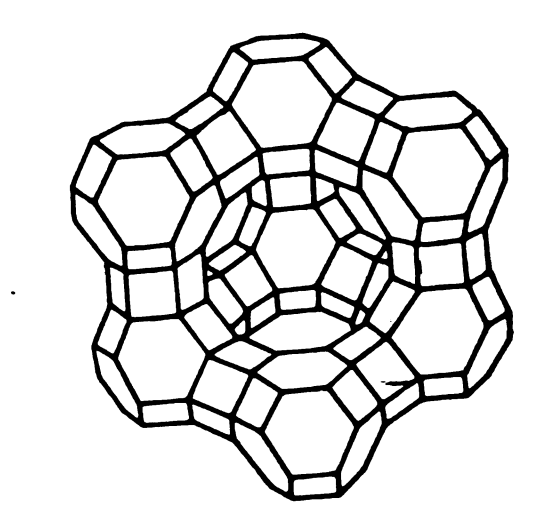


Figure 5-2 Structure of zeolite Y

Molecular sieve zeolites have played an important role in catalysis since the 1960's because of their selective adsorptive properties. (54) Their properties have been reviewed recently. (55) In order to locate and disperse metal particles in zeolite, researchers have studied zeolites intensively by X-ray diffraction, small angle X-ray scattering, chemisorption, electron microscopy. IR spectroscopy. X-ray photoelectron spectroscopy and Auger electron spectroscopy. The zeolite Y occurs naturally as the mineral faujasite and consists of a porous network of aluminate and silicate units tetrahedrally linked through bridging oxygen atoms. The structure consists of sodalite units arranged in a diamond net and linked through double sixrings. (56) These cavities provide an ideal environment for synthesizing single-size clusters.

The traditional way to synthesize supported metal zeolites is by impregnation or ion exchange followed by hydrogen reduction to give zero valent metal. In most cases, the final dispersion and location of the metal depend upon the pre-treatment under oxygen, which governs the cation positions, and the gaseous environment in which the sample is thermally treated before reduction. Homogeneous reduction of various metal salts with alkalides or electrides in dimethyl ether or tetrahydrofuran at - 50°C or below has produced 3-15 nm diameter particles of metals, alloys or oxidized products as described in Chapters 3 and 4. Here, the new reduction method that uses alkalides and electrides in zeolite pores will be discussed.

#### B. Experimental

One gram of NaY zeolite. Na56 (A102)56(SiO2)136xH2O. was ion exchanged by 100 mL of 0.1 N AgNO3. or Na2PdCl4. or CuCl2 in aqueous solutions for 3 days. and was washed by H2O. methanol. and dry ether several times to remove excess ions. followed by vacuum drying for 3 days at 120°C. AgY. PdNaY and CuNaY were produced respectively. About 200 milligrams of ion-exchanged zeolite and an excess of electride. K+(15C5)2e<sup>-</sup>. were added in a nitrogen-filled glove bag to different sides of an evacuated H-cell (Figure 2-1) with a medium frit. A liquid nitrogen bath was used to cool the cell to prevent decomposition of the electride. About 20 mL of pre-purified Me2O was distilled into both sides after evacuation to about 10<sup>-5</sup> torr while the cell was kept in a -50 °C isopropanol bath.

The blue-black solution of electride was poured through the frit to react with zeolite. Reaction occurred immediately upon addition of the electride as indicated by the fading of the blue color. A slight excess of electride was added until the blue color no longer disappeared to make sure that the reaction was complete. Then the solvent was distilled out under vacuum. Pre-purified water or methanol was used to wash away the by-products. The zeolite was removed from the H-cell and mounted on either indium foil or 3M Scotch double-coated tape in the He-filled dry box. A vacuum transfer vessel was used to carry the sample from the dry box to the XPS transfer chamber without exposing the sample to air.

The X-ray photoelectron spectra were obtained by using monochromatic Al K $\alpha$  X-rays. The Si 2p line at 102.8 eV was used as

an internal standard. The charging effect was reduced by flooding the sample with zero kinetic energy electrons of a neutralizer. X-ray diffraction patterns were recorded by packing the zeolite on a glass slide. A drop of zeolite suspension was put on the transmission electron microscope carbon coated grid and allowed to dry in the air.

#### C. Results

The XPS spectra of palladium in zeolites are shown in Figure 5-3. The reduction of palladium containing zeolite in dimethyl ether by electride at -50 °C leads to a shift of the 3d5/2 line position from 337.5 eV to 335.2 eV: this is the evidence for the reduction of palladium cations. This binding energy of palladium in zeolite is the same as that of a metallic palladium film.(57) However the value of the binding energy of the Pd 3d5/2 level in zeolite Y after hydrogen reduction is 336.1 eV as determined by Romannikov and coworkers.(58) Previous work had shown that atomically dispersed Pd in zeolite Y is at 336.4 eV while 20Å crystalline Pd is at 335.2 eV.(59)

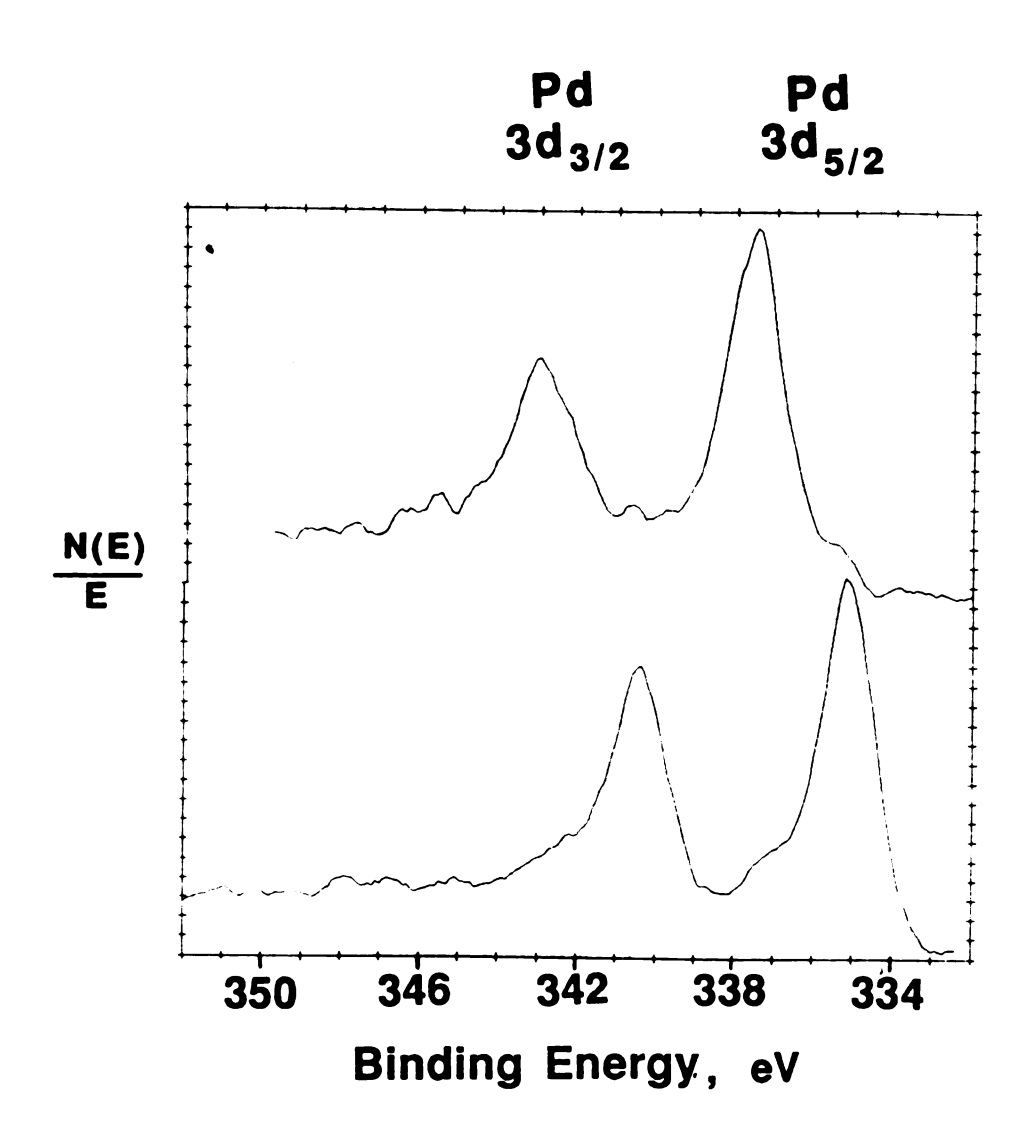


Figure 5-3. XPS spectra of Pd in zeolite Y before reduction 3d5/2=337.5 eV. 3d3/2=343.0 eV (top) and after reduction 3d5/2=335.2 eV. 3d3/2=340.4 eV (bottom).

We have calculated atomic ratios from the peak areas and the cross sections reported by Scofield. (60) These values were compared with the theoretical ratios obtained by assuming no surface enrichment. Surface enrichment of a particular element would normally appear as a large relative increase in the peak for that element since XPS only detects the top few layers of the zeolite particles. It is clear that the Pd 4f/Si 2p ratios did not change very much during reduction. Figure 5-4 shows the survey scans of (A) plain zeolite Y (B) after Na2PdCl4 ion exchange (new peaks of Pd 3d5/2 at 337 eV and 3d3/2 at 343 eV appear and the Na 1s peak at 1071 eV decreases) (C) after reduction by  $K^+(15C5)2e^-$ . (new peaks of K 2p appear showing potassium cations balance the counter charge)

Powder X-ray diffraction patterns were recorded to make sure that there was no structural change during reduction.(61) The peak corresponding to the (111) d-spacing of palladium was not observed for the sample. This indicates that the palladium particles are too small (< 30 Å) to be detected by powder X-ray diffraction. Transmission electron microscopic investigation also showed the absence of metallic particles on the external surface of the zeolite crystals.

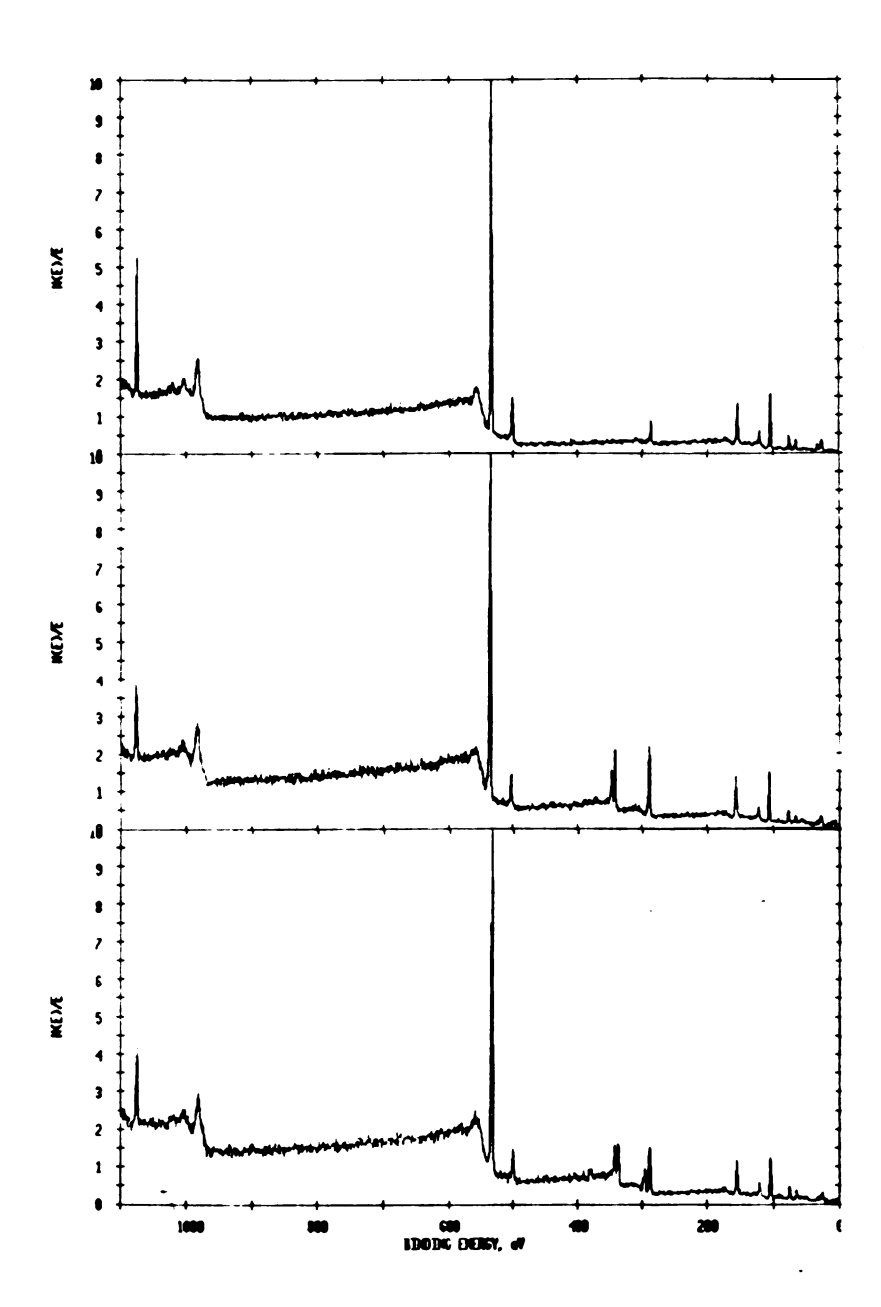


Figure 5-4. XPS survey scans of (A) plain zeolite Y (B) after Na<sub>2</sub>PdCl<sub>4</sub> ion exchange ( new peaks of Pd 3d<sub>5</sub>/<sub>2</sub> at 337 eV and 3d<sub>3</sub>/<sub>2</sub> at 343 eV appear and Na 1s peak at 1071 eV decreases) (C) after reduction by . K<sup>+</sup>(15C<sub>5</sub>)<sub>2</sub>e<sup>-</sup>.(new peaks of K 2p appear showing potassium cations balance the counter charge)

Copper cations in Zeolite Y were reduced by electrides as shown in Figure 5-5. The binding energy of the copper  $2p_{3/2}$  level shifts from 934.35 to 933.70 eV after reduction. The peak was shifted 2.1 eV to higher binding energy after exposure to air for 24 hours. We assume that this is the oxidation of copper to cupric oxide in zeolite because the peak maximum is rather poorly defined with respect to the Cu peak due to significant broadening, probably associated with multiple splitting. Moreover, the strong shakeup peak located 10 eV above the principle copper  $2p_3/2$  line is a good indication of the presence of CuO.(62) The copper L3M45M45 Auger spectra of Cu<sup>2+</sup>. Cu<sup>0</sup> and CuO in zeolite are all shifted to different kinetic energies. However, these peaks are broad and somewhat more difficult to characterize because of the large number of discrete Auger lines under this envelope. There is no surface enrichment of copper either after reduction or re-oxidation. Transmission electron microscopy and powder X-ray diffraction were also obtained. Clean surfaces and no structural change of the zeolite were observed.

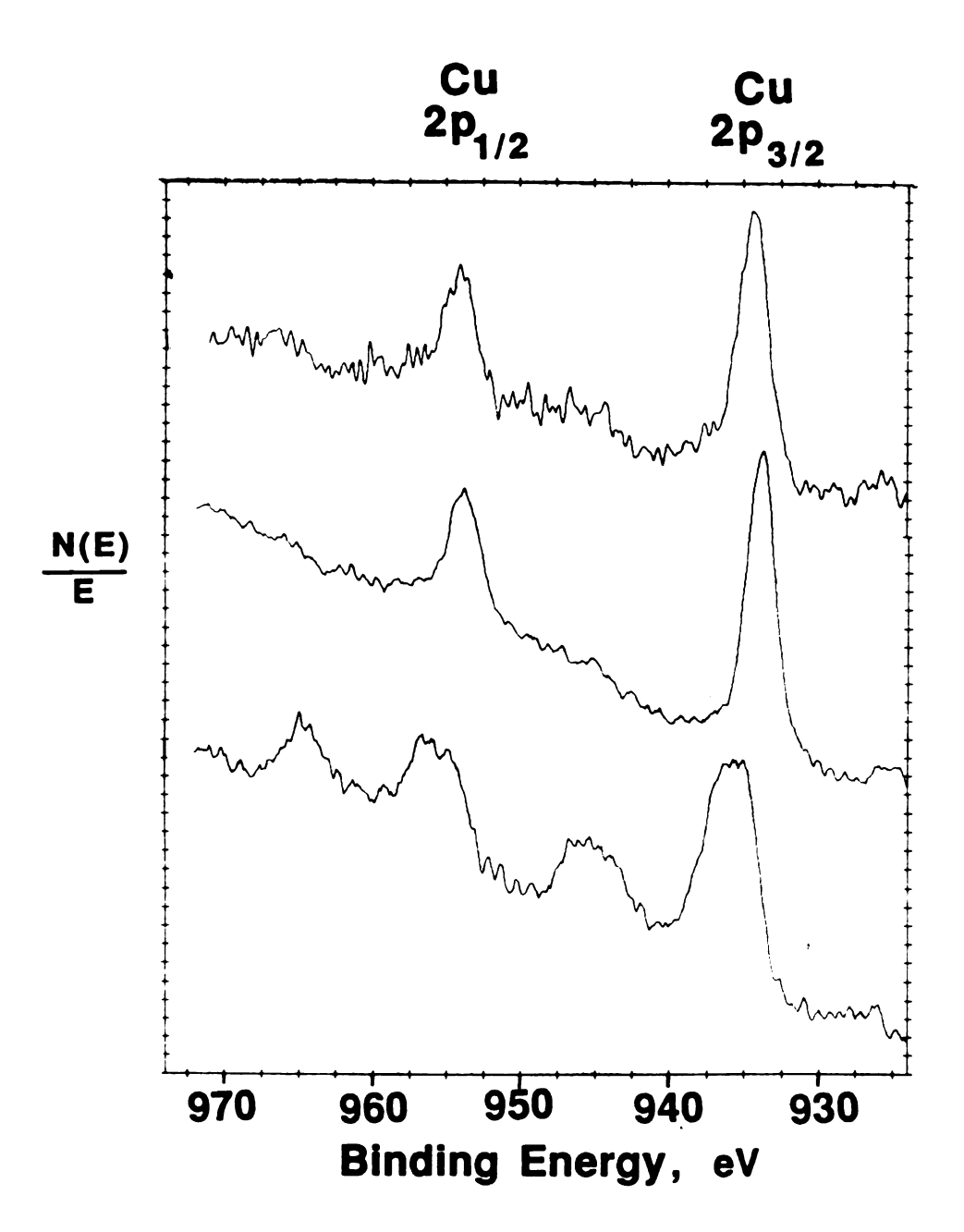


Figure 5-5. XPS spectra of Cu in zeolite Y before reduction  $(2p_3/2=934.35 \text{ eV}. 2p_1/2=954.15 \text{ eV top})$ , after reduction  $(2p_3/2=933.7 \text{ eV}. 2p_1/2=953.8 \text{ eV middle})$ , and oxidized in the air  $(2p_3/2=935.8 \text{ eV}, 2p_1/2=955.9 \text{ eV bottom})$ .

Silver cations were reduced by electrides in Me<sub>2</sub>O. The silver 3d5/2 peak shifted from 369.5 to 368.75 eV after reduction with great surface enrichment. Figure 5-6 shows XPS spectra of Ag in zeolite Y before reduction 3d5/2=369.5 eV. 3d3/2=375.6 eV (top) and after reduction 3d5/2=368.7 eV, 3d3/2=374.7 eV (bottom). Figure 5-7 shows the survey scans of (A) plain zeolite Y (B) after AgCI ion exchange (new peaks of Ag 3d5/2 at 369 eV and 3d3/2 at 375 eV appear and Na 1s peak at 1071 eV disappear) (C) after reduction by  $K^+(15C5)_2e^-$  (new peaks of K 2p appear showing potassium cations balance the counter charge). The average particle size estimated by Scherrer's equation from the powder X-ray peak broadening is about 40 Å. A TEM micrograph of reduced silver zeolite also confirmed that silver particles were on the external surface of the zeolite crystals. The reduced silver clusters may migrate out of zeolite cavities after reduction and aggregate to larger and stable particle size. Alternatively, the silver cations may exchange with potassium cations first and then react with electride on the surface of the zeolite.

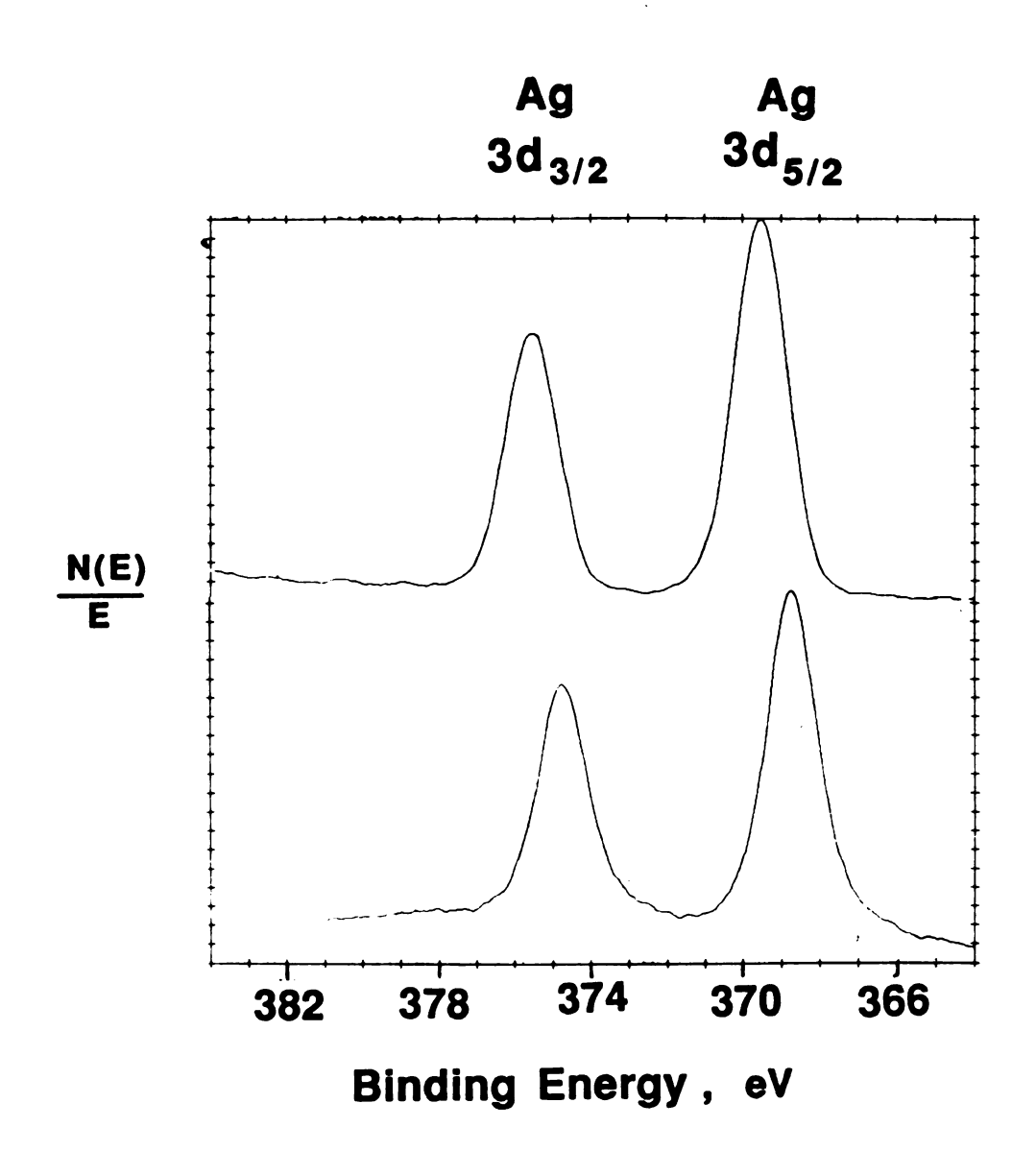


Figure 5-6. XPS spectra of Ag in zeolite Y before reduction 3d5/2=369.5 eV. 3d3/2=375.6 eV (top) and after reduction 3d5/2=368.7 eV. 3d3/2=374.7 eV (bottom).

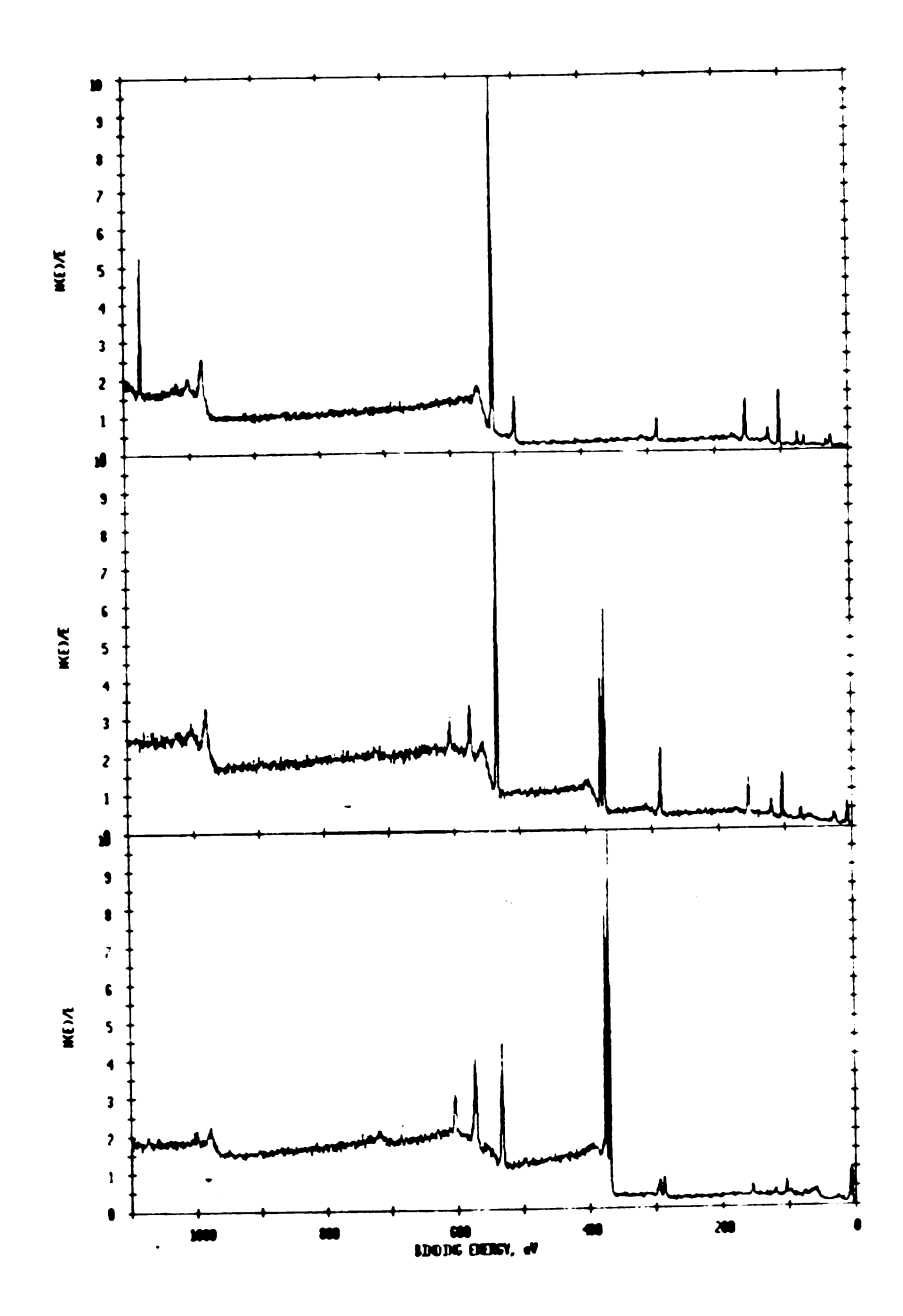


Figure 5-7 XPS survey scans of (A) plain zeolite Y (B) after AgNO3 ion exchange (new peaks of Ag 3d5/2 at 369 eV and 3d3/2 at 375 eV appear and Na 1s peak at 1071 eV disappear) (C) after reduction by . K+(15C5)2e-.(the peak intensities of Ag show surface enrichment and new peaks of K 2p appear showing potassium cations balance the counter charge).

## D. Summary

Electrides, the most powerful reducing agents, can reduce  $Cu^{2+}$ ,  $Pd^{2+}$ , and  $Ag^+$  originally present in Y zeolite pores. XPS data show that these cations were completely reduced to the zero oxidation state by  $K^+(15C5)_2e^-$  at -50 °C. XPS is clearly a valuable tool for studying small metal particles or catalysts. In addition to its surface sensitivity. XPS is uniquely capable of providing chemical information such as oxidation state and chemical bonding, as well as elemental compositions.

XPS shows that the electride is powerful enough to reduce Pd. Cu and Ag cations to the metallic state. XRD data indicates that there is no structural change of the zeolite during the ion-exchange and reduction precesses. A TEM investigation showed no particle aggregation on the zeolite surface in the cases of Pd & Cu. for which it is believed that Pd and Cu were reduced to the metallic state and remained trapped inside the zeolite pores, while K<sup>+</sup> balances the counter charge upon reduction. However, Ag formed particles that were 40 Å in diameter, uniformly dispersed on the external surface.

## Chapter 6 CONCLUSIONS and SUGGESTIONS for FUTURE WORK

The science and technology of nanometer particles have been greatly advanced to meet the urgent demands of modern industries including catalysts, sensors, electromagnetic devices, and photosensitive materials. Monodispersed colloidal systems are invaluable for this purpose because the entire system's uniform physical/chemical properties directly reflect the properties of each individual particle. The highly dispersed solid state is thermodynamically unstable, thus highly dispersed metals are not found in nature. However, metals with high melting temperature can be obtained and maintained in this state over long periods of time, since aggregation involves a high activation energy.

The objective of this study was to test the generality of homogeneous reductions of soluble metal salts by solvated electrons and/or alkali-metal anions in aprotic solvents. Although many of the metals studied can be prepared as small particles by other methods, this method has the advantage of being rapid and quantitative and of requiring only low temperatures for all steps. The initial reduction products must consist of very small, reactive particles as binary alloy formation is observed rather than mixtures of metals when two metal salts are simultaneously reduced. This new method for the preparation of metal/oxidized metal or alloy particles not only

provides the nanoscale particles of metals and alloys but also produces relatively uniform particle size.

For a single element reduction, soluble compounds of transition metals and post-transition metals in dimethyl ether or tetrahydrofuran are rapidly reduced at -30 °C by dissolved alkalides or electrides to produce metal particles with crystallite sizes from < 3 to 15 nm. The products were characterized by X-ray photoelectron spectroscopy, powder X-ray diffraction and selected area electron diffraction. The average particle size was estimated from the line broadening of powder X-ray diffraction. Particle size distributions were determined by counting the particles on electron micrographs obtained by transmission electron microscopy. Salts of Au. Pt. Cu. Te. Fe. and Ta formed metallic particles with little or no oxidation even when washed with methanol or liquid ammonia. Reduction of salts of Ni. Fe. Zn. Ga. Si. Mo. W. In. Sn. and Sb yields surface oxidation over a metallic core. This method is also applicable to the formation of finely divided metals on oxide supports.

X-ray amorphous alloys or intermetallic compounds formed when two different metal salts were used, as indicated by X-ray photoelectron spectroscopy. Selected area electron diffraction revealed the structure of air-stable samples. Reduction of salts of Au-Cu, Au-Zn, Cu-Te, Zn-Te, Au-Ti, Fe-Ta formed particles that contained intermetallic compounds.

The reduction of  $Cu^{2+}$ ,  $Pd^{2+}$ . Ag<sup>+</sup> in zeolite-Y was made. X-ray photoelectron spectroscopy data show that these cations were completely reduced to zero oxidation state at -30 °C. Cu and Pd remain trapped in the interior and an alkali metal cation balances

the counter charge upon reduction. In contrast, Ag formed 40 Å diameter particles uniformly on the external surface.

The nanoscale metal particles are extremely air-sensitive: they will be oxidized in a few seconds without any protection in the air.

X-ray photoelectron spectroscopy has proven to be a useful tool in the study of nanoscale particles. In addition to its surface sensitivity.

XPS is capable of providing chemical information such as the oxidation state and the nature of the chemical bonding, as well as elemental composition.

Powder X-ray diffraction and selected area electron diffraction provide additional characterization of those air-stable particles. Average particle size was estimated from the line broadening of powder X-ray diffraction. Particle size distributions and morphology was made from the electron micrographs of transmission electron microscopy.

The small angle X-ray scattering has undergone considerable progress in recent years. Experiments on the characterization of supported metallic catalysts have demonstrated that even for low metal concentration (0.6% Pt on alumina), distribution curves of the particle diameters can be obtained which are comparable to electron microscopy results. (63) Moreover, one of the main advantages of this technique is the possibility to obtain directly a parameter proportional to the metallic surface area.

This technique is especially favorable for the preparation of metal particles in zeolites. As the pores are regularly arranged in the zeolite, the scattering produced by the support is very weak. Therefore about 95% of the small angle X-ray diffraction intensity is

related to metal. Clearly this technique can give one a true particle size distribution over the pure metallic particles or metal particles on support. I think the small angle X-ray scattering should be the next step to use.

Extended X-ray absorption fine structure (EXAFS) is another method that can give insight into the structure and dimensions of the small metallic particles. This method is based on absorption of X-rays resulting from the excitation of an electron from core states and the subsequent scattering of the outgoing photoelectron waves by neighbors of the excited atom. Experimentally, the method requires intense X-rays sources and thus became practicable only recently due to the availability of intense synchrotron X-ray sources.

As a structural technique, the EXAFS method has many advantages. Since the X-ray absorption is specific for a given element, it is possible to analyze separately the environment of each kind of atom in a multi-component system. Due to its sensitivity to the immediate neighborhood of the X-ray absorbing atom, a single crystal is not required and the method can be successfully used both with small size crystallites and even amorphous solids. In the case of extremely small microcrystals and clusters, the mean coordination number around a given atomic species is smaller than that observed in massive solids.

Due to these advantages, a significant amount of work has already been performed on highly dispersed metals with investigations of the local chemical composition, structure and determinations of the size distributions of the smallest clusters. In particular, supported platinum and copper catalysts have been

investigated with this technique. (64. 65) EXAFS should be another technique for the characterization of small particles and supported particles.

Colloidal particles are normally formed through a sequential process of nucleation and growth of the nuclei. To obtain a monodispersed system, the two stage must be strictly separated and nucleation avoided during the growth period. Since the steady concentration of monomers in the growth stage is determined by the balance between the rates of generation of monomers and their consumption by particle growth, the generation or introduction rate of monomers must be controlled so that it is low enough to keep the balanced monomer concentration below critical supersaturation after the nucleation period.(66)

Typically, the initial concentration of metal salts, alkalide/electride, and temperature must be adjusted to meet this requirement for the formation of monodispersed particles. I have demonstrated that the particle sizes can be decreased by lowing the initial concentration of the metal salts. In order to produce monodispersed small metallic or alloy particles. I think much more work can be done by controlling the temperature and the concentration of alkalide/electride.

The reduction with alkalides/electrides is so powerful that alloys can be formed instead of separated metals when mixed metal salts are reduced. A lot of alloys which are very useful in industrial applications might be made by this method including: semiconductors (GaAs), shape memory alloys (NiAl), magnetic particles (Fe2O3, NiFe2O3, and CoFe2O4). It is hope that this

introduction of a new low temperature method for the preparation of nanoscale metal and alloy particles will lead to further developments by others.

## **APPENDIX**

	compound	trials	comments
1	AuC13	9	The solubility of AuCl <sub>3</sub> is high both in Me <sub>2</sub> O and THF. Colloidal Au solution was formed first. The Au particles start to aggregate a few seconds later in Me <sub>2</sub> O. The colloidal Au is stable in THF at least 3 hours. The black Au particles can be washed by MeOH or H2O in the air easily.
2	CuCl <sub>2</sub>	15	The red colloidal Cu is stable in THF for at least 48 hours in room temperature. The black Cu products can be washed by MeOH under protection. The unwashed products turned green several days later in the air.
3	TeBr4	4	The solubility of TeBr4 is high both in Me <sub>2</sub> O and THF. The black metallic Te can be collected by washing the reaction products with MeOH under protection.
4	ZnI <sub>2</sub>	24	The Zn product will be oxidized easily without careful protection. Only broadened ZnO XRD lines were observed from MeOH washed products.
5	NiCl <sub>2</sub>	5	Triethyl phosphine was added to increase the solubility of NiCl <sub>2</sub> in Me <sub>2</sub> O and THF. The Ni products can be oxidized easily without good protection. Ni(Et <sub>3</sub> P) <sub>2</sub> Cl <sub>2</sub> can be reduced directly by alkalide or electride in Me <sub>2</sub> O or THF.
6	FeC13	3	A deep green colloid was formed when washed with MeOH. The clean metallic Fe can be collected by washing with NH <sub>3</sub> in the H-cell.

7	C-C1	1	Doub modellie Co and seel do seeles
′	GaC13	6	Both metallic Ga and oxide peaks were observed for unwashed and MeOH
			washed products from XPS.
8	SiCl4	4	Both elemental Si and oxide peaks
		}	were observed for unwashed and
	ł		MeOH washed products from XPS.
			Only oxide peaks were observed if the
			products were not carefully protected.
9	GeC14	1	Both metallic Ge and oxide peaks were
		}	observed for unwashed and MeOH
			washed products from XPS.
10	SbC15	4	Both metallic Sb and oxide peaks were
			observed for unwashed and MeOH
			washed products from XPS.
11	SnC14	2	Both metallic Sn and oxide peaks were
	ĺ		observed for unwashed and MeOH
			washed products from XPS.
12	InCl <sub>3</sub>	3	Both metallic In and oxide peaks were
		İ	observed for unwashed and MeOH
		1	washed products from XPS.
13	MoC15	1	Both metallic Mo and oxide peaks were
		i -	observed for MeOH washed products
		ļ	from XPS. Only Mo oxide was
			observed upon washing by MeOH.
14	WC16	5	Both metallic W and oxide peaks were
	" 5.0		observed for MeOH washed products
		į	from XPS. Only W oxide was observed
	i		upon washing by MeOH.
15	H <sub>2</sub> PtCl <sub>6</sub>	2	Black metallic Pt can be washed by
• •	112. 10.6	-	MeOH or H <sub>2</sub> O. The particle size is
			about 3-4 nm from TEM microgragh.
16	TaC15	4	Ta metallic particles can be washed
•	1	1	cleanly by liquid NH <sub>3</sub> . Only Ta oxide
			was observed upon washing by MeOH
17	Mola	5	Products were unable to be identified
' /	MnI <sub>2</sub>	,	at this time.
18	AICIa	5	
10	AIC13	ر ا	The unwashed reduction products
			were not identified by XPS because the
			peak separation between metallic Al
			and oxide is too narrow. Gas evolution
			was observed upon washing with
L	I	<u> </u>	MeOH.

19	VC13	4	VCl <sub>3</sub> was reduced by alkalide or electride. The products have not yet
			been characterized yet.
20	Cdl <sub>2</sub>	2	Metallic Cd was observed in the unwashed reaction products. The
		j	oxidized product was identified as
			Cd(OH) <sub>2</sub> by XPS upon washing with
	l		MeOH.
21	YC13	2	Only Yittrium oxide was observed in
			the unwashed products.
22	TiCl4	11	Only Titanium oxide was observed in
		!	the unwashed products and MeOH
			washed products.
23	AuCl <sub>3</sub>	5	The products were identified as AuZn
	ZnI <sub>2</sub>		(CsCl type structure) by XPS and SAD.
24	AuCl <sub>3</sub>	4	The products were identified as Cu Au
	CuCl <sub>2</sub>		(CsCl type structure) by SAD.
25	AuC13	3	Two new peaks of Au $4f_{5/2}$ and $4f_{7/2}$
	Til4		from XPS shows that there is a new
			compound formed. The compound has
			not yet been identified.
26	AuCl <sub>3</sub>	3	Reduction of this mixture gave X-ray
	TeBr4		amorphous products except when an
			excess of one component was used.
			XPS data suggested that a new
			compound was formed.
27	CuCl <sub>2</sub>	3	Reduction of this mixture gave X-ray
	TeBr4		amorphous products except when an
			excess of one component was used.
			XPS data suggested that a new
<u></u>			compound was formed.
28	CuCl <sub>2</sub>	2	Reduction of this mixture gave X-ray
	Znl <sub>2</sub>		amorphous products except when an
			excess of one component was used.
1			XPS data suggested that a new
			compound was formed.

	T-01	T.	The second second second
29	TaC15	1	The product has not yet been
	FeC13		identified, but the XPS data show the
			presence of Ta. Fe and K in
		1	approximately a 1:2:3 mole ratio when
			a 1:2 ratio of TaCl5 and FeCl3 was
			reduced by excess K+(15C5) <sub>2</sub> K- in
			Me <sub>2</sub> O.
30	SbC15	1	Unable to identify the products at
	GaC13		present time.
31	AIC13	1	Unable to identify the products at
	TeBr <sub>4</sub>	!	present time.
32	Cdl <sub>2</sub>	1	Unable to identify the products at
	TeBr4		present time.
33	CuCl <sub>2</sub>	1	Unable to identify the products at
	MnCl <sub>2</sub>	1	present time.
34	InCl <sub>3</sub>	1	Unable to identify the products at
٦٦	TeBr4	*	present time.
35	AuCl <sub>3</sub>	1	Unable to identify the products at
ردا	GaCl <sub>3</sub>	1	present time.
36	Cu <sup>2+</sup>	3	
٥٥	on Na-Y	٦	Cu <sup>2+</sup> loading percentage can be
	on Na-1		increased by multiple step ion-
			exchange. Metallic Cu peaks were
l			observed. These Cu particles may stay
}			inside the sodalite cage or the super
			cage of the zeolite-Y. The metallic Cu
			clusters were oxidized easily upon
	5.42		exposure to air.
37	Pd <sup>2+</sup>	2	Pd <sup>2+</sup> loading percentage can be
	on Na-Y		increased by multiple step ion-
			exchange. Metallic Pd peaks were
			observed. These Pd particles may stay
l			inside the sodalite cage or the super
			cage of the zeolite-Y.
38	Ag+	3	Almost 100% Na+ was replaced by Ag+
	on Na-Y		after ion exchange. Metallic Ag
	ł		particles were observed on the surface
			of zeolite-Y.
39	AuCl <sub>3</sub>	3	Au <sup>3+</sup> did not ion-exchange with Na <sup>+</sup> in
	on Na-Y		zeolite-Y. Au particles on the surface
			of zeolite-Y were observed after
			reduction with alkalide or electride.
L	<del></del>	<del></del>	

40	AuCl <sub>3</sub> on Al <sub>2</sub> O <sub>3</sub>	2	Au particles with 4 nm diameter were observed on the surface of Al <sub>2</sub> O <sub>3</sub> from TEM microgragh.
41	H <sub>2</sub> PtCl <sub>6</sub> on Al <sub>2</sub> O <sub>3</sub>	2	No individual Pt particles were observed on the surface of Al <sub>2</sub> O <sub>3</sub> from TEM microgragh, but Pt signal was observed by EDS and a metallic Pt pattern was observed by SAD.

## References

- (1) C. W. Weyl. Annalen der Physik and Chemie, 197, 601 (1864).
- (2) C. J. Pedersen J. Am. Chem. Soc., 89, 7017 (1967).
- (3) B. Dietrich, J. M. Lehn and J. P. Sauvage, *Tet. Letters*, **34**, 2855 (1969).
- (4) B, Dietrich, J. M. Lehn and J. P. Sauvage, *Tet. Letters*, **34**, 2889 (1969).
- (5) J. L. Dye, J. M. Ceraso, M. T. Lok, B. L. Barnett, and F. J. Tehan, J. Am. Chem. Soc., 96, 608 (1974).
- (6) A. S. Ellaboudy, P. B. Smith and J. L. Dye, J. Am. Chem. Soc., 105.6490 (1983).
- (7) J. L. Dye, Angew. Chem. Int. Ed. Eng., 18, 587 (1979).
- (8) J. L. Dye, C. W. Andrews and J. M. Ceraso, *J. Phys. Chem.*, 79, 3076 (1975).
- (9) R. S. Bannwart, S. A. Solin, M. G. DeBacker, and J. L. Dye, J. Am. Chem. Soc., 111, 5552 (1989).
- (10) D. Issa, A. E. Ellaboudy, R. Janakiraman, and J. L. Dye, *J. Phys. Chem.*, 88.3847 (1984).
- (11) S. B. Dawes, D. L. Ward, R. H. Huang, and J. L. Dye, J. Am. Chem. Soc., 108, 3534 (1986).
- (12) S. Doeuff, K. L. Tsai, and J. L. Dye, Inorg. Chem., 30, 849 (1991).
- (13) J. S. Landers, A. Stacy, M. J. Sienko, and J. L. Dye, J. Phys. Chem..85, 1096 (1981).

- (14) J. Papaioannou. S. Jaenicke, and J. L. Dye, J. Solid State Chem.67, 122 (1987).
- (15) K. J. Moeggenborg, J. Papaioannou, and J. L. Dye, *Chem. Mater.*. 3, 514 (1991).
- (16) J. L. Dye, Scientific American, 257, 66 (September, 1987).
- (17) J. L. Dye. J. Phys. Chem., 84, 1084 (1980).
- (18) F. Fievet, J. P. Lagier and M. Figlarz, MRS Bull., December, 29 (1989).
- (19) J. Livage, M. Henry, J. P. Jolivet and C. Sanchez, MRS Bull., January, 18 (1990).
- (20) J. J. K. Schloten, J. A. Konvalinka and F. W. Beekman, J. Catal.28, 209 (1973).
- (21) R. M. Wilenzick, D. C. Russel, R. H. Morris and S. W. Marschall, J. Chem. Phys., 47, 533 (1967).
- (22) D. W. MacKee and F. J. Norton, J. Phys. Chem., 68, 481 (1964).
- (23) R. D. Rieke, Science, 246, 1260 (1989).
- (24) L. Chao and R. D. Rieke, J. Organometal. Chem., 67, C64 (1974).
- (25) R. D. Rieke and S. E. Bales. J. Am. Chem. Soc., 96, 1775 (1974).
- (26) R. D. Rieke and P. M. Hudnall, *J. Am. Chem. Soc.*, **94**, 7178 (1972).
- (27) M. J. McCormick, K. B. Moon, S. R. Jones and T. P. Hanusa, J. Chem. Soc. Chem. Commun., 778 (1990).
- (28) P. G. Fox. J. Ehretsman and C. E. Brown. J. Catal., 20, 67 (1971).
- (29) W. B. Philips, E. A. Desloge and J. G. Skofronick, Appl. Phys., 39.3210 (1967).
- (30) K. J. Klabunde, H. F. Hfner, T. O. Murdock and R. Rople, *J. Am. Chem. Soc.*, **98**, 1021 (1976).

- (31) J. H. Jean and T. A. Ring, Langmuir, 2, 251 (1986).
- (32) H. Bonnemann. W. Brijoux and T. Joussen. *Angew. Chem. Int. Ed. Engl.*. 29, 273 (1990).
- (33) See, for example, (A) C. D. Wagner, L. H. Gale and R. H. Raymond, Anal. Chem., 5, 466 (1976). (B) D. Briggs and M. P. Seah. "Practical Surface Analysis by Auger and X-ray Photoelectron Spectroscopy", John Wiley & Sons, Inc., New York(1983).
- (34) See, for example, (A) A. Schuster and J. W. Nicholson, "An Introduction to the Theory of Optics", Edward Arnold and Co., London, third edition, (1924), page 11. (B) H. P. Klug and L. E. Alexander, "X-ray Diffraction Procedures for Polycrstalline and Amorphous Materials", John Wiley & Sons, Inc., New York, 491-583 (1962).
- (35) P. P. Edwards, Adv. Inorg. Chem. Radiochem., 25,135, (1982).
- (36) J. C. Thompson. Electrons in liquid ammonia. (Oxford University Press. 1976)
- (37) J. J. Lagoski and M. J. Sienko, Eds. "Metal ammonia Solutions". (IUPAC, Butterworths, London, 1970).
- (38) J. L. Dye. Conference Organizer. Colloque Weyl IV. "Electrons in Fluids- The Nature of Metal Ammonia Solutions". J. Phys. Chem.,
   79. No 26 (1975).
- (39) C. A. Kraus and H. F. Kurtz. J. Am. Chem. Soc., 47, 43 (1925).
- (40) J. L. Dye, M.G. DeBacker and V. A. Nicely, *J. Am. Chem. Soc.*, **92**, 5226 (1970).

- (41) J. L. Dye, M.T. Lok, F.J. Tehan, R.B. Coolen, N. Papadakis, J. M. Ceraso and M. G. DeBacker, *Ber. Buncenges Phys. Chem.*, 75, 3092 (1971).
- (42) J. L. Dye "Electrons in Fluids"; (J. Jortner, N. R. Kestner, Eds Springer-Verlag, Berlin, 1973).
- (43) J. L. Dye. Science. 247, 663 (1990).
- (44) M. T. Lok. F. J. Tehan, and J. L. Dye. *J. Phys. Chem.*, **76**, 2975 (1972).
- (45) K. Tsai and J. L. Dye. J. Am. Chem. Soc., 113, 1650 (1991).
- (46) C. D. Wagner, W. M. Riggs, L. E. Davis, J. F. Moulder, and G. E. Muilenberg, "Handbook of X-ray Photoelectron Spectroscopy": Perkin-Elmer: (1979); p154.
- (47) R. D. Rieke, Science (Washington, D.C.) 246, 1260 (1989) and references therein.
- (48) H. Abe, K. P. Charle, B. Tesche, and W. Schulze, *Chem. Phys.*, 68, 137 (1982).
- (49) R. H. Doremus, J. Chem. Phys., 40, 2389 (1964).
- (50) C. D. Wagner, W. M. Riggs, L. E. Davis, J. F. Moulder, and G. E. Muilenberg, "Hand book of X-ray photoelectron spectroscopy".
  Perkin-Elmer.(1979), p. 154
- (51) J. C. Fuggle, E. Kaline, L. M. Watson, and D. J. Fabian, *Phys. Rev.*.B16, 750 (1977).
- (52) C. H. Johansson and J. O. Linde, Ann. Physik, 25, 1-48 (1936).
- (53) S. Bhatia "Zeolite Catalysis: Principles and Applications". CRC Press, Inc. (1990)
- (54) D.W. Breck, W. G. Eversole, R. M. Milton, T. B. Reed, and T. L. Thomas, J. Am. Chem. Soc., 78, 5963 (1956).

- (55) a. I. E.Maxwell. Adv. Catal., 31, 1 (1982).
  b. P. Gallezot. Catal. Rev. Sci. Eng., 17, 273 (1978).
- (56) D. W. Breck. "Zeolite Molecular Sieves"; Wiley: New York. (1974).
- (57) G. Kumar, J. R. Blackburn, W. E. Moddeman, R. G. Albridge, and M. M. Jones, *Inorg. Chem.*, 11, 296 (1972).
- (58) V. N. Romannikov and K. G. Ione. J. Catal., 66.121 (1980).
- (59) J. C. Vedrine, M. Dufaux, C. Naccache, and B. J. Imelik, *Chem. Soc. Faraday Trans.*, 174, 440 (1978).
- (60) J. H. Scofield, J. Electron Spectrosc., 8, 129 (1976).
- (61) L. Broussard and D. P. Shoemaker, J. Am. Chem. Soc., 82, 1041 (1960).
- (62) N. S. McIntyre and M. G. Cook. Anal. Chem., 47, 2208 (1975).
- (63) A. Renouprez, C. Hoang-Van and P. A. Companon. J. Catal.. 34.411 (1974).
- (64) G. H. Via, J. H. Sinfelt and F. W. Lyttle, *J. Cem. Phys.*, 71, 690 (1979).
- (65) S. J. Gurman, J. Mat. Sci., 17, 1541 (1982).
- (66) T.Sugimoto., Adv. Colloid Interface Sci., 28, 65 (1987).

